# Aerodynamics of finite-span inclined flat plates in ground proximity

by

Supun Pieris

A thesis
presented to the University of Waterloo
in fulfilment of the
thesis requirement for the degree of
Doctor of Philosophy
in
Mechanical and Mechatronics Engineering

Waterloo, Ontario, Canada, 2023

**Examining Committee Membership**

The following served on the Examining Committee for this thesis. The decision of the Examining Committee is by majority vote.

| | |
|---|---|
| External Examiner | Prof. dr. K. Mohseni<br>Professor<br>Dept. of Mechanical and Aerospace Engineering<br>University of Florida |
| Supervisor | Prof. dr. S. Yarusevych<br>Professor<br>Dept. of Mechanical and Mechatronics Engineering<br>University of Waterloo |
| Supervisor | Prof. dr. S.D. Peterson<br>Professor<br>Dept. of Mechanical and Mechatronics Engineering<br>University of Waterloo |
| Internal Members | Prof. dr. M. Collins<br>Professor<br>Dept. of Mechanical and Mechatronics Engineering<br>University of Waterloo |
| | Dr. Z. Pan<br>Assistant Professor<br>Dept. of Mechanical and Mechatronics Engineering<br>University of Waterloo |
| Internal-External Member | Dr. B. MacVicar<br>Associate Professor<br>Dept. of Civil and Environmental Engineering<br>University of Waterloo |

## Author's Declaration

This thesis consists of material all of which I authored or co-authored: see Statement of Contributions included in the thesis. This is a true copy of the thesis, including any required final revisions, as accepted by my examiners.

I understand that this document may be made electronically available to the public.

## Statement of Contributions

All research was conducted at the University of Waterloo. I, Supun Pieris, was the sole author for Chapters 1–3 and 7, which were written under the supervision of Dr. Serhiy Yarusevych and Dr. Sean Peterson and were not written for publication. Chapters 4–6 are adapted from two published manuscripts and a conference paper, where myself and my supervisors were involved:

- Chapter 4: Pieris, S., Yarusevych, S., & Peterson, S. D. 2022. Flow development over inclined flat plates in ground effect and relation to aerodynamic loads. *Phys. Fluids*, **34**(9), 095113.
- Chapter 5: Pieris, S., Yarusevych, S., & Peterson, S. D. 2023. Effect of yaw angle on aerodynamics of square inclined flat plates in ground effect. *Phys. Fluids*, **35**(5).
- Chapter 6: Pieris, S., Yarusevych, S. V. & Peterson, S. D. 2023. Effect of dynamic wind direction changes on aerodynamics of a square inclined flat plate in ground effect. *AIAA Aviat. 2023 Forum.*, San Diego, CA, June 12-16.

The breakdown of contributions for the works listed above are as follows:

| | Mr. Pieris | Dr. Yarusevych | Dr. Peterson |
|---|---|---|---|
| Conceptualization | equal | equal | equal |
| Methodology | equal | equal | equal |
| Investigation | lead | supporting | supporting |
| Data curation | lead | - | - |
| Visualization | lead | - | - |
| Analysis and interpretation | equal | equal | equal |
| Writing - original draft | lead | - | - |
| Writing - review and editing | supporting | equal | equal |

Funding was provided by the Natural Sciences and Engineering Research Council of Canada and the Ontario Graduate Scholarship Program.

## Abstract

Photovoltaic power generation has grown to become a multi-billion dollar global sector, aiding in the switch to renewable energy sources to limit the progress of climate change. However, relatively high energy production costs at the utility scale currently limits capacity expansion. A comprehensive understanding of salient flow physics and the relation to associated aerodynamic loading are critical in reducing costs through appropriate sizing of support structures, improving site selection criteria, and providing guidance for future load reducing flow control strategies. The research presented in this thesis is centred around this effort, as flow development and aerodynamic loading on finite-span inclined flat plates in close ground proximity subject to both steady and unsteady flow conditions are experimentally investigated. The supporting data consists of direct force measurements, surface flow visualization, and particle image velocimetry.

In the first part of the thesis, the influence of aspect ratio, pitch angle, and ground proximity under steady headwind and tailwind conditions on the aerodynamic forcing and flow over inclined flat plates was investigated. Ground proximity-related effects are most notable when the plate was closer than 0.75 chord lengths from the ground, near the stall angle, where pronounced changes in the midspan and wake flow development take place. The modulation of free flight aerodynamics by ground proximity is dependent on the specific combination of aspect ratio, angle of attack, and wind direction. Notably, for headwinds, the increase in static pressure on the underside leads to increased aerodynamic loads, while for tailwinds, either a decrease or insensitivity in aerodynamic loads is observed with closer ground proximity depending on the aspect ratio.

In the second part of the thesis, the yaw angle of a square plate at an angle of attack of 30° was varied between 0° and 180° to simulate steady wind directions. Ground effect-related aerodynamic changes are strongly dependent on yaw angle. Between yaw angles of 0° and 90°, a ground height invariant suction side flow is observed; however, the aerodynamic loading increases due to a higher static pressure on the ground facing area relative to free flight conditions. For yaw angles between 90° and 120°, the suction side and thus the loading is ground height invariant. Between yaw angles of 120° and 150°, notable sting effects confound any ground proximity related effects. Further increase in yaw angle, up to 180°, leads to an onset of stall with decreasing ground proximity reducing the aerodynamic loading.

For the third part of the thesis, the aerodynamics of a square inclined plate under moderate ground effect is investigated for yaw angles between 0° and 30°. Transient changes in wind direction was modelled by a yaw rotation from 0° and 30° as well as from 30° and 0°, over 3.8 convective time units. Peak transient lift coefficients are above 10% of steady state levels immediately following the yaw rotation. Both the tip vortex circulations and the lift coefficient exhibit a consistent hysteresis, highlighting the important role tip vortices play in lift generation under dynamic conditions.

**Acknowledgements**

I am deeply indebted to my supervisors, Serhiy and Sean, for providing me this opportunity to pursue a PhD with the two of them. Thank you for the guidance, expertise, and insights that have been invaluable through this endeavour. Your high standards and relentless approach for conducting research is an example to everyone. I have learned a lot from the both of you, about research and life.

Thank you to the examination committee members, Prof. Mohseni, Prof. Collins, Dr. Pan, and Dr. MacVicar for taking the time to read this thesis, in order to pose valuable questions and improvements.

Thank you to all the technical staff in the Mechanical and Mechatronics Engineering department for the help in putting together the experimental setup. Special mention to Jason Benninger for fabricating most of the solar panel setup and Neil Griffett for helping with troubleshooting numerous equipment quirks.

I would like to thank all of my colleagues, part and present, at the FMRL and FFPL groups. In some form or another, all of you have supported me, which is greatly appreciated. Special mention to John for the banter-filled, yet consutructive discussions about wind tunnel experiments and tinkering with PCs; I would know far less about getting perfect PIV results and data storage servers otherwise. Nikhilesh, thank you for our humorous and productive talks during routine coffee runs to the Grad house and particularly for your help during the pandemic lab shutdowns. We definitely proved that all you need is a dremel, a drill press, and a dream to do high quality experiments in the fluids lab.

To Steve, I greatly enjoyed our time at FPP and Sunday car washes, where we theory crafted infinitely better endings to Game of Thrones. It was a great way to destress from the PhD grind, thank you. To my mother, Rita, I am eternally grateful for the unimaginable sacrifices you made to give me a better life. To my love, Sarah, thank you for your unconditional love and support through the best of times and the worst of times. Without you, I would not be where I am today. Laslty, to Bean, the best cat ever, thank you for your comforting purrs during thesis writing.

# Table of Contents

*If I have seen further it is by standing on the shoulders of Giants.*

Sir Isaac Newton

# Chapter 1

# Introduction

*Aerodynamics of finite-span inclined flat plates is introduced within the context of stagnating energy production costs currently faced by the solar power industry. Knowledge gaps within the current understanding of finite-span inclined flat plate aerodynamics that may reduce the cost of solar energy generation are highlighted and used to formulate research objectives of this thesis.*

Technological advancements in the last century have led to an ever increasing demand for energy, which has been largely addressed by non-renewable energy sources, mainly fossil fuels [1]. Continued use of fossil fuels is expected to lead to significant and permanent changes to the Earth's ecosystems, the consequences of which will severely impact the quality of life of future generations [2–8]. This has sparked initiatives to incentivise renewable energy sources, which has been facilitated by new national policies on a global scale [9, 10]. In 2022, global investments in renewable energy sectors totalled $ 366 billion (USD), with 56% of these invesments allocated to the solar photovoltaic industry [10]. The global solar industry has observed an exponential growth in terms of power production in the last decade, with a matching decrease in energy production costs, however, in the last three years energy production costs have remained relatively constant [11]. This may be attributed to COVID-19 pandemic related economical effects, however, the stagnating trend was apparent prior to the pandemic [12]. Addressing the stagnating energy production costs is one avenue to further incentavize the switch to solar power.

Photovoltaic installations consist of a solar panel module comprising power generating photovoltaic cells, a support structure, and electrical systems. The structural costs of residential, commercial and utility scale photovoltaic installations has remained relatively high (15-30% of installation costs) [11–13]. As such, there is an oppurtunity to lower costs through improved support structure designs, targeted flow control strategies to minimize aerodynamic loads, and improved site selection criteria guided by aerodnynamic loading consdierations.

Aerodynamics of solar panels is a rich and complex problem despite the relative simplicity of the underlying geometry, i.e, a finite-span inclined flat plate. Early research, such as the canonical work by Fage & Johansen [14], focused on two-dimensional configurations and drew connections between instantaneous loading and wake topology. Solar panels are typically rectangular due to the shape of the solar cells that make up a photovoltaic module and are configured in a large range of aspect ratios ($O(1)$ to $O(10)$ [15–17]). Notably, there are significant differences in the aerodynamic loading within the relevant aspect ratio range due to tip effects [18–22]. At aspect ratios equal to or less than unity, tip vortices produce significant downwash over the plate surface, causing the leading-edge shear layer to reattach near the trailing edge [19, 23]. This flow topology has been shown to produce significantly higher loading and cause an increase in stall angle compared to aspect ratios greater than two for free flight[1] configurations, however, it remains to be investigated in close ground proximity, which is of greater relevance for photovoltaic installations.

Solar panels are typically placed in open terrains to maximize solar irradiance or mounted on roof tops when there is lack of ground space, such as in urban areas. In these environments, photovoltaic installations are subjected to effects of winds and gusts, which can lead to significant steady and impulsive loading on control mechanisms and support structures which may be damaged during extreme weather events [24]. Furthermore, the incoming wind direction can vary significantly throughout the year and also during gusts, which must be accounted for in support structure designs. Although there has been some attention given to effects of wind direction variations on flat plate aerodynamics [25–27], the connection between the flow and loading for the full range of wind directions remains to be investigated for both steady winds and gusts.

[1]free flight is used to describe placement of a submerged body unaffected by nearby surfaces.

Ground proximity of photovoltaic installations is an important consideration when designing support structures as the aerodynamic loading is significantly modified in comparison to free flight conditions, the so-called "ground effect". This is of particular importance since most solar panels are mounted in relatively close ground proximity. Further, in most solar panel installations, the pylon designs are fixed leading to coupled effects of ground proximity and panel orientation. Although some researchers have considered the isolated effects of these parameters on finite-span inclined flat plate aerodynamics [15, 28, 29] for a limited parameter range, recent studies motivated by photovoltaic applications have used fixed supports confounding the effects of ground proximity and panel orientations on aerodynamic loading [26, 30, 31], requiring further investigation. Furthermore, a discrepancy in aerodynamics loading has been observed between headwind and tailwind conditions as the ground clearance is decreased [18, 29], which remains to be clarified through further investigation. Previous studies have also shown ground effect is dependent on aspect ratio, however, the flow development was not considered [18].

## 1.1 Research Objectives and Thesis Outline

Solar energy production costs have been stagnant in recent years [11] creating a barrier to entry. At the same time, there are substantial knowledge gaps in the fundamental understanding of finite-span inclined flat plate aerodynamics, addressing which can lead to cost reduction through improved support structure designs, implementation of targeted flow control strategies, and modification of site selection criteria. To address some of the existing knowledge gaps, a series of experimental investigations are carried out employing direct force and torque measurements, while both qualitative and quantitative non-invasive flow measurements are used to characterize the aerodynamics of a representative solar panel geometry in a wind tunnel. The following objectives are pursued in this thesis:

- Assess the influence of aspect ratio, angle of attack, wind direction, and ground proximity on steady flow development and loading on finite-span inclined flat plates.
- Characterize the transient wake development and loading of a finite-span inclined flat plate in close ground proximity during an extreme weather event and compare to steady state results.
- Relate loading trends to salient flow features for both steady and unsteady incoming flow conditions to provide insights for future photovoltaic installation cost reduction strategies.

The thesis is organized as follows. Chapter 2 provides detailed background information relevant to the investigated flows, including environmental effects and aerodynamics of inclined flat plates. Chapter 3 provides a description of the facility and experimental model, along with an overview of main experimental and data analysis techniques used in this work. In Chapter 4, combined effects of aspect ratio, angle of attack, and ground proximity on aerodynamics of inclined flat plates are investigated. In Chapter 5, the steady effects of wind direction and ground proximity on inclined flat plate aerodynamics near stall are examined. The results from these chapters are used

to determine a critical loading configuration for a sudden wind direction change, and the unsteady aerodynamics of a solar panel model is analyzed in Chapter 6. Lastly, Chapter 7 presents key conclusions stemming from this work and recommendations for future extensions of this research.

# Chapter 2

# Background

*Background information on topics relevant to the study of wind loading on solar panels is outlined in this chapter. An overview of solar panels installations is provided in Section 2.1. The environmental conditions that solar panels experience is presented in Section 2.2, with a specific focus on the in-field characterization and modelling of the atmospheric boundary layer and gusts. Thereafter, previous studies relevant to the free flight aerodynamics of solar panels under steady and transient conditions are reviewed in Section 2.3. Lastly, ground effect aerodynamics is discussed in Section 2.4.*

## 2.1 An Overview of Photovoltaic Installations

In 2021, nearly 60% of the global solar power capacity was distributed amongst China, mainland USA, and Japan [10]. As shown in Fig. 2.1, these regions are located in a relatively narrow band of latitudes between 20° and 50°. Within these regions, maximization of solar irradiance requires solar panels to be placed at an angle of attack of 30° ± 15° based on the time of the year [32]. As will be discussed in detail later, the relatively high pitch angles results in increased loads compared to solar panel installations closer to the equator, requiring strong, yet costly, support structures [11–13].

A typical solar panel, as seen in Fig. 2.2, consists of an array of photovoltaic cells mounted to a support structure held in place by a central pylon. The structural system also houses the electrical components required to transfer the electricity generated by the panel to a power distribution grid. Sun tracking solar panels use actuators that change the relative orientation of the panel as part of the structural support systems. In such cases, the actuators must be sized appropriately to resist the expected wind loads while maintaining tracking accuracy. Photovoltaic cells are cast in rectangular shapes to minimize the ratio of non-photovoltaic-to-photovoltaic surfaces, resulting in the rectangular shape observed in almost all solar panel designs. The physical size of the solar panel in terms of the panel length and width varies between 1 m to 10 m based on the application, with the smaller panels used for residential or commercial installations and the larger panels used in utility grade installations [17, 28, 33].

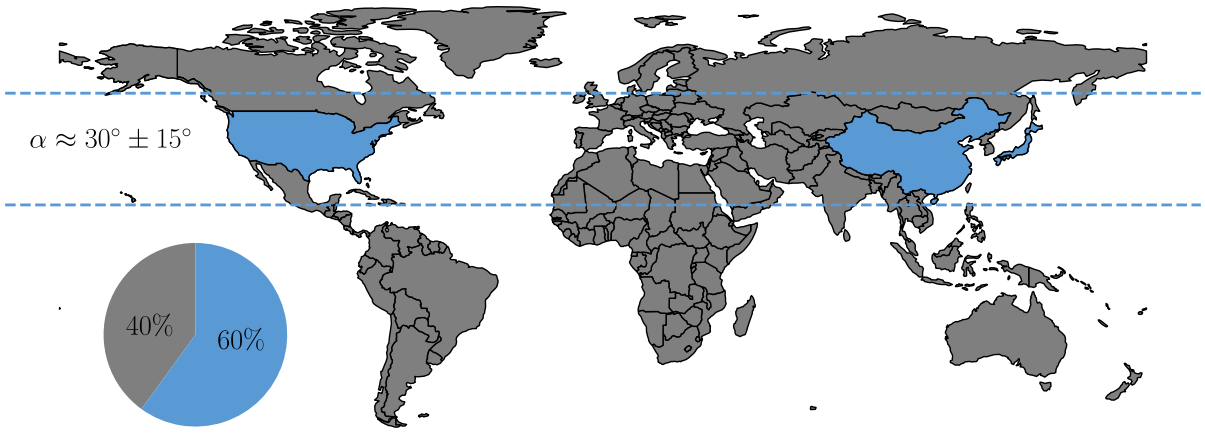


**Figure 2.1:** World map showing top three energy solar energy producing regions in 2021. Inset pie chart indicates the power capacity division between top three solar energy producers and the rest of the world. Angle of attack of solar panels within the latitudes indicated by the dashed lines is defined as $\alpha$. Data sourced from [10].

**Figure 2.2:** Pole mounted solar panel with dual-axis solar tracking capabilities. (© 2016 Adsala, original shared under CC BY-SA 4.0)

Solar panels can be deployed in many locations from urban areas to harsh and remote regions, with varying environmental conditions. In urban environments, solar panels are typically placed on top of buildings to maximize the incident solar irradiance, while ground mounted solar panels are more common in rural and isolated areas where large open spaces are readily available (e.g., grasslands, tundras, deserts, etc). In some cases, solar panel fields can also be placed on floating or static offshore structures, when the availability of open land is scarce [9, 34]. Notably, significant climate variations between installations sites has led to a number of case studies to assess the feasibility of specific locations [e.g., 35–39].

Generally, building mounted solar panels are subject to both the atmospheric boundary layer (ABL) and disturbances due to nearby buildings, while ground mounted solar panels on open land are largely subjected to the lower portion of the ABL. Solar panels are also exposed to extreme weather events, such as powerful gusts during storms and down bursts, which can bring precipitation in the form of rain, snow, and hail in addition to the elevated wind speeds and sudden variations in wind direction. In arid environments, particulates can also collect on the solar panel lowering its efficiency (known as soiling), which can be exacerbated by heavy winds and gusts during storm conditions [40]. Structural damage due to extreme winds and gusts can be mitigated through the use of locking devices or ground tethers [16, 41]. In the case of actuated solar panels, the panel can be placed in a flat position known as the stow position, in order to reduce wind loads [42, 43].

As seen in Fig. 2.3, solar panels are placed in grid formations in large flat areas, such as on building roofs or rural farm lands in order to increase the total generated power. The perimeter solar panels undergo the largest mean wind loading in terms of lift and drag compared to the internal solar panels [44], while the associated sheltering effect decreases the loading on the internal structures [45, 46]. The use of wind fences (perimeter or internal) and increased field

(a) (b)

**Figure 2.3:** Solar panel arranged in grid formations on (a) building roofs and (b) farm land [9].

density can be effective in the reduction of loads experienced by solar panel arrays [46]. Compared to solar panel grids, an isolated solar panel experiences greater peak loads [47], which provides a conservative model for examination of wind loading.

## 2.2 Environmental Flow Characteristics

Solar panels are generally subjected to the ABL, with ground mounted solar panels exposed to the lower portion of the ABL. Unsteadiness is introduced by atmospheric turbulence, often abstracted as wind gusts associated with sudden localized changes in the incoming velocity profile and wind direction. This section provides a brief overview of the in-field characterization and laboratory modelling of the ABL and gusts. For a full description of the topic, the reader is directed to the works by Garratt [48], Azad [49], and Stull [50].

### 2.2.1 Atmospheric Boundary Layer

Atmospheric circulation, driven by mechanical and thermal effects, results in flow of air over the Earth's surface. Due to the no-slip condition, the wind speed above the ground will increase with increasing height. The lower portion of this moving air region, where viscous effects are significant due to the ground-air interaction, is known as the atmospheric boundary layer. The ABL is further divided into the inner and outer layer, with the inner layer consisting of the fluid that directly borders the Earth's surface, which has a thickness of approximately 100 m [49]. Wind speed measurements of the inner layer require vast flat open geography. For example, the Surface Layer Turbulence and Environmental Science Test (SLTEST) site in Utah's northwestern desert region allows the ABL to develop undisturbed over a distance of approximately 100 km [e.g., 51–53].

Time-averaged velocity and turbulence intensity profiles within the inner layer of the ABL measured at the SLTEST site by Monty *et al.* [52] and Hutchins *et al.* [54] are presented in Fig. 2.4 with respect to the surface normal direction, $y$. As the measurements were collected under different

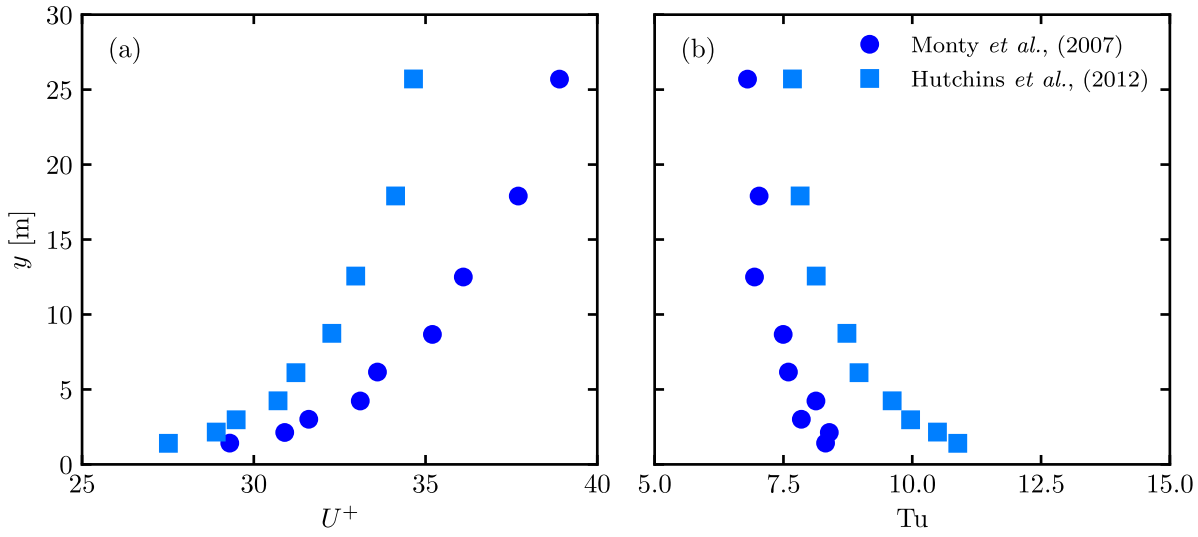


**Figure 2.4:** Experimental measurements of the ABL at the SLTEST site in Utah's west desert by Monty *et al.* [52] and Hutchins *et al.* [54]. (a) Inner scaled velocity and (b) turbulence intensity profiles.

atmospheric conditions, the scaled velocity and turbulence intensity profiles do not collapse. The velocity profile is scaled by the friction velocity, $U_\tau = \sqrt{\tau/\rho}$, where $\tau$ is the wall shear stress and $\rho$ is the fluid density. As accurate values of wall shear stress are difficult to measure, an estimation is obtained using the Clauser method [55] by Monty *et al.* [52] and peak Reynolds shear stress [56] by Hutchins *et al.* [54]. In both cases, the uncertainty level of $U_\tau$ was approximately 10 %. As expected, the ABL velocity profiles in Fig. 2.4a exhibit a power-law profile observed for turbulent boundary layers, with the highest velocity wall normal gradients observed near the surface.

The turbulence intensity profiles (Fig. 2.4b) also resemble a turbulent boundary layer power-law profile. Notably, both Monty *et al.* [52] and Hutchins *et al.* [54] collected these measurements under calm weather conditions, leading to relatively low turbulence intensities between 7.5 % to 10.5 %. In comparison, turbulence intensities as high as 30 % have been observed under extreme weather conditions [57]. The integral length scale, $\mathcal{L}$, at a height of $y = 10$ m ranges between 62 m to 144 m [58, 59]. At the same wall normal distance, the Kolmogorov length scale, $\eta$, ranges between 1 mm to 10 mm [60–62]. For a large solar panel with a width of 10 m, the integral length scales are approximately between 6 to 14 panel width, while the Kolmogorov length scales range between 0.01 % to 0.1 % of the panel width.

Time-averaged velocity and turbulence characteristics of the ABL must be closely modelled in order to accurately estimate the wind loads on solar panels. The most simple ABL mean velocity profile is a power-law profile, which is expressed as

$$\frac{U(y)}{U(y_0)} = \left(\frac{y}{y_0}\right)^{\alpha_0}, \tag{2.1}$$

where $U(y)$ is the streamwise wind speed at height $y$, $U(y_o)$ and $y_0$ are the reference values for velocity and height, respectively, and $\alpha_0$ is the exponent based on ground roughness. The power-law profiles show good agreement with in-field velocity measurements at heights between 30 m to 300 m [63]. Conventional solar panels are typically located at heights below 30 m, however, the power law velocity profile has been widely used in a number of previous works studying wind loads on solar panels due its simplicity [e.g., 28, 33, 45, 47, 64–66].

The lower height limitation of the power-law profile can be extended with a log-law velocity profile [48], formulated as

$$U(y) = \left(\frac{U_0^*}{k}\right) \ln\left(\frac{y - y_d}{y_0}\right), \tag{2.2}$$

where $U_0^*$ is the surface friction velocity, $k$ is the von Karman constant, and $y_d$ is the zero-plane displacement. The log-law profile compares well against in-field velocity measurements at heights as low as 0.5 m [67] and up to 200 m [48], however with very rare exceptions [e.g., 68], the log-law profile is rarely used due to the added complexity compared to the power-law. The Deaves-Harris (DH) profile deserves a mention as it can model the full ABL velocity profile by using three scaling parameters [69]. The DH profile has similar accuracy as the log-law and power-law in the inner layer [70], however, it shows better agreement with measured mean wind speeds in the outer layer [71]. Civil codes have incorporated the use of the Deaves-Harris profile, but the power-law and log-law profiles are more convenient and has been more commonly employed to model steady wind loads on photovoltaic installations [63, 72].

Similarly, a power-law profile is the most common method of approximating the turbulence intensity profile of the ABL and has been adopted into North American building codes for wind load estimations. Mier-Torrecilla *et al.* [66] determined that the wind load estimates on solar collectors, which are similar to solar panels in terms of structure, from numerical and experimental setups showed good agreement when using power-law velocity and turbulence intensity profiles. The Engineering Science Data Unit (UK) provides empirical measurements that can be used to validate wind tunnel turbulence intensity profiles, which has been implemented in some recent studies with success [e.g., 28, 42, 47, 64].

The neutrally buoyant ABL can be modelled in laboratory settings with appropriate upstream turbulence generating devices. Adjustable spires and small roughness elements can be used to create the required velocity and turbulence intensity gradients in wind tunnels with a high degree of accuracy to measured values [60, 73, 74]. One of the major limitations when experimentally modelling the ABL is the need for a relatively large test section in order to allow flow to fully develop into a characteristic ABL. The test section lengths are typically between 10 m to 20 m with the cross section on the order of a few meters [e.g., 47, 65]. Adjustments to the velocity and turbulence intensity profiles can be made relatively easily by the placement of the spires and roughness elements, however, independently controlling the integral length scales simultaneously is difficult. A convenient alternative is to adjust the characteristic length scale of models, in order to precisely vary the normalized integral length scales [e.g., 42, 64]. The turbulence characteristics of the ABL recreated in wind tunnels can be verified through the use of the von Karman [75] and Davenport [76] energy spectra.

### 2.2.2 Gusts

Gusts are large deviations from the average wind speed that occur suddenly, which can impart significant dynamic loads on civil structures. Coherent motions in the ABL result in gusts, the intensity of which will be dependent on the local weather and topological features. Consideration of gusts in the study of wind loads on civil structures is particularly important as the forces scale with the square of the wind speed. Dynamic loads on civil structures due to gusts are approximated in civil codes by using a constant factor to scale the steady wind loads, however, this method ignores the transient structural response and fluid-structure interactions [77].

Gusts can be described by their magnitude, rise time, and durations. The gust magnitude is defined by a ratio between peak wind speed and average wind speeds. The average wind speed, $\overline{U}_0$, measured over a sampling period, $T_s$, is

$$\overline{U}_0 = \frac{1}{T_s}\int_0^{T_s} U(t)\,\mathrm{d}t, \tag{2.3}$$

where $t$ is the time, $U(t)$ is the instantaneously measured wind speed. The peak gust speed, $\hat{U}_g$, is defined as the maximum of a moving average of $U(t)$ with an averaging period of $t_s$, determined over $T_s$:

$$\hat{U}_g = \max_{t_0\in[0,T_s-t_s]} \frac{1}{t_s}\int_{t_0}^{t_0+t_s} U(t)\,\mathrm{d}t, \tag{2.4}$$

where $t_0$ is the start of the moving average period. The gust magnitude over the duration $T_s$ is then expressed non-dimensionally using the gust factor [78]:

$$\mathrm{G} = \hat{U}_g/\overline{U}_0. \tag{2.5}$$

The moving average and sampling periods were previously defined in civil codes with significant regional variations. In a push for standardization, values of $t_s = 3$ s and $T_s = 10$ min are suggested by the World Meteorological Organization [79] and North American building codes [78, 80]. The gust rise time, $t_{gr}$, which is the time taken for the wind speed to increase from a steady value to a peak value, and gust duration, $t_{gd}$, which is the length of time where the velocity remains elevated, define the gust time scales. Notably, $t_s$ is different from $t_{gr}$ and $t_{gd}$ as the former is a predetermined time period for quantifying the gusts, while the latter are physical properties that are specific to each gust event. The rise time and durations for a single gust event can be non-dimensionalised as $\mathrm{t}^*_{gr} = t_{gr}\hat{U}_g/c$ and $\mathrm{t}^*_{gd} = t_{gd}\hat{U}_g/c$, where $c$ is the panel width (also defined as chord length). When considering wind loads on civil structures, the magnitude and rise time are important as these parameters directly govern the transient structural loading and response [81].

Gust factors between $1 < \mathrm{G} \leq 4$ have been observed throughout the world and exhibit significant regional variations, as expected. Prior to standardization of $t_s$ and $T_s$, gust factors between 1 to 2 were reported as early as the 1960s [82]. More recently, Jungo *et al.* [83] observed gust factors between $1 < \mathrm{G} \leq 4$ in Switzerland. Furthermore, extreme gust factors up to $\mathrm{G} = 10$ were also observed, but were considered to be outliers. In Guangdong, China, gust factors exhibited significantly less variation and were within the range $1.25 \leq \mathrm{G} \leq 2.25$ [57] during storms. In Ontario, Canada, gust factors were similar to those observed in Switzerland without any extreme

deviations [84]. In New York, USA, gust factors that ranged between $1 < G \leq 1.8$ were reported by Hu *et al.* [78] using hourly and daily meteorological observations collected over nearly five decades, covering both typical and storm like conditions.

Gusts are commonly characterized by their durations, however, gust rise times are important as the rate of increase of the velocity affects the transient loading on civil structures. Similar to gust factors, gust rise times also show significant regional variance. In all cases reviewed here, the gust rise time probability distributions follow a log-logistic distribution and the gust rise time range that occurs with an associated minimum probability greater than 1 % is used to characterize the full scale parameter space. In field measurements of gust rise times are limited; some observed maximum gust rise times, $t_{gr,\max}$ and maximum peak gust speeds, $\hat{U}_{g,\max}$ are tabulated in Table 2.1. Notably, the gusts observed in Newcastle, Australia were significantly weaker, perhaps due to the measurement site being in an urban area as opposed to rural areas used by other studies [78, 85, 86]. Results presented in Table 2.1 are collected at heights relevant to wind turbines (60 m to 100 m), with the exception of Rakib *et al.* [86], who collected wind speed data at 15 m, which is more relevant to utility-scale solar panel structures. Therfore, the measured maximum rise times and peak gust velocities correspond to a non-dimensional parameter range of $0 < t^*_{gr} \leq O(10^2)$, though additional wind speed measurements at lower heights is needed for improved estimates of gust rise times relevant for solar panel structures.

Gusts can be modelled using analytical, numerical, and experimental methods, either as single discrete events characterized by a sudden change in velocity or continuous gusts through stochastic velocity changes. Continuous gust events are defined by spectral energy distributions of the atmospheric turbulence for the three velocity components [88]. Experimental modelling is typically limited to single component discrete gusts, while use of analytical or numerical modelling allows for continuous gusts to be modelled for all three velocity components simultaneously. As the present study mainly focuses on the effect of discrete gusts using experimental methods, the methodology related to physical gust modelling in wind tunnels or other experimental facilities will be discussed in more detail. Notably, gusts characteristics and the effect on various submerged obstacles have been widely explored using analytical [e.g., 89–93] and numerical methods [e.g., 94–96].

Experimental modelling of gusts can be achieved through the use of flow control hardware placed either upstream or downstream of the test section. Towing tanks, where a model is accelerated rather than the fluid, may also be used with appropriate inertial load characterization. A simple method of generating gusts include the use of programmable controllers to vary the

**Table 2.1:** In-field measurements of maximum gust rise times and peak gust velocities

| | Location | $t_{gr,\max}$ [s] | $\hat{U}_{g,\max}$ [m s$^{-1}$] | $t^*_{gr,\max}$ [a] |
|---|---|---|---|---|
| Rakib *et al.* [86] | Newcastle, Australia | 9.5 | 7.5 | 71 |
| Hu *et al.* [78] | New York, USA | 40 | 17.5 | 700 |
| Bardal & Sætran [85] | Froya, Norway | 32 | 27 | 864 |
| Letson *et al.* [87] | Perdigao, Portugal | 75 | 15 | 1125 |

[a] Based on a panel width range of 1 m to 10 m

test section flow speed, however, due to the greater inertia of fans and motors in larger wind tunnels, rapid changes in freestream speeds at timescales relevant to photovoltaic installations are nearly impossible. The most common method of creating gusts is to employ active louvres, as shown in Fig. 2.5a, that are able to operate independent of the wind tunnel fan [e.g., 88, 97, 100, 101]. Active turbulence grids consisting of arrays of individually actuated diamond plates (Fig. 2.5b), known as Makita grids, can be used to precisely vary the tunnel blockage resulting in rapid changes of freestream characteristics [102, 103]. Makita grids simultaneously generate multiple length scales within the test section due to vortex shedding from each diamond element, flapping of diamond elements, and large sections of the grid opening and closing. More recently, small programmable fans in place of individual actuated elements (Fig. 2.5c) have been used to create gusts with prescribed length scale profiles, amplitudes, and frequencies [99]. Tow tanks with models that can be accelerated allow for the model to undergo impulse loading, which is analogous to a gust event. Moving model setups are typically used with water tunnels in order to minimize required model accelerations. Transverse gusts can also be created in tow tanks by passing the model through stationary free jets, which creates a gust with a sinusoidal velocity profile [104].

In addition to a sudden changes in local wind speeds, gusts may also manifest as a local change in wind direction, particularly during inclement weather events. To the knowledge of the author, in field characterizations and analytical models of sudden wind direction variations have not been reported in literature at timescales relevant to flow timescales (seconds). However, a sudden wind direction change is defined in the IEC 61400-1 international standard for wind turbine installations as a wind direction change of 30° occurring over 6 s. It is reasonable to assume that utility scale photovoltaic installations may also be subjected to the same wind direction changes, at least when considering utility scale installations, which are more comparable to wind turbine structures in height. Based on publicly available meteorological data from Environment Canada collected at weather stations in Ontario, the average wind speed is approximately 5 m s$^{-1}$, comparable with observations in New York State collected over two decades [105]. Thus, for a solar panel width between 1 m to 10 m as previously considered, the non-dimensional rise time for sudden wind

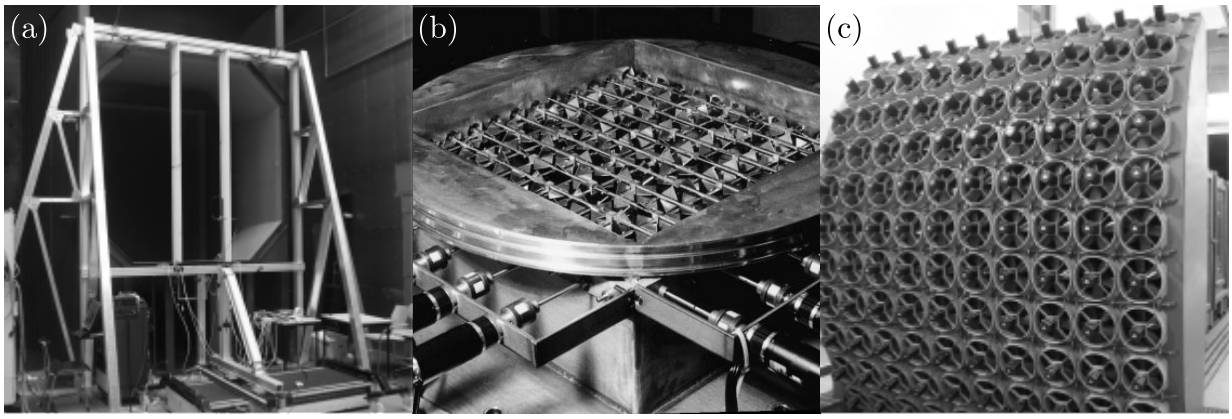


**Figure 2.5:** Wind tunnel gust generation systems. (a) Oscillating airfoil/flat plate system [97] (b) Makita grid system [98] and (c) array of small fans in an open loop system [99].

direction change, $t^*_\beta$, is estimated to be between 3 to 30, which is notably lower than in-field rise time range for a sudden wind speed variation (Table 2.1). As was the case for freestream speed variations, sudden wind direction variations can be modelled experimentally through upstream flow control mechanisms to impulsively vary the local flow direction [e.g., 97, 106–108] or by rotating the model [109]. Compared to an incoming flow direction variation, larger wind direction changes are possible with model rotating systems, as long as model vibrations are minimized and inertial loads are characterized through tests under quiescent flow conditions.

## 2.3 Aerodynamics of Finite-span Inclined Flat Plates

In this section, the aerodynamics of photovoltaic installations are discussed in terms of the flow development, forces, and the associated fluid-structure interactions under steady incoming flows. As the contribution of the support structure to the overall wind loading is expected to be minimal compared to panel loading and due to geometric similarity of conventional solar panels to flat plates, the following discussion is focused on the aerodynamics of flat plates under free flight conditions, while ground effect aerodynamics is discussed in Section 2.4. The problem definition is outlined in Section 2.3.1, while the following sections discuss the effect of parameters relevant to solar panel installations on both steady and unsteady finite-span inclined flat plate aerodynamics.

### 2.3.1 Problem Description

The Cartesian coordinate system and the parameters pertaining to a finite-span inclined flat plate placed in close ground proximity are shown in Fig. 2.6. The incoming velocity profile defined by $U(y)$ is characterized by its freestream velocity, $U_\infty$. The solar panel geometry is defined by its chord length (equivlanet to panel side length), $c$, width, $b$, and thickness, $d$. The panel orientation with respect to the freestream flow direction is defined by the angle of attack, $\alpha$ and the wind direction (yaw angle), $\beta$. The origin is located at the plate centre and the coordinate system remains fixed through plate rotations.

The pressure coefficient, $C_p = 2\Delta p/(\rho U_\infty^2)$, describes the relative pressure distribution on the panel and the surrounding flow field, where $\Delta p$ is the local gauge pressure and $\frac{1}{2}\rho U_\infty^2$ is the dynamic pressure. The components of forces and moments along each axis $i = x,\ y,\ z$ are defined by $F_i$ and $M_i$. These forces and moments are non-dimensionalised as $C_{F_i} = 2F_i/(\rho U_\infty^2 bc)$ and $C_{M_i} = 2M_i/(\rho U_\infty^2 bc^2)$. Naturally, colloquial descriptions of loading components are more intuitive, therefore forces acting along $x$, $y$, and $z$ are described as drag, lift, and side forces, and denoted by $D$, $L$, and $S$, respectively. Similarly, moments about $x$, $y$, and $z$, are described as roll, yaw, and pitch and denoted by $M_R$, $M_Y$, and $M_P$, respectively.

### 2.3.2 Effect of Panel Geometry

The main non-dimensional parameter that characterizes the shape of the panel is the aspect ratio of the wetted surface, $AR = b/c$. The use of square panels allow for higher field densities in grid arrangements, however, the use of wider panels lowers the average wind speed leading to wind

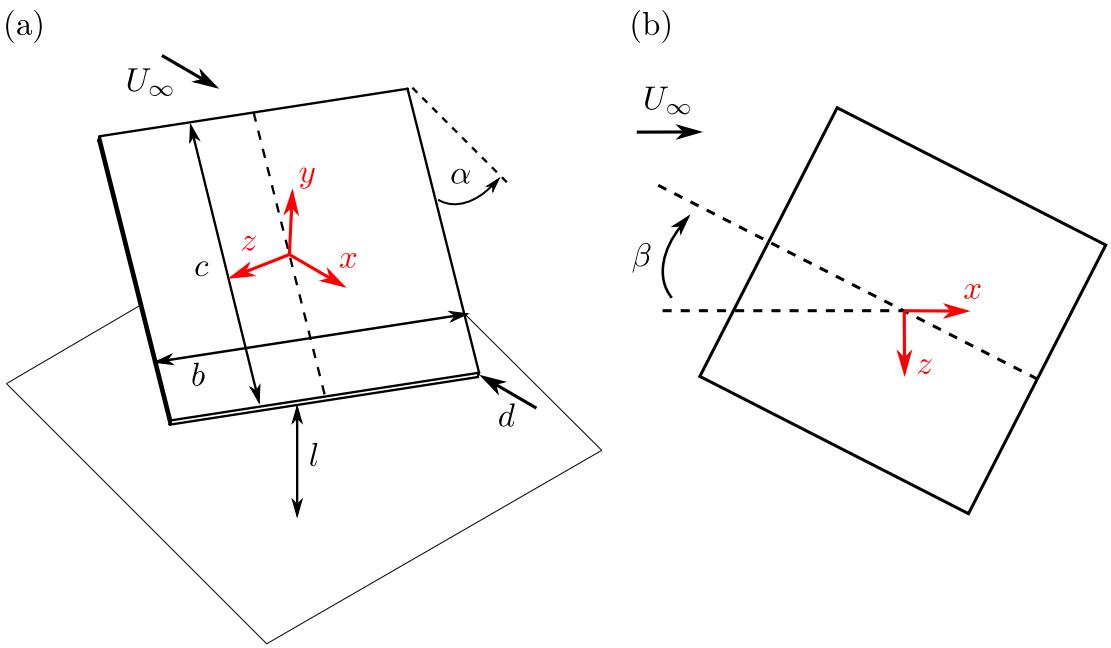


**Figure 2.6:** Schematic of a finite-span inclined flat plate in close ground proximity describing the Cartesian coordinate system and relevant parameters. (a) Isometric view and (b) top view.

load reduction [110]. A significant number of studies have utilized the square panel geometry to investigate wind loading and the dynamic response of isolated solar panels or solar collectors [24, 28, 43, 111, 112]. Pfahl *et al.* [110] employed a relatively large aspect ratio range between 0.5 to 3 in order to study the effect of AR on the wind loads. They developed a number of correlations for all axial forces and $C_{M_Y}$ in addition to all base moment coefficients, $C_{M_{B,i}}$, for critical loading configurations (Section 2.3.3) [110]. Under headwind conditions ($\beta = 0°$), the base yaw moment, $M_{B_y}$, decreased with increasing AR for both upright ($\alpha = 90°$) and stowed elevation angles ($\alpha = 0°$). Under crosswind conditions ($\beta = 90°$), a similar decrease was observed in the orthogonal base moment, $M_{B_x}$. Notably, the peak loading coefficients were more sensitive to variations in AR compared to mean values [110].

Though the developed correlations between aspect ratio and loading components are of practical importance, a physical understanding (i.e., link between loading and flow development) of the effects of aspect ratio on finite-span inclined flat plate aerodynamics was lacking until recently. The main difference in the aerodynamics between two-dimensional and finite-span inclined flat plate stems from the influence of tip effects on the overall flow development. To provide clarification on tip effects and relation to loading, DeVoria & Mohseni [19] examined the flow and forces on flat plates of $0.75 \leq \text{AR} \leq 2.5$ for $0° \leq \alpha \leq 40°$ at $\text{Re}_c = 80\,000$, which was corroborated by Linehan & Mohseni [23] in the same facility for $0.75 \leq \text{AR} \leq 3$, $0° \leq \alpha \leq 40°$, and $\text{Re}_c = 100\,000$. For $\text{AR} \leq 1$, the downwash induced by the tip vortices resulted in leading-edge shear layer reattachment near the trailing edge, facilitating smooth flow at the trailing edge, which led to delayed stall and higher maximum lift coefficient compared to plates of $\text{AR} \geq 2$ due to establishment of a Kutta condition. Notably, a relatively high lift coefficient and delayed stall has been observed up to $\text{Re}_c > 10^6$ [110], which suggests that the same mechanism

persists for a relatively large range of Reynolds numbers. Similar observations were made by Shademan & Naghib-Lahouti [21] in a numerical study utilizing aspect ratios of AR = 0.5, 2, and 5 for $75\,000 \leq \mathrm{Re}_c \leq 150\,000$ and $\alpha = 30°$. Overall, the results point to a practical demarcation between the low and high AR ranges with AR $\leq 1$ and AR $\geq 2$ defining these ranges, respectively. Results from other experimental and numerical works examining aerodynamics of finite-span flat plates have generally agreed with these observations [15, 20, 28].

A high AR is favourable for reducing the load on the elevation drive that controls $\alpha$ [113], which is important as most commercially available single and dual axis solar trackers employ elevation drives. Grid installation designs have exploited this by employing panels with higher AR, as seen in Fig. 2.3. Variations in the AR causes the moment arms to change, which changes relative and absolute magnitude of some loading components. Therefore, the AR must be strategically chosen based on the panel design and installation site conditions in order to lower load requirements on specific drives, foundations, and pylon structures. In addition to feasibility studies at specific installation sites, optimization schemes for the choice of AR have been developed for critical loading configurations (Section 2.3.3) [114].

Multiple modules of solar cells may be used for the final solar panel assembly creating small inter-panel gaps. These gaps lead to the formation of localized free jets and associated coherent structures that develop downstream of the panel [115]. For gap area of up to 8 % of the total panel area, the drag force increases with increasing gap size, due to the overall increase in the effective wetted area and decrease in the static pressure on the leeward surface associated with the formation of free jets at the gaps [28, 115]. Peterka & Derickson [111] found that panel arrays with gap areas of up to 15 % of the total panel area can be treated as a solid surface for estimating drag forces. With further increase in gap size, the panels are expected to behave as individual panels rather than a collective, however, such designs are not common due to the inefficient use of space.

### 2.3.3 Effect of Panel Orientation

Wind loading of solar panels is strongly dependent on the relative orientation of the panel to the incoming flow. As the elevation angle and wind direction changes, some loading components increase, while others decrease much like the effect of AR on wind loads. Square solar panel orientations that maximize each loading component have been identified for steady incoming flow and are summarized in Table 2.2 [43, 110, 111].

**Table 2.2:** Critical loading configurations for steady incoming flow [43, 110, 111].

| Component | $\alpha$ | $\beta$ |
|---|---|---|
| $F_D$ | 90° | 0° & 180° |
| $F_S$ | 90° | 45° & 135° |
| $F_L$ | 30° | 0° & 180° |
| $M_R$ | 30° | 120° |
| $M_Y$ | 90° | 60° |
| $M_P$ | 90° | 0° & 180° |

The attendant changes in the loading with respect to the angle of attack closely resembles the trends observed in flat plate studies. Solar panels elevation angles span a relatively large range of $0° \leq \alpha < 90°$ [e.g., 47, 116] based on optimal solar irradiance angles for a given latitude [117]. Notably, $\alpha$ extrema are used for panel stowing during extreme weather events ($\alpha = 0°$) or closer to the Earth's poles ($\alpha \to 90°$). Drag is maximized when the plate is normal to the flow ($\alpha = 90°$) due to maximum projected area, with maximum drag coefficients falling between 1 to 1.2 [18, 47]. Lift increases linearly at a rate of approximately $2\pi$ with respect to $\alpha$ and reaches a maximum at moderate angles of attack ($10° \leq \alpha \leq 45°$), with the the maximum lift coefficient and corresponding angle of attack dependent on the AR. For AR = 1, the lift is maximized at $\alpha \approx 30°$, however, finite-span flat plates and thin cambered airfoils in unsteady freestream flows have been reported to exhibit a post-stall maximum in the lift coefficient between $40° \leq \alpha \leq 50°$ [118, 119]. This difference between flat plates and solar panels may be attributed to the effect of the support structure and proximity to the ground, however, the exact cause remains unknown.

As the yaw angle is increased from $\beta = 0°$ to 90°, effective $\alpha$ tends to zero, resulting in a decrease in lift and drag coefficients from their maximums at $\beta = 0°$ [26, 28, 31]. As expected, at $\beta = 90°$, the lift is zero, and drag is minimal (friction drag). Consequently, all moments are also zero barring any sting or geometrical effects due to use of full detail scaled down solar panel models [25, 26]. The side force coefficient is sinusoidal with respect to $\beta$, with near zero values at $\beta = 0°$, 90°, and 180° and has opposingly signed peaks at $\beta = 45°$ and 135° [26, 46]. The roll and yaw moment coefficients follow a similar trend as the side force with respect to $\beta$, while the base pitch moment is negatively correlated with lift and drag coefficients [26, 28, 46]. Examination of the effect of $\beta$ on finite-span inclined flat plates have been largely limited to force measurements and the associated physical mechanisms remains to be investigated and linked to loading trends, particularly for low AR panel configurations.

Some insight into the physical mechanisms associated with $\beta$ variations can be gained from studies that considered a "side-slip" configuration. In such cases, $\alpha$ is kept constant with $\beta$, essentially rotating the flat plate normal to its flat surface. Devoria and Mohseni [19, 120] measured forces on and flow around a square flat plate inclined at $\alpha = 35°$ for $\beta < 35°$ at $\mathrm{Re}_c = 80\,000$. As $\beta$ increased, the circulations associated with the tip vortices decreased and the "pinning" effect on the leading-edge shear layer reduced, as marked by disappearance of stall cell flow patterns [121]. As expected, the flow development about the midspan became increasingly asymmetric with increasing $\beta$. In general, for relatively low $\beta$ values, where the change in $\alpha$ is minimal, the rate of change in loading between side-slip and yawed configurations were comparable [25, 26, 120, 122].

### 2.3.4 Effect of Reynolds number

The chord based Reynolds number is typically defined as $\mathrm{Re}_{U_h} = U_h c/\nu$ for flow past a solar panel, where $U_h$ is the incoming streamwise velocity at the elevation axis. In comparison, inclined flat plate studies utilize $\mathrm{Re}_c = U_\infty c/\nu$. Given the widely varying size of solar panels and atmospheric conditions, the operational $\mathrm{Re}_{U_h}$ range is estimated to be between 1 to 25 million [72, 116]. The stowed configuration has been used as a representative case for studying the effect of the Reynolds number as stowing is used to reduce wind loading under extreme weather conditions, though lift

forces may be generated due to support structures themselves or flow asymmetry introduced by the supports [24, 116]. Emes *et al.* [24] investigated the effect of Reynolds number for $\mathrm{Re}_{U_h} = 0.88$ and 1.24 million and found that the increase in peak lift coefficient ranged between 13 % to 21 % depending on the disturbance environment. Due to the experimental design, the effect of the Reynolds number could not be decoupled from the changes to the turbulence intensity, yet Emes *et al.* [24] concluded that Reynolds number effects on wind loading are expected to be less significant compared to turbulence intensity, which requires additional validation. Pfahl & Uhlemann [116] found that the wind loading coefficients were Reynolds number independent for $\mathrm{Re}_{U_h} = 3.2$ to >25 million in the stow position.

The effect of Reynolds number on the solar panel drag in the stow position is expected to be similar to the drag on a smooth flat plate at zero incline albeit with support structures Fig. 2.2. Though the support structure designs can vary, the form drag of support structures are expected to be largely Re-independent, with pressure drag dominating over the friction drag of support structures. For the operational range of solar panel Reynolds numbers, the state of the boundary layer is expected to be turbulent for a significant portion of the panel. For the turbulent regime the drag coefficient on flat plate is proportional to $\mathrm{Re}_c^{-1/7}$ [123]. These theoretical results were experimentally corroborated by Mueller [124] by drag measurements on a flat plate with AR = 1 for various $\mathrm{Re}_c$ at $\alpha = 0$. Notably, measured $\mathrm{C}_D$ values when $\mathrm{Re}_c < 50\,000$ were larger than theoretical values, but at higher Reynolds number the experimental results showed close agreement with theoretical results.

Investigations of Reynolds number effect on wind loads at non-zero elevation angles are currently lacking for solar panels, however, Mueller [124] also reported Reynolds number ranges for various $\alpha$ where $\mathrm{C}_L$ and $\mathrm{C}_D$ of an inclined flat plate became Reynolds number independent. With increasing $\alpha$, the range of Reynolds numbers where the loading was constant increased. This is attributed to the fixation of the separation point at the leading edge and the relatively greater contribution of pressure drag to the total drag at higher $\alpha$ [124]. For $\alpha = 10°$, $\mathrm{C}_L$ and $\mathrm{C}_D$ were constant when $\mathrm{Re}_c > 20\,000$. By ensuring that the Reynolds number is greater than this minimum for a given elevation angle, traditional wind tunnels can be used in place of atmospheric wind tunnels [e.g., 47] or high pressure wind tunnels [e.g., 116] for investigating solar panel aerodynamics.

### 2.3.5 Effect of Gusts

Gusts may cause transient loading outside of photovoltaic structural operation envelopes which can result in significant damage and downtime. In practice, gust loads are approximated through the use of scaling coefficients [125], however, this ignores any transient effects stemming from fluid-structure interactions. Pfahl *et al.* [16] investigated the gust response of an in-field sun-tracking square solar collector for the purpose of designing a shock-absorber wind load reduction system. Naturally, in-field conditions were not repeatable, limiting the insights to be gained from linking the loading trends to flow behaviour. Investigations focusing on the interaction between gusts and solar panel geometries are scarce, however, the flow development and loading due to gusts interacting with a free inclined plate has been the focus of a number of recent studies due to relevance in flight applications [e.g., 126–129].

Experimental investigations examining the effects of freestream accelerations on finite-span inclined flat plates have typically utilized ramp accelerations, which is typical of naturally occurring gusts [78]. For various plate configurations across different facilities, a generally common transient flow development has been observed [130–133]. As the freestream velocity ramps up, there is increased vorticity generation at the leading edge, producing a leading edge vortex (LEV) that initially remains bound to the suction side. The LEV can grow in size up to half a chord length before moving away from the plate. As the primary vortex convects downstream, interaction with plate bound vorticity leads to a formation of a primary trailing edge vortex (TEV), which rolls onto the suction side surface prior to its convection downstream. In some cases, a secondary LEV may form and convect downstream due to interaction of the primary TEV with the plate bound vorticity. Notably, the vortex formation and evolution process has been shown to be independent of the initial conditions, i.e., starting from rest or from a non-zero freestream velocity [128, 134]. The periodic shedding of LEVs and TEVs is characterized by the non-dimensional frequency, Strouhal number, $\mathrm{St}_c = fc/U_\infty$, where $f$ is the shedding frequency and $U_\infty$ is the final steady velocity. Shedding frequencies between 0.25 to 0.27 have been previously observed over accelerating inclined flat plates [128, 133], which shows good agreement with expected vortex formation timescales [135].

The aforementioned vortex formations and evolution over the plate suction side leads to notable transient loading trends. Given the similarity in the flow development across a number of studies, some common features are also observed. As the plate accelerates, there is an increase in plate loading followed by oscillations in the loading magnitude with a frequency that matches the vortex shedding frequency [128, 133], producing local peaks in the loading magnitudes. Notably, oscillations in the drag coefficient occurred at approximately double the frequency due to alternative shedding of LEVs and TEVs, which occurs with a phase difference of approximately $\pi/2$ [128, 136]. Subsequent loading magnitude peaks decay exponentially [128] and loads return to the steady state level corresponding to the final Reynolds number. In experimental investigations, transient loading peaks that are twice the steady state levels have been observed [128, 129, 133] for rise times that are $O(1)$.

Deviations from the previously introduced flow development and structural loading trends occur with aspect ratio, angles of attack, and gust accelerations or rise times. The AR determines the spanwise portion of the LEV affected by the tip vortices and therefore the force history following the gust event. With decreasing AR, the wake topology becomes increasingly three-dimensional and the tip vortices act to keep the LEV attached, minimizing loading oscillations [130, 131, 137]. The interaction of the tip vortices with leading and trailing edge vortices at low AR led to aperiodic shedding, which was not observed for high AR cases [130]. As expected, the angle of attack also has a notable effect on the transient flow development following the gust interaction. At relatively low angles of attack ($\alpha < 10°$), the starting LEV-TEV vortex pair could not be detected and flow remained attached to the plate [133]. For these cases, lift coefficient showed good agreement with Wagner's predictions for an inviscid surging plate [133]. With further increase in $\alpha$, the flow becomes increasingly separated and was characterized by the emergence of secondary and tertiary shedding events, with corresponding oscillations observed in the loading coefficients [133]. Lastly, LEV circulation is proportional to the acceleration magnitude and subsequently produced higher peak loads at higher acceleration [133].

Many investigations into the interaction between a gust and inclined flat plates have utilized accelerating models in water tunnels to create the time variations in the freestream velocity. When a body is accelerated through a fluid, the layer of fluid that is in direct contact with the body must also be accelerated along with the body due to the no-slip condition at the body surface. Therefore, a body accelerated in a fluid requires an additional amount of force compared to a body accelerated in a vacuum. The additional force can be defined in terms of the extra mass of the fluid accelerated with the body and is known as the added mass force. The remaining contributors to the total force are previously shed wake vortices and frictional forces. The contribution due to the vorticity field is referred to as the circulatory force. Pitt Ford & Babinsky [136] found that, following the acceleration phase, the contribution of the bound vorticity was negligible compared to the effect of the LEV and TEV.

The investigations that have been discussed so far were largely concerned with flight applications and thus explored gust rise times that are $O(1)$ [e.g., 128, 129, 131]. Mancini *et al.* [133] demonstrated that as the gust rise times increased from $t^*_{gr} \approx 0.22$ to 11 for the same gust factor, the transient lift coefficient peak of a AR = 4 flat plate model decreased by a factor of three. Notably, at $t^*_{gr} \approx 11$, the lift coefficient amplitude were less than 25% over steady state levels. Further increase in gust rise times are expected to procue a quasi-steady lift response without significant transient loading peaks [131, 133]. Considering that natural gust rise times may be nearly two orders of magnitude higher in a number of locations (Table 2.1) than those employed in the previously mentioned investigations, it would appear that freestream gusts should not be of major concern at least for high AR photovoltaic installations. On the same note, as long as support structures are designed to resist loading at the freestream velocity corresponding to the maximum possible gust factors at the installation site, the structure should resist any transient loading during gusts. However, gust rise times during extreme weather events, which would naturally have lower rise times, have not been comprehensively characterized due to impracticality of in-field measurements, predictability of such events, and terrain variability, though obtaining real-time data under harsh conditions has been the focus of recent studies [e.g., 138]. Standards that define annual operating gusts or gust factors typically underpredict expected structural loading [86, 125], which risks damage during extreme weather events due to undersized support structures. With lower gust rise times for the same gust factors, transient loading peaks notably higher than steady state loads is possible, with potential to cause significant damage and downtime, increasing operating costs.

There is a sizable body of literature on aerodynamics of finite-span inclined flat plate in an accelerating freestream, which is motivated by the wide number of engineering and biological flight applications. In contrast, examination of the effect of a time-varying incident flow direction on aerodynamics of finite-span inclined flat plates have been limited. Notably, unsteady aerodynamics during the interaction between airfoils and inclined plates with oblique [e.g., 139, 140] and transverse gusts [e.g., 141, 142] was recently considered, however, the incident gust direction was fixed. To the knowledge of the author, the effect of a sudden wind direction change representative of an extreme weather event has been carried out for wind turbines based on the IEC-614000-1 standard [143–146]. Though the effects of a sudden change in wind direction on aerodynamics of a solar panel geometry has not yet been directly investigated, some insight in the relevant physics can be gained from studies that focused on impulsively started, rotating finite-span inclined

flat plates. Tudball Smith *et al.* [147] numerically investigated the flow development and lift coefficient of an impulsively rotated AR = 1 plate at $\alpha = 45°$ and $\mathrm{Re}_c = 2500$, with the leading edge aligned with the radial axis. The radius of gyration was varied across infinite (translation) to finite levels to examine the effect on suction side flow development. For all tested cases other than the translating case, spanwise asymmetry in the suction side flow develops post-acceleration with a sizable overshoot in the lift coefficient, approximately 70% above steady state levels at the lowest gyration radius of $0.7c$ from the plate root. Similar assymetrical flow development across the plate span was observed by Garmann & Visbal [148] in a DNS study for a square plate at $\alpha = 45°$, $\mathrm{Re}_c = 1000$, and a gyration radius of $0.5c$, though load estimates were not reported. Based on these results, during a sudden wind direction variation, the LEV over a low AR inclined plate is expected to develop asymmetrically about the plate midspan, thus leading to modified structural loading relative to headwind or tailwind conditions. Furthermore, the influence of the tip vortices for such a wind direction variation remains to be characterized and linked to instantaneous structural loads to further the current understanding of unsteady aerodynamics of low AR inclined flat plates.

## 2.4 Ground Effect

Ground effect (GE) is the phenomenon of modified loading of a structure when in close proximity to a no-slip wall. This phenomenon has been exploited in the design of wing-in-ground aircraft [149] and has been increasingly important in motorsports such as the formula one series [150]. Furthermore, both flying and aquatic animals have also been observed to take advantage of the ground effect by flying closer to the ground while foraging and commuting to minimize the required effort [151]. As solar panels are typically mounted close to a surface, ground effect is an important design consideration. Practically, the lower bound of ground proximity will be limited due to ground clearances required for tilting the panel, maintenance access, and to accommodate growth of plants in mixed use areas.

Ground effect on different geometries, ranging from streamlined bodies such as airfoils [152] to blunt obstacles such as cubes [153] has been investigated. The critical gap distance, where time-averaged loading coefficients deviated from free flight levels, was found to be dependent on the specific geometry. The main governing parameter that characterizes the ground effect is the minimum spacing between a body and the ground, $l$ (Fig. 2.6), normalized by a representative length, known as the gap ratio. In general, the loads increase with decreasing gap ratio due to an increase in static pressure on the ground facing side, as a result of flow restriction between the body and ground, termed the ram effect [154]. This phenomenon has been observed for two dimensional obstacles, such as normal flat plates and cylinders of $10 \leq \mathrm{AR} \leq 26$ [155–157]. For a normal plate, the effect of the ground on the lift coefficient is not observed until very small ground clearances of approximately $l/c \approx 0.1$, due to the narrow ground facing area [157]. The circular and square cylinder critical gap ratios are 0.8 and 1, respectively, when the minimum distance was normalized by the diameter and side length for the corresponding geometry [155, 156]. For these geometries, a more gradual increase in the lift coefficient with decreasing gap ratio was observed due to the larger ground projected area in comparison to the normal plate. The drag coefficient of

a normal flat plate, square cylinder, and circular cylinder decreased with the gap ratio due to a decrease in the pressure difference between the upstream and downstream surfaces as the wake elongated downstream with closer ground proximity. The critical gap ratio was equivalent to the lift results between these geometries.

For a solar panel geometry, the gap ratio is defined as $l/c$ (Fig. 2.6). As solar panels are submerged within the ABL, sufficient decoupling of incoming velocity profile and ground effect is necessary to obtain a clear understanding of the physical mechanisms associated solely with ground proximity variations. For instance, within the limited range of $0.47 \leq l/c \leq 1.8$, peak wind loading coefficients normalized by a reference velocity (see Eqs. (2.1) and (2.2)) increased linearly with $l/c$ for $\alpha = 0°$ and 45° [28, 42]. However, this linear increase in peak wind loads is attributed to the increase in the average streamwise velocity with increasing height, rather than ground effect. Furthermore, in studies motivated by photovoltaic applications, the effect of gap ratio on aerodynamic loading is typically coupled with the inclination angle due to fixed support geometries [26, 30, 31]. Examination of the decoupled aerodynamic effects is critical for developing accurate design guidelines supported by a comprehensive understanding of the flow physics.

Shademan *et al.* [28] and Fukuda *et al.* [15] numerically investigated the influence of $l/c$ decoupled from $\alpha$, on lift and drag coefficients of an inclined plates. Both studies considered flat plates of AR = 1.3 placed at $\alpha = -45°$ and $0.15 \leq l/c \leq 0.78$, for $\mathrm{Re}_c = 9.2 \times 10^6$. As the gap ratio decreased, the recirculation region bordering the back of the plate was repositioned further downstream and was accompanied by a decrease in the pressure difference between the suction and pressure sides. Consequently, the mean lift and drag coefficients decreased with decreasing gap ratio. Ortiz *et al.* [18] collected lift and drag force measurements for flat plates of $0.4 \leq \mathrm{AR} \leq 9$ placed at $-90° \leq \alpha \leq 0°$ for $63\,900 \leq \mathrm{Re}_c \leq 118\,000$ under mild ground effect ($l/c = 0.25$) and free flight conditions ($l/c > 1$). In all cases, the lift and drag coefficients decreased with decreasing gap ratio, however, the relative decrease in the forces depended on AR. Specifically, low AR flat plates exhibited a higher reduction in loading. Bleischwitz *et al.* [29, 158, 159] conducted a series of studies using both flow and force measurements for a flat plate of AR = 2 at $0.01 \leq l/c \leq 2$, $0° \leq \alpha \leq 40°$, and $\mathrm{Re}_c = 56\,000$. As the studies were focused on flier applications, the ground plane moved at the freestream air speed. They observed an increase in lift and drag coefficients with decreasing gap ratio, in opposition to the aforementioned results of Refs. [15, 18, 28] for $\alpha < 0°$. Notably, aerodynamic loading on an airfoil in ground effect has been shown to differ between static and moving ground configurations due to ram effect [154, 160]. However, the aforementioned disagreement in the aerodynamic loading with decreasing gap ratio is likely due to the variation in $\beta$, which modulates the effect of the ground proximity on the suction side flow development, critical for high load generation on low AR plates.

In comparison to aforementioned steady state effects of ground proximity, ground effect aerodynamics of finite-span inclined flat plates under transient conditions, termed dynamic ground effect, have not yet been considered to the knowledge of the author. Dynamic ground effect may occur due to change in incoming flow conditions or a change in the gap ratio. Previous investigations into dynamic ground effect have considered airfoils pitching and surging near a ground surface, or a transient change in ground height to gain a improved understanding of aerodynamics of airplane takeoff and landing [161, 162]. In contrast, solar panels are fixed in terms

of their geometry and changes in orientation for maximizing solar irradiance are conducted at timescale significantly longer than prominent flow timescales. However, placement of photovoltaic installations in open environments, desirable for unimpeded power generation, exposes them to sudden changes in wind speeds and directions during extreme weather events. Such events are expected to cause notable modifications to aerodynamic loads, based on aforementioned steady state investigations, and remains to be addressed.

# Chapter 3

# Methodology

*Information about the experimental facilities and models are outlined in this chapter, along with an overview of the techniques used for direct load measurements and flow diagnostics. The chapter concludes with a description of the framework used for uncertainty quantification.*

## 3.1 Experimental Setup

Three experimental campaigns were carried out at the University of Waterloo (UW) in the Fluid Mechanics Research Laboratory (FMRL). All campaigns were carried out in the recirculating wind tunnel facility, using a boundary layer plate and solar panel models that are described in this section.

### 3.1.1 Recirculating Wind Tunnel

The recirculating wind tunnel facility shown in Fig. 3.1 was used for all experiments. Airflow was generated using a vane axial six blade fan belt-driven by an AC motor and controlled using a variable frequency drive. The flow was conditioned within the settling chamber using a series of five wire mesh screens, placed downstream of a honeycomb grid. A contraction of 9:1 area ratio was used to accelerate and homogenize the flow before entering the test section. The freestream velocity was set based on a calibration of the pressure drop across the contraction to the freestream velocity at the model location without the model. The test section has a length of 2.4 m and a square cross-section with side lengths of 0.61 m. All walls of the test section are 9.35 mm clear glass to allow free optical access to the test section. Cross-flow freestream uniformity of the empty test section was within ±0.5% over 95% of the cross-sectional area [163]. The turbulence intensity was less than 0.08% for all tests [164]. Furthermore, no significant spectral content was observed in the incoming flow near frequencies associated with inclined flat plates for selected experimental conditions.

The closed loop tunnel is capable of producing freestream velocities up to $U_\infty = 32\,\mathrm{m\,s^{-1}}$, which limits the operating Reynolds numbers to about $O(10^5)$ for the chosen chord lengths, well below operational Reynolds numbers of solar panels, ranging between $O(10^6)$ and $O(10^7)$

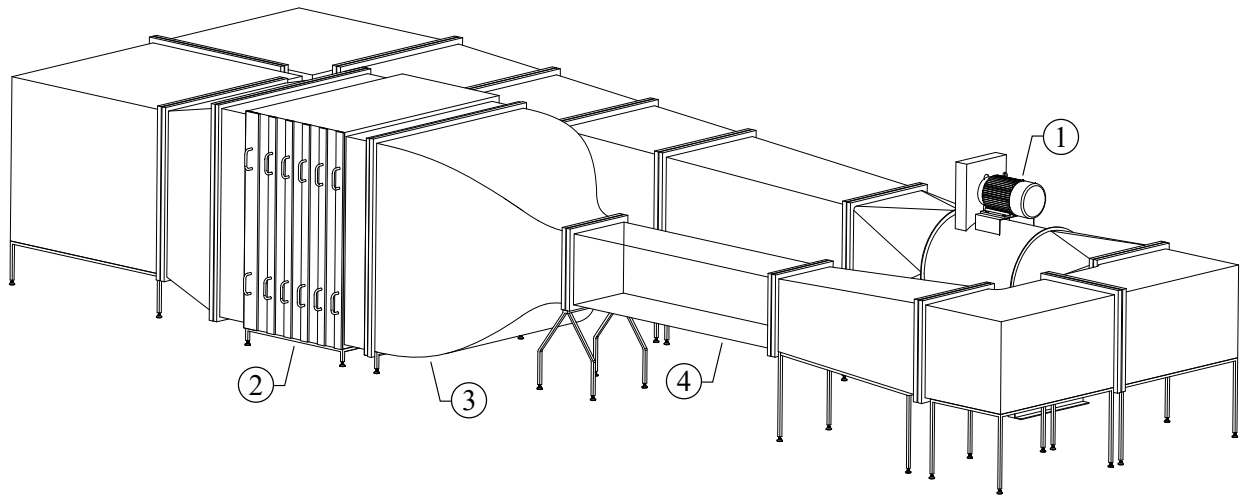


**Figure 3.1:** Recirculating wind tunnel facility at the Fluid Mechanics Research Laboratory (adapted from [165]). ① Fan and motor, ② settling chamber with honeycomb and mesh screens, ③ contraction, and ④ test section.

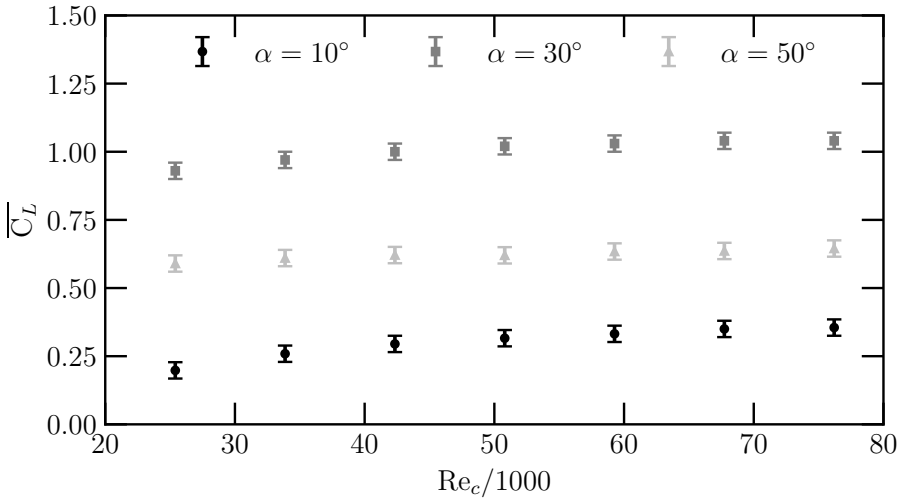


**Figure 3.2:** Time-averaged lift coefficient variation with respect to $\mathrm{Re}_c$ in free flight for AR = 1 at $\alpha$ = 10°, 30°, and 50°. Direct force measurements were collected using set up shown in Fig. 4.1a.

[116]. For $\alpha > 0°$, the force and moment coefficients were expected to be Reynolds number independent for $\mathrm{Re}_c > 10\,000$ according to previous investigations [124, 166]. Figure 3.2 presents lift coefficients of a AR = 1 plate at $\alpha$ = 10°, 30°, and 50° covering pre-stall, stall, and post-stall cases. Direct force measurements were collected using the same setup described in Chapter 4 (Fig. 4.1a). Based on these results, an operating Reynolds number of 50 000 was chosen for the present investigation. As additional confirmation, aerodynamic loads collected within the closed loop wind tunnel facility were found to generally agree with results found in literature, as shown throughout Chapters 4–6.

### 3.1.2 Boundary Layer Plate and Solar Panel Model

For all experiments, the generation of a nearly uniform incoming velocity profile, along with mounting of the solar panel model and load measurement devices were facilitated by a boundary layer plate. A schematic of the boundary layer plate is shown in Fig. 3.3. The boundary layer plate consists of a leading-edge (nose) section, a flat middle section, and a trailing edge flap. An asymmetric super-ellipse leading edge profile was used to promote smooth, attached flow over the length of the plate, while minimizing disturbance due to curvature [167]. The middle section was used for mounting the solar panel model with actuation and load measurement devices placed on the underside of the plate. A circular opening allowed for model stings (cylindrical slender beams) to be connected to these devices. For all experiments, the flap was placed at 15°, which was verified to produce an attached flow over the leading edge using smoke flow visualization. The total length of the boundary layer plate is approximately 1.8 m at this flap angle. The boundary layer plate was supported by three aluminium pillars with airfoil profiles to minimize blockage.

Solar panel models were created from 3.18 mm thick clear glass or acrylic. Glass provided minimal illumination power loss for cases where the flow between the model and ground was optically measured. For all other cases, acrylic was used due to its greater toughness compared

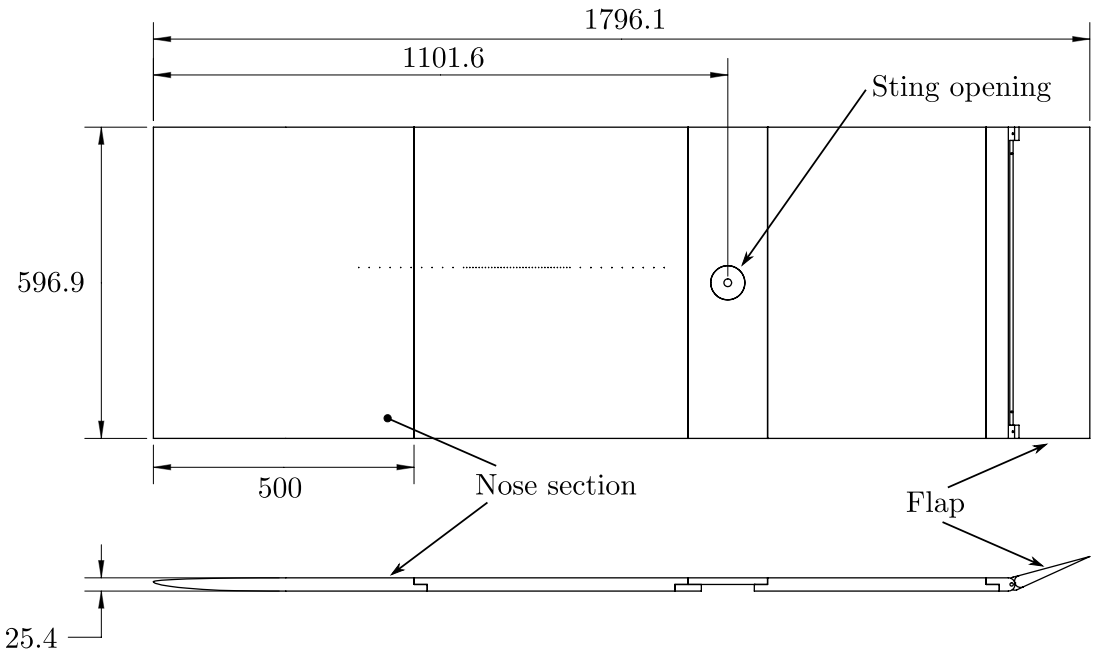


**Figure 3.3:** Boundary layer plate used for experiments.

to glass. Two aspect ratios were considered, AR = 1 and 2, spanning the low and high AR aerodynamic regimes (Section 2.3.2). Models with a chord length of 100 mm were used for all tests at AR = 1. In order to maintain the same blockage ratio, all tests at AR = 2 were conducted with models of chord length 71 mm, and the freestream velocity was adjusted to maintain the same Reynolds number between AR = 1 and 2 cases. The flat plate models were mounted to stings connected to load measurement devices that were shielded from the flow, with different sting-model configurations considered depending on the load and flow measurement requirements.

Placement of the model in the test section results in increased solid blockage, which may cause significant loading coefficient deviations relative to freestream conditions. This was mitigated using a solid blockage correction factor, applied to the freestream dynamic pressure used to normalize the forces and moments. The correction factor is based on Cowdrey's rederivation [168] of Maskell's blockage correction formulation [169], requiring only model geometry information. The uncorrected and corrected freestream dynamic pressures, $q_u$ and $q_c$, respectively, are related by

$$\frac{q_c}{q_u} = 1 + m' \left( \frac{A_m}{A_{ts}} \right), \tag{3.1}$$

where $m'$ blockage factor based on the model aspect ratio

$$m' = 1.85 + 1.35 e^{-0.05\mathrm{AR}}, \tag{3.2}$$

$A_m$ is the streamwise projected area of the model, and $A_{ts}$ is the cross sectional area of the test section. This correction was found to appropriately scale the loading measurements based on comparison to results from relevant literature.

## 3.2 Experimental Techniques

For all investigations, direct force measurements facilitated by a force balance were used to determine structural loading on the solar panel model. The design and characterization processes related to the force balances are provided in Section 3.2.1. Surface oil flow visualization was used for qualitative flow diagnosis, while nearly all quantitative flow results were extracted from planar particle image velocimetry measurements. Therefore, brief introductions to these techniques are provided and practical considerations followed during implementation are outlined herein. Specific experimental setup descriptions are found in Chapters 4–6.

### 3.2.1 Direct Load Measurements

Force balances provide a direct and a convenient method of obtaining structural loads and was used in this investigation for all load measurements. The loading results presented in Chapter 4 were obtained using an in-house fabricated, two-component force balance as shown in Fig. 3.4. The in-situ mounting of the force balance underneath the boundary layer plate is shown in Fig. 4.1a. High structural strength and stiffness, with natural frequencies significantly higher than relevant flow frequencies were desirable. High sensitivity of the balance was also needed, which directly conflicts with the high stiffness requirement. Additionally, a compact design was beneficial to minimize blockage of the test section. Cantilever beam profiles typically used as basic sensing elements in traditional strain gauge balances [e.g., 170] suffer from low stiffness when made thin enough for high sensitivity. To address this, a sensing element as seen in Fig. 3.4b, referred to as a binocular sensing element [171], was adopted. The dual beam structure of a binocular element provides high stiffness, while the high stress concentration at the thinnest sections facilitates strain gauge measurements with high sensitivity and accuracy.

Prior to fabrication, a structural simulation was used to verify that the natural frequencies were at least an order of magnitude higher than the relevant flow frequencies and the strain at the thinnest

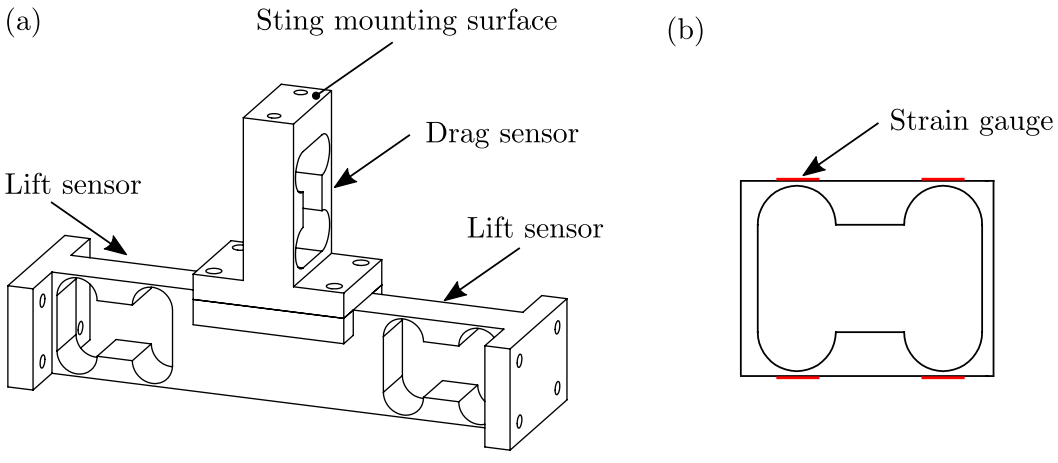


**Figure 3.4:** Force balance used for force measurements in Chapter 4. (a) Assembled balance and (b) binocular sensing element showing placement of strain gauges indicated in red.

locations would not exceed the capabilities of the selected aluminium strain gauges. The balance was fabricated using a 6061-T6 aluminium alloy to match the strain gauge material, mitigating thermal expansion effects. The balance was composed of two components, with two sensing elements on the longest beam and one element on the short vertical beam (Fig. 3.4a), which were used to measure forces in two orthogonal directions, namely lift and drag. Only one of the long member sensors was used to measure the lift force, while the other was used for troubleshooting and validation purposes. This balance design also allows for roll moment measurements using both the lift sensors, however, this capability was not utilized. For each sensing element, four strain gauges were affixed at the thinnest points in a Wheatstone bridge configuration to maximize the electrical signal strength and automatically compensate for temperature and lead wire effects. The electrical signals from each sensing element were externally amplified using FUTEK CSG110 strain gauge signal conditioners prior to being measured.

The two sensing elements were calibrated individually using weights in still air outside of the test section. The balance was rotated and weights mounted to allow for gravity to apply a known force to each sensing element. The calibration was verified to be linear and the cross-talk between each sensor was less than 1% of the applied load during calibration. The comparison of results presented in Chapter 4 to values in literature served as validation of the balance.

For force measurements pertaining to results presented in Chapters 5 and 6, a JR3-30E12A4 commercially available load cell was utilized. The load cell was mounted underneath the boundary layer plate as shown in Figs. 5.1 and 6.1. The JR3 load cell is able to measure all six loading components, has relatively high overload characteristics, and is able to tolerate mild shock loading during model actuation for simulating sudden wind direction variations. A six-way factory calibration also allows for combined loads to be applied and individual loading components to be resolved. The factory calibration was verified in-situ under quiescent conditions using precision weights and resultant errors were incorporated into aerodynamic coefficient uncertainties.

### 3.2.2 Surface Oil Flow Visualization

Limitations associated with quantitative flow measurements can be overcome with flow visualization techniques, which in general tend to be simpler and require less experimental efforts. A wide variety of flow visualization techniques have been developed, and the reader is directed to [172, 173] for a comprehensive overview of these techniques. With currently available flow visualization techniques, decryption of flow patterns within the flow and also wetted surfaces is possible in wind tunnels to produce both qualitative and semi-quantitative results.

Surface oil flow visualization was employed to determine the flow topology over the suction side surface for the results presented in Chapter 5. The oil mixture used for surface flow visualization was made using mineral oil, diesel fuel, and fluorescent dye. The mineral oil applied as a thin layer was found to respond appropriately to the wall stresses on airfoils at FMRL [174] and was also used in these tests. The fluorescent dye provided a way to track the motion of the oil on the surface and the diesel fuel was used as an activator of the fluorescent dye. A volumetric ratio of 3:1:1 of mineral oil, diesel, and dye was found to be optimal in terms of ease of application and provided a sufficiently high signal-to-noise ratio in the captured images. The mixture was applied

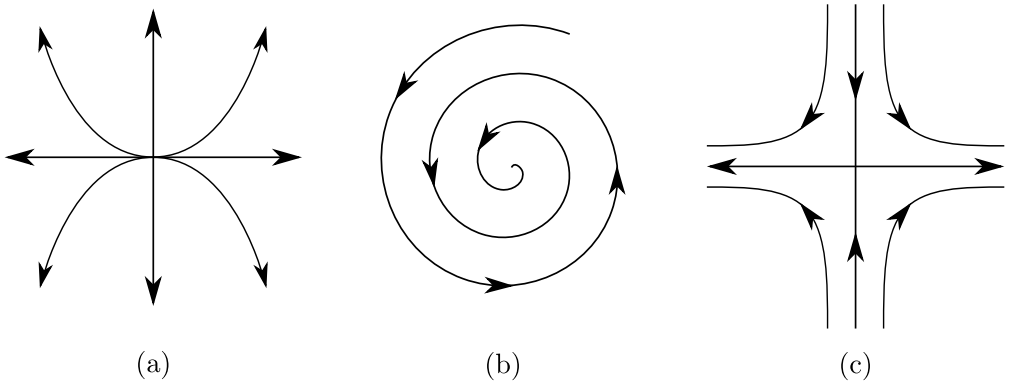


**Figure 3.5:** Critical points relevant to interpretation of flow patterns: (a) repelling node, (b) attracting focus, and (c) saddle. Nodes and foci may also have opposing flow directions to those shown.

using a foam brush with strokes aligned in the chordwise direction, which was found to improve the oil response to the flow compared to other application patterns.

The surface flow visualization images were analyzed within the framework of critical point theory [175–177]. Critical points are marked locations within three dimensional separated flows where streamlines may originate or terminate. Streamline patterns of these points may be categorized into three types as shown in Fig. 3.5: nodes, foci, or saddles. Notably, other types of nodes and foci theoretically exist, (e.g., isotropic nodes, or centres), however, these are unlikely to be observed experimentally for separated flows. Furthermore, a combination of these critical points is possible in three-dimensional flows and mark instances of separation, reattachment or interaction between shear layers of separate initiation points.

### 3.2.3 Particle Image Velocimetry

Particle image velocimetry (PIV) was the main flow measurement technique employed in this work. The ability to acquire instantaneous velocity field information non-intrusively using PIV is highly desirable. Generally, PIV involves imaging of neutrally buoyant tracer particles illuminated by a pulsed light source to obtain velocity vector fields through statistical image processing methods. Detailed workings of PIV and useful experimental guidelines are available in Westerweel *et al.* [178] and Raffel *et al.* [179]. Two- and three-component PIV configurations were used in this thesis for midspan and crossplane flow measurements, respectively. While specific PIV setup details can be found in relevant chapters, commonalities during implementation are provided herein.

To accurately reflect flow velocities, tracer particles that follow the flow without altering the natural flow or exhibiting significant inertial effects are desirable. Additionally, the particles should also scatter light sufficiently to be imaged. In this work, a water-glycol mixture was used to produce tracer particles through vaporisation with a mean diameter of 1 µm, which results in a characteristic response frequency on the order of $O(10)$ kHz [180], well above the Nyquist limit of PIV acquisitions ($O(1)$ kHz) used in all investigations of this work. The seeding was

first collected in a plenum and introduced into the wind tunnel at the end of the test section, with sufficient time given before image acquisition to allow for a uniformly seeded flow to develop. Since the wind tunnel is not fully sealed, the level of seeding within the wind tunnel decreases over time, however, the resident time was long enough to allow acquisitions of up to two minutes.

The illumination of the fog particles was facilitated by the means of a DM20-527 Nd:YAG dual pulsed laser. In double pulse mode, the image acquisition rate is decoupled from the pulse separation time by using a two rapid pulses, with each pair of pulses repeated at the acquisition frequency, allowing for finer control when optimizing PIV acquisitions. Furthermore, dual pulse operation allows for high speed (Chapter 6) and low speed acquisition (Chapters 4 and 5) with the same system, while maintaining optimal particle displacements. In all PIV experiments in this work, pulse separation times were tuned such that particle motions were linear and around 10 px for each image pair in order to accurately resolve particle motions.

For PIV measurements, the laser light was formed into a thin sheet, using a combination of spherical and cylindrical lenses, and turning mirrors. An example of such an optical arrangement and resulting laser sheet is shown in Fig. 3.6. In two-component PIV, the cameras were oriented normal the light sheet, while for three-component PIV, two cameras were angled away from the normal such that the combined optical angle of the cameras axis is set close to 90° to minimize uncertainties in all three velocity components [181]. A calibration target placed parallel to the laser sheet relates the image space to the physical space for both PIV configurations. For two-component PIV measurements, a square grid with 10 mm spacing was used and a simple scaling calibration was applied. For three-component PIV measurements, an off the shelf two-level calibration target was used. This is necessary for camera calibration of a three-component PIV setup, as noncoplanar points are needed to estimate camera viewing angles, essential for three-component velocity vector reconstruction. When the camera was placed at an angle to the measurement plane, alignment of the camera focus plane was facilitated through the use of special tilting lens adaptors, known as Scheimpflug adaptors (after Theodor Scheimpflug[1]). For three-component PIV, misalignment between the light sheet and focus plane were further corrected using self-calibration methods based on the disparity between simultaneous particle

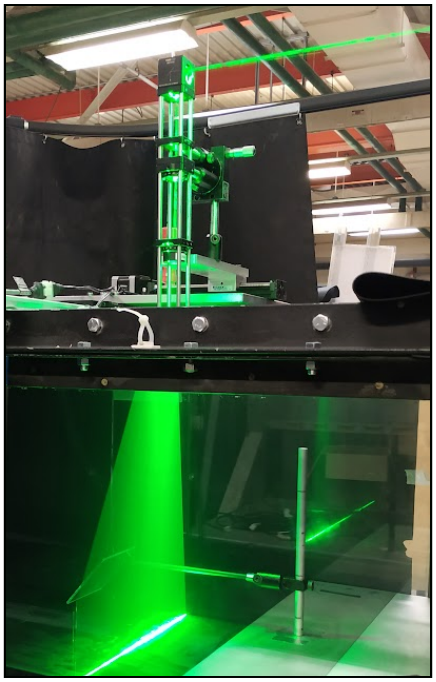

**Figure 3.6:** Formation of a laser sheet using a set of turning mirrors and lenses. The spread of the laser sheet has been exaggerated for better visualization.

[1]Theodor Scheimpflug himself disclaimed inventing the principle and attributed it to the original patent owner Jules Carpentier, a French photographic engineer.

images from both cameras [182]. For self-calibration, lower seeding densities relative to normal acquisitions were used such that both cameras can accurately resolve the same tracer particles without interference.

Prior to vector field calculation, particle images were pre-processed to improve the local signal-to-noise ratio, and thus the final vector field quality. Initially, the minimum count of the full time series of data was subtracted from individual images at each pixel, i.e., background subtraction. In some cases, image artifacts due to vibration of the model persisted after background subtraction. For these cases, a temporal high pass filter is applied [183] as the undesired reflections have frequencies lower than the passage of illuminated particles. Effects of light intensity variation within each image on the final vector field is minimized through normalization of each particle image by a normalized ensemble average of each data set. An iterative statistical cross-correlation method [184] was applied to pre-processed image pairs to obtain a time-series of velocity field. For stereo measurements, the images were first dewarped based on the camera calibration prior to computing vector fields. During vector processing, universal outlier detection [185] was used to detect and replace erroneous vectors. PIV uncertainties were calculated using correlation statistics method, which incorporates uncertainties from particle disparity, camera noise, and out-of-plane particle motions [186, 187].

## 3.3 Vortex Characterization

Once velocity vector fields are obtained using PIV, further analysis is needed to quantify salient flow features. Much of the analysis of this work focuses on tip vortices that develop downstream of the flat plate model. Thus, computational steps most relevant to quantification of vortex dynamics are presented in the following sections.

### 3.3.1 Vorticity and Circulation

Vorticity describes the degree of local rotation of an infinitesimal fluid element. Mathematically, vorticity is the curl of the velocity field, $\vec{u}$,

$$\vec{\omega} = \nabla \times \vec{u}. \tag{3.3}$$

Computation of vorticity from velocity vector field results from PIV requires some additional considerations. Although it is possible to directly apply the above definition to compute vorticity, gradients of PIV velocity results contain amplified noise due to its discrete nature and uncertainties related to cross-correlation used to estimate velocities. Vorticity field estimations are improved by computing 8-point weighted local line integrals of velocity at each vector position (i.e., local circulation) within the initialized vorticity field [179].

Circulation, a scalar integral quantity, is the global rotation for a finite area of the fluid. It may either be computed directly from the integral of tangential velocity along a closed contour, $C$, or

from the area integral of vorticity contained within an area $A$ as follows:

$$\Gamma = \oint_C \vec{u} \cdot d\vec{s} = \iint_A \vec{\omega}\, dA. \tag{3.4}$$

In the case of experimentally obtained velocity fields, circulation estimates computed using the line integral form is preferred, as introduction of additional noise from the computation of discrete gradients when using the vorticity fields can be avoided.

### 3.3.2 Vortex Identification

Although aerodynamicists may astutely identify coherent structures from velocity or vorticity fields, mathematical definitions are needed for quantification of vortex dynamics. Vortices in the flow field can be characterized based on their associated circulation (strength) and position, however, they must first be identified. Vortex identification has received significant attention over last several decades [188], however, a universal vortex identification criterion has yet to be developed. For the purposes of the current work, the main goal was to employ a methodology that would reliably and accurately identify and characterize dominant coherent structures within the flow field.

For this purpose, the $\lambda_2$ criterion, formulated by Jeong & Hussain [189], is employed to identify and characterize vortices. Although there are number of similar velocity gradient based vortex identification methods with different formulations, they are practically equivalent when using experimental data [188, 190, 191]. Using PIV velocity fields, the eigenvalues of $\Omega^2 + S^2$ are computed at each point in the measurement domain, where $\Omega$ is the angular rotation tensor and $S$ the strain rate tensor. Eigenvalues of $\Omega^2 + S^2$, $\lambda_i$, are then ordered based on their magnitudes. Vortices are identified as closed isocontours of negative $\lambda_2$, the second largest eigenvalue of $\Omega^2 + S^2$, using a selected threshold that is less than zero. Circulation is estimated based on a line integral formulation (Eq. 3.4) along the selected $\lambda_2$ isocontour. To minimize errors due to choice of the $\lambda_2$ threshold, a convergence study of circulation is conducted for a range of $\lambda_2$ threshold values. A convergence criteria of 3% is used to determine the lowest possible $\lambda_2$ threshold.

The inherent noise in experimental measurements along with discretized nature of PIV results may lead to relatively high uncertainties in vortex core tracking when using derivative-based techniques. To circumvent this, a relatively simple integral quantity technique postulated by Graftieaux *et al.* [192], known as the $\Gamma_1$ method, can be used to identify vortex core positions. If $P$ is a point on a discrete velocity field, a vector can be defined to any point $M$ on this field as $\overrightarrow{PM}$. If $P$ is at a vortex core, then the angle between $\overrightarrow{PM}$ and the velocity vector at $M$ should be 90° (for an ideal vortex), otherwise, the angle will be less than 90°. On this basis, the $\Gamma_1$ field for a given velocity field domain is constructed as the average sine of the angle between the vector $\overrightarrow{PM}$ and the local velocity at $M$, $\vec{V}_M$. Near a vortex core, a local peak between 0.9 to 1 in $|\Gamma_1|$ is expected [192] and can be readily identified using local peak detection.

## 3.4 Uncertainty Estimation

Uncertainty quantification due to both systematic and random errors is critical for accurate interpretation of experimental results. In this work, experimental uncertainty is mainly related to estimation of aerodynamic loading coefficients from direct load measurements, and velocity fields from PIV measurements.

Uncertainties presented throughout this thesis are calculated using the $n^{\text{th}}$ order uncertainty methodology of Moffat [193] over a 95% confidence interval. In this method, the uncertainty of a a parameter of interest, $X$, is estimated as:

$$\epsilon_X = \sqrt{\sum_{i=1}^{N} \epsilon_i^2}, \tag{3.5}$$

where $\epsilon_X$ is the total uncertainty and $\epsilon_i$ is that due to a given $i^{\text{th}}$ source of error, with a total of $N$ sources. Uncertainty may arise from zero order errors (e.g., measurement resolution), first order errors (e.g., temporal fluctuations), and $n^{\text{th}}$ order errors (e.g., instrument calibration). Practically, it is impossible to account for all sources of error, however, the most significant sources are accounted such that clear interpretations may be made from experimental results.

Inevitably, directly measured parameters are used to calculate derived quantities, such as in estimation of loading coefficients from direct force or moment measurements. Uncertainty in measured quantities are propagated to derived quantities where necessary using one of two methods. When the relationship between a measured quantity, $X_{m,i}$, and a derived quantity, $X_d$ can be functionally defined, i.e., $X_d = f(X_{m,1}, X_{m,2}, \ldots, X_{m,n-1}, X_{m,n})$, then the uncertainty of $X_d$ is estimated as

$$\epsilon_{X_d} = \sqrt{\left(\frac{\partial f}{\partial X_{m,1}}\epsilon_{X_{m,1}}\right)^2 + \left(\frac{\partial f}{\partial X_{m,2}}\epsilon_{X_{m,2}}\right)^2 + \cdots + \left(\frac{\partial f}{\partial X_{m,n-1}}\epsilon_{X_{m,n-1}}\right)^2 + \left(\frac{\partial f}{\partial X_{m,n}}\epsilon_{X_{m,n}}\right)^2}. \tag{3.6}$$

As long as the evaluation of the partial derivatives, known as sensitivity coefficients, is simple, then the above equation may be used for uncertainty estimation. In most cases, either the sensitivity coefficients are tedious to compute or the processing steps are highly complex and sensitivity coefficients are nearly impossible to obtain (e.g., Eq. 3.4). For these cases, total uncertainty of $X_d$ is computed based on the method of sequential perturbation [194]. Although the exact implementation will vary based on the analysis technique, the general procedure for the method of sequential perturbation is as follows:

1. Calculate $X_d$ using nominal values of $X_{m,i}$ using the known relationship.
2. Positively perturb the $i^{\text{th}}$ $X_{m,i}$ by its uncertainty and compute $X_{d,i}^{+}$.
3. Negatively perturb the $i^{\text{th}}$ $X_{m,i}$ by its uncertainty and compute $X_{d,i}^{-}$.
4. Estimate the uncertainty of $X_d$ due to $X_{m,i}$ as $|X_{d,i}^{+} - X_{d,i}^{-}|$.

**Table 3.1:** Maximum uncertainty estimates of measured and derived quantities. All uncertainty estimates are provided over a 95% confidence internal.

| Parameter | Chapter 4 | Chapter 5 | Chapter 6 | Method |
|---|---|---|---|---|
| $\mathrm{Re}_c$ | ±2000 (4% of set point) | | | Repeated trial variability |
| $\alpha$ | ±0.2° | | | Measurement resolution |
| $\beta$ | - | ±0.2° | | Measurement resolution |
| $l/c$ | ±1.0% | | ±5.0% | Eq. 3.6 |
| $\overline{C_L}$ | ±0.03 | ±0.04 | ±0.04 | Eq. 3.6 |
| $\overline{C_D}$ | ±0.03 | ±0.03 | - | Eq. 3.6 |
| $\overline{C_S}$ | - | ±0.03 | - | Eq. 3.6 |
| $\overline{C_T}$ | - | ±0.06 | - | Eq. 3.6 |
| $\overline{C_{B,R}}$ | - | ±0.03 | - | Eq. 3.6 |
| $\overline{C_{B,P}}$ | - | ±0.03 | - | Eq. 3.6 |
| $\overline{C_{B,Y}}$ | - | ±0.03 | - | Eq. 3.6 |
| $\overline{C_{B,T}}$ | - | ±0.05 | - | Eq. 3.6 |
| $\overline{\vec{U}}/U_\infty$ | < 0.026 | < 0.012 | < 0.007 | Correlation statistics method |
| $\overline{C_l}$ | ±0.06 | - | - | Method of sequential perturbation |
| $\overline{\Gamma_{TV}}/(cU_\infty)$ | ±0.04 | ±0.06 | ±0.06 | Method of sequential perturbation |
| $\overline{z_{TV}}/c$ | - | ±0.04 | ±0.04 | Method of sequential perturbation |
| $\overline{y_{TV}}/c$ | - | ±0.04 | ±0.04 | Method of sequential perturbation |
| $C_L$ | - | - | ±0.05 | Repeated trial variability |
| $\vec{U}/U_\infty$ | - | - | < 0.044 | Correlation statistics method |
| $\Gamma_{TV}/(cU_\infty)$ | - | - | ±0.1 | Method of sequential perturbation |
| $z_{TV}/c$ | - | - | ±0.04 | Method of sequential perturbation |
| $y_{TV}/c$ | - | - | ±0.04 | Method of sequential perturbation |

5. Use Eq. 3.5 to combine the uncertainties from all considered error sources of $X_{m,i}$, i.e., $\sqrt{\sum_{i=1}^{N}(X_{d,i}^{+} - X_{d,i})^{-}|^2}$.

Uncertainty estimates presented throughout this work are calculated based on the above framework and are summarized in Table 3.1. For conservative uncertainty estimation, the maximum uncertainty of a parameter is used throughout this work. They are also noted where relevant in Chapters 4–6.

# Chapter 4

# Effect of Angle of Attack, Aspect Ratio, and Ground Proximity on Finite-span Flat Plate Aerodynamics

*As the initial investigation into ground effect aerodynamics of finite-span flat plates, a relatively large set of parameters are considered in this chapter. Specifically, effects of angle of attack, aspect ratio, and ground proximity on the steady state aerodynamics of a finite-span inclined flat plate under both headwinds and tailwinds are investigated. The analysis of both structural loads and flow development is used to identify the salient features of flows over flat plates in close ground proximity. The results show that ground effect is significant below 0.5 chord lengths from the ground, most notably near the stall angle, where it leads to significant changes in flow development. The nature of aerodynamic modifications related to ground effect are strongly dependent on the aspect ratio, angle of attack, and wind direction combinations.*

Parts of this chapter have been adapted from

Pieris, S., Yarusevych, S., & Peterson, S. D. 2022 Flow development over inclined flat plates in ground effect and relation to aerodynamic loads. *Phys. Fluids* **34** (9), 095113. DOI.

## 4.1 Introduction

As discussed in Section 2.3, studies on finite-span inclined flat plates in free flight have explored the influence of several parameters on the flow and forces, including $\alpha$ and AR. Flight-related studies tend to restrict angle of attack to relatively low values, however, since optimal solar irradiance angles vary based on the latitude [117], exploration of the full range of angles of attack is important [47]. Lift coefficient reaches a maximum in the range of $10° \leq \alpha \leq 45°$ [18, 19], marking a critical lift configuration for photovoltaic installations. The exact stall angle is dependent on aspect ratio, with a square plate attaining maximum lift between $30° \leq \alpha \leq 35°$ [18, 19, 111, 116]. The aspect ratio has a significant effect on the aerodynamic loading of finite-span inclined plates in free flight due to the influence of tip effects [15, 18–22, 157, 159, 195, 196]. The tip vortices induce significant downwash over plates of AR $\leq 1$, facilitating delayed stall and high aerodynamics loads through leading-edge shear layer reattachment [19, 23]. As the aspect ratio is increased above two, the range of influence of the tip vortices diminish, resulting in lower stall angles and decreased aerodynamic performance.

As discussed in Section 2.4, flat plates situated near a ground plane can experience significantly different steady state aerodynamic loading in comparison with plates in free flight conditions. Most importantly, previous studies show a notable difference in ground proximity effect on loading for $\alpha > 0$ and $\alpha < 0$ [15, 18, 28, 29, 158, 159]. Near positive stall angles, the ram effect leads to higher than free flight loading [154]. Close to negative stall angles, the recirculation region bordering the back of the plate was repositioned further downstream as the gap ratio decreased, resulting in a decrease in the pressure difference between the suction and pressure sides. Consequently, the mean lift and drag coefficients decreased with decreasing gap ratio. Notably, parameter ranges of $\alpha$ and AR covered in previous investigations were limited, hindering the understanding of other physical mechanisms related to ground proximity and obfuscated $\alpha$ and AR effects on flat plate aerodynamics in close ground proximity.

There is a notable effect of ground proximity on flow development and aerodynamic loading for finite-span flat plates with substantial differences in forcing for varying plate orientations, aspect ratios, and gap ratios. However, the combined effect of these parameters has not been considered in detail, which forms the motivation for the investigation presented in this chapter. The specific focus is on the combined influence of angle of attack, plate orientation, and ground proximity for aspect ratios at the "low" and "high" limits (AR = 1 and 2), which are expected to represent notably different end effect conditions. This is accomplished through a series of experimental studies combining force and flow field measurements, thereby elucidating the coupled effect of key geometric parameters on aerodynamic loading and the underlying flow physics.

## 4.2 Experiment Details

Herein, the flow development around, and the resulting aerodynamic loading on, inclined flat plates with AR = 1 and 2 is explored for the full range of angles of attack ($-90° \leq \alpha \leq 90°$) and gap ratios within the range $0.1 \leq l/c \leq 1$. The experimental set up is shown in Fig. 4.1a. A Cartesian coordinate system with origin at the geometric centre of the plate is defined such that

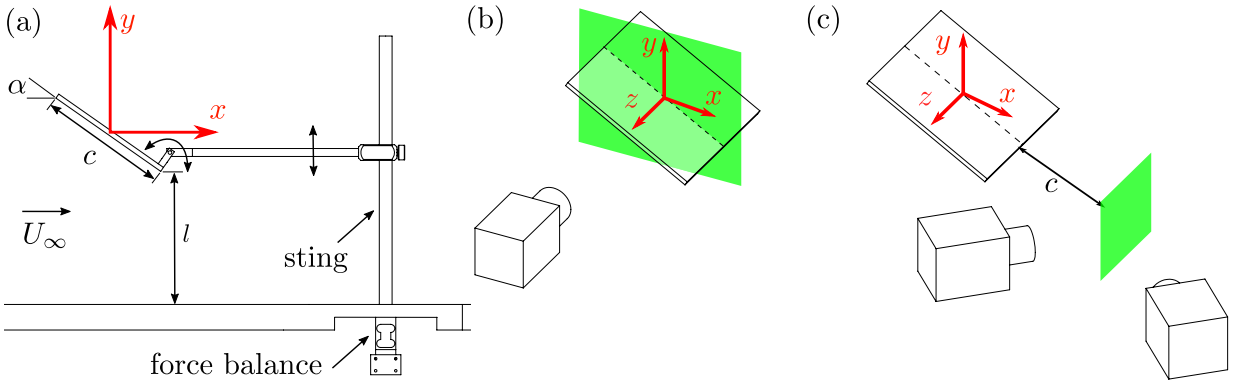


**Figure 4.1:** Schematic of the experimental setup. (a) Sting and force balance. Field of view and camera arrangement for (b) streamwise midplane flow measurements, and (c) cross-plane flow measurements one chord length downstream of the trailing edge.

the freestream flow is in the $x$ direction, and the $y$ direction is oriented normal to the ground plane. The model was placed at a distance $l$ away from the ground surface at an angle $\alpha$ with respect to the $x$ axis. The flat plate models were made of 3.18 mm thick clear glass. The chord lengths of the AR = 1 and AR = 2 models were 100 mm and 71 mm, respectively. These chord lengths were selected such that the blockage ratios were equivalent between the two models at a given angle of attack. The maximum compound blockage was approximately 5% at $\alpha = 90°$. A solid blockage correction was applied to the reported force coefficients [197]. The models were mounted on a sting assembly as shown in Fig. 4.1a, which allowed adjustment of both $l$ and $\alpha$ to within ±0.5 mm and ±0.2°, respectively. A horizontal sting configuration is used to minimize the disturbance to the suction side flow. The mean lift and drag coefficients were verified to be Reynolds numbers independent for $\mathrm{Re}_c \geq 35\,000$, and the Reynolds number was maintained at 50 000 for all cases.

All experiments were carried out in the recirculating wind tunnel in the Fluid Mechanics Research Laboratory at the University of Waterloo. The glass test section of the tunnel has a length of 2.4 m and a square cross section with side length 0.6 m. The tunnel contraction ratio is 9:1 with a honeycomb insert and a set of five screens installed upstream to condition the flow, resulting in a turbulence intensity of less than 0.1%. The empty test section freestream uniformity was within ±0.5% over 95% of the test section span. The freestream velocity, $U_\infty$, was set based on the contraction pressure drop, which was calibrated against a Pitot-static tube placed in the center of the empty test section inlet, with an uncertainty of less than 3%.

Experiments were conducted for both positive and negative incidence angles and gap ratios as specified in Table 4.1. Forces were measured for the full range of angles, while flow field measurements were limited to $\alpha = \pm 10°$, ±30°, and ±50° for AR = 1 and $\alpha = \pm 30°$ for AR = 2. The selected angles for flow measurements span pre-stall, stall, and deep stall cases, thus covering a significant portion of global photovoltaic installations based on latitudes corresponding to photovoltaic plate angles used for maximizing solar irradiance [32]. Tested gap ratios span the moderate ground effect to free flight regimes[29]. Flow field measurements were obtained at $l/c = 0.1$, 0.2, 0.5, and 1 for both models.

**Table 4.1:** Test matrix of measurements

| Parameter | Forces | PIV | |
|---|---|---|---|
| AR | 1, 2 | 1 | 2 |
| $\alpha$ [°] | ±0, 10, 20, 25, 30, 35, 40, 50, 60, 70, 80, 90 | ±10, 30, 50 | ±30 |
| $l/c$ | 0.1, 0.2, 0.3, 0.5, 0.75, 1 | 0.1, 0.2, 0.5, 1 | |

A two-component force balance mounted beneath the ground plane was used to measure lift and drag force components (Fig. 4.1a). The balance employed high stiffness binocular sensor elements [171] as shown in Fig. 3.4b, with each sensing element consisting of four strain gauges in a full Wheatstone bridge configuration. The strain gauge signal was amplified using FUTEK CSG110 amplifiers. The force balance was calibrated using precision weights in still air. Maximum crosstalk between the two force components was less than 1% of the applied load. For each force measurement, 30 000 samples were collected at 1000 Hz, which were ensemble averaged to computed mean lift and drag. Contribution to the measured loads from the sting were quantified and corrected for by repeating all force measurements with the model decoupled from the sting assembly by virtue of an alternative model mounting structure. The mean force components measured in this configuration were subtracted from the test case measurements to isolate the aerodynamic loads on the flat plate from the sting assembly. Force coefficients are defined as $C_F = 2F/(q_c \mathrm{AR} c^2)$, where $F$ is the measured force component and $q_c$ is the blockage corrected freestream dynamic pressure. The maximum uncertainty in the reported force coefficients is estimated to be ±0.03.

Planar two and three-component PIV were used to measure velocity fields in two configurations as shown in Figs. 4.1b and 4.1c. Two-component PIV at the plate midspan captured the streamwise flow development over the plate (Fig. 4.1b), whereas the cross-plane flow was measured using Stereoscopic PIV (SPIV) to capture the tip vortex behaviour (Fig. 4.1c). To minimize the effect of the sting on the flow measurements, the sting was offset along the spanwise direction by $0.2c$ from the midspan position based on preliminary velocity measurements. Additionally, cross-plane flow measurements were also collected near the tip farthest away from the sting. The flow was seeded using a glycol-water fog mixture with a mean particle diameter of approximately 1 µm. The particles were illuminated using a Photonics DM20-527 Nd:YLF single cavity dual pulsed laser, which was conditioned into a laser sheet outside the test section. Particle images were acquired in double frame mode at 15 Hz, and 1000 image pairs were collected for each case investigated, which was found to be sufficient for convergence of mean velocity field statistics. An overview of the PIV parameters for both configurations is provided in Table 4.2.

Particle images at the plate midspan were captured using a single 5.5 Mpx LaVision Imager sCMOS camera with a sensor size of 2560 by 2160 px. The camera was outfitted with a Nikon UV-Nikkor lens with a focal length of 105 mm set to an aperture number $f_\# = 5.6$. The full sensor was used to capture a field of view (FOV) of approximately 115 mm by 98.9 mm with a magnification factor of 0.14, corresponding to FOVs of $1.15c \times 0.99c$ and $1.62c \times 1.39c$ for AR = 1 and 2, respectively. The camera was mounted on a precision traverse with a resolution

**Table 4.2:** PIV parameters

| Parameter | Midspan PIV | Normal SPIV | Zoomed out SPIV | Unit |
|---|---|---|---|---|
| Laser | | Photonics DM20-527 | | - |
| PIV Mode | | Double frame | | - |
| Camera(s) | | LaVision Imager sCMOS CLHS | | - |
| Sensor size | | $2560 \times 2160$ | | px × px |
| Lens focal length | 105 | 200 | 50 | mm |
| Numerical aperture | 5.6 | 5.6 | 8 | - |
| Magnification | 0.14 | 0.22 | 0.11 | - |
| Field of view | $117.0 \times 98.9$ | $90.8 \times 78.0$ | $183.0 \times 163.7$ | mm |
| AR = 1 | $1.17c \times 0.99c$ | $0.91c \times 0.78c$ | $1.83c \times 1.64c$ | - |
| AR = 2 | $1.62c \times 1.39c$ | $1.28c \times 1.10c$ | $2.58c \times 2.37c$ | - |
| Pulse separation | 70 (AR = 1)<br>50 (AR = 2) | 50 | 50 | µs |
| Final window size | | $24 \times 24$ (75% overlap) | | px |
| Vector pitch | 0.27 | 0.51 | 1.13 | mm |
| Combined optical angle | - | 90° | 90° | |
| Sample rate | | 15 | | Hz |
| Number of images | | 1000 | | - |

of 0.01 mm to allow for wall normal motion when adjusting the model gap ratio. The laser sheet thickness was 1 mm at full laser power. Double frame images were acquired with a frame separation between 50 µs to 70 µs resulting in average particle displacements of 12 px.

At a cross-plane one chord length downstream from the trailing edge SPIV was conducted. Two optical configurations were used, denoted normal and zoomed out. For the normal SPIV configuration, two 5.5 Mpx LaVision Imager sCMOS cameras were mounted to the same traverse system used for streamwise measurements. Each camera was outfitted with a Nikon 200 mm lens set to an aperture $f_\# = 5.6$ and a Scheimpflug adapter. The camera optical axes were oriented at 45° to the image plane. Particle images were captured in double-frame mode using the full sensor size, resulting in a total FOV of 90.8 mm by 78.0 mm ($0.91c \times 0.78c$ and $1.28c \times 1.10c$ for AR = 1 and 2, respectively) for the normal configuration. For the zoomed-out configuration, the cameras were equipped with Nikon 50 mm lenses set to an aperture $f_\# = 8$, allowing for an increase in FOV to 183 mm by 163.7 mm ($1.83c \times 1.64c$ and $2.58c \times 2.31c$ for AR = 1 and 2, respectively). The laser sheet thickness for both configurations was approximately 2 mm. The frame separation time was kept constant at 50 µs resulting in out-of-plane displacements of less than 14 px. The zoomed out FOV was used for AR = 1 at ±50° and for the entirety of the AR = 2 cases.

## 4.3 Time-averaged Lift and Drag Coefficients

Time-averaged lift (magnitudes) and drag coefficients representative of free flight ($l/c = 1$) are presented in Fig. 4.2. Included in the plots for comparison are results for a sharp-edged flat plate by Ortiz *et al.* [18] and round-edged flat plates by DeVoria & Mohseni [19] and Bleischwitz *et al.* [29]. At AR = 1, $|\overline{C_L}|$ increases with $|\alpha|$ up to a maximum around 1.05 at $|\alpha| = 30°$, then decreases back to zero at $|\alpha| = 90°$. For AR = 2, $|\overline{C_L}|$ reaches a maximum of 0.69 at $|\alpha| = 20°$, which is then followed by a plateau region from $20° \leq \alpha \leq 50°$.

For both aspect ratios, the drag tends to increase with angle of attack. As seen in Figs. 4.2b and 4.2d, the local slope changes around the angles of attack corresponding to maximum lift. This is more pronounced for AR = 1 (Fig. 4.2b), where the drag coefficient decreases between $\alpha = 35°$ and 40°. For $25° \leq |\alpha| \leq 50°$, $\overline{C_D}$ for the AR = 1 model is higher than that of the AR = 2 model, while outside this range the two aspect ratios are comparable to within experimental uncertainty.

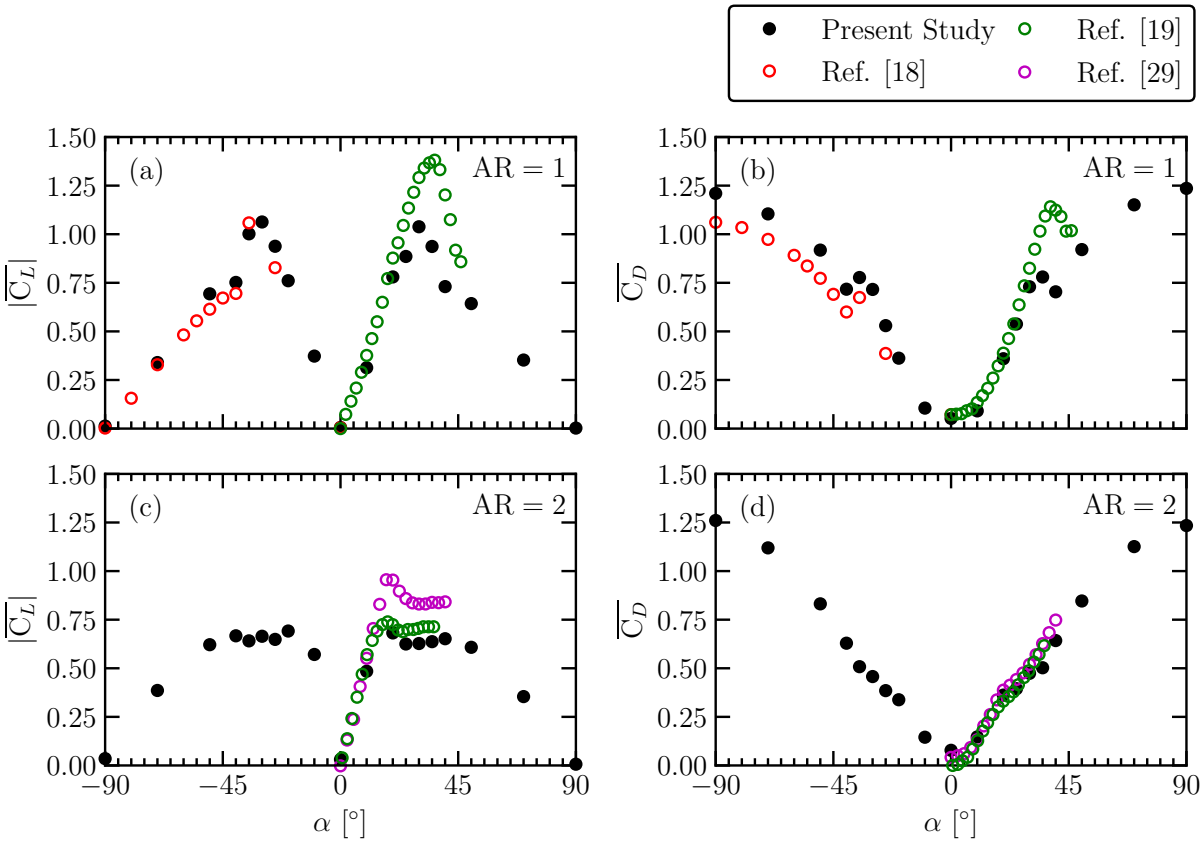


**Figure 4.2:** Time-averaged lift (a,c) and drag coefficients (b,d) in free flight for AR = 1 (top row) and AR = 2 (bottom row). Data are from the following sources: Ortiz *et al.* [18] at $\mathrm{Re}_c$ = 210 000, DeVoria & Mohseni [19] at $\mathrm{Re}_c$ = 80 000, and Bleischwitz *et al.* [29] at $\mathrm{Re}_c$ = 56 000. Uncertainty is accommodated by the marker size.

Data reported by Ortiz *et al.* [18] (reproduced in Fig. 4.2) show good agreement with the present study, replicating local extrema in the lift and drag coefficients and following the same general trends. Force coefficients reported by Bleischwitz *et al.* [29] and DeVoria & Mohseni [19] also match the present results well at lower angles of attack. However, both studies report notably higher maximum lift coefficients. This is likely due to their use of rounded leading edge models, whereas both the present study and Ortiz *et al.* [18] employed plates with flat leading edges. The rounded leading edge designs are expected to delay stall by promoting smooth flow around the leading edge.

Lift and drag coefficients for all gap ratios tested are presented in Fig. 4.3. Notably, varying $l/c$ does not fundamentally change the overall loading trends with respect to $\alpha$ in comparison to the free flight case (Fig. 4.2). The most substantial differences between gap ratio conditions are evident near the maximum lift angle. The lift coefficient for AR = 1 is more sensitive to gap ratio at negative incidence angles, whereas, loading coefficients for AR = 2 are virtually invariant across gap ratios at negative angles, while notable changes are observed in the forcing at positive angles of attack. Figure 4.3 suggests that ground effect is significant between $-35° \leq \alpha \leq -10°$ for AR = 1 and $10° \leq \alpha \leq 40°$ for both aspect ratios.

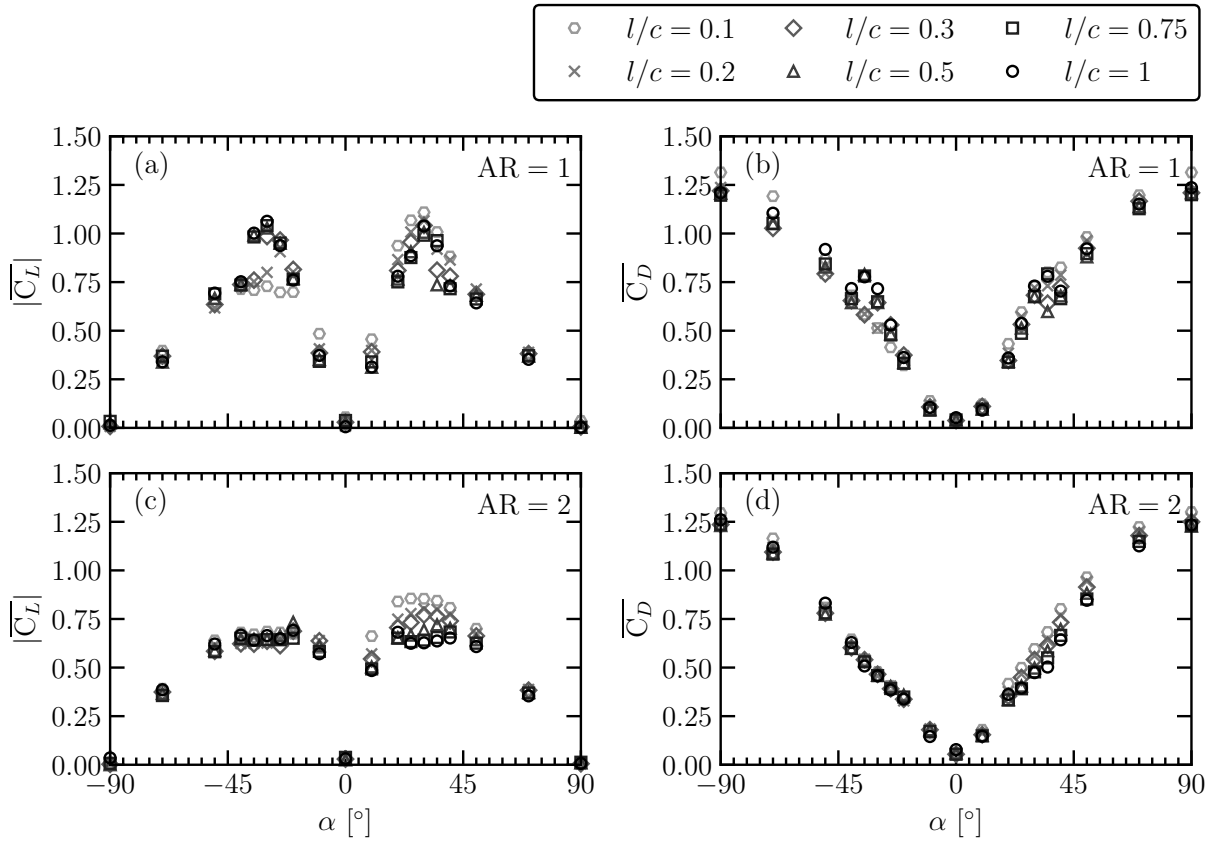


**Figure 4.3:** Time-averaged lift (a,c) and drag coefficients (b,d) for AR = 1 (top row) and AR = 2 (bottom row) for all tested $l/c$. Uncertainty is accommodated by the marker size.

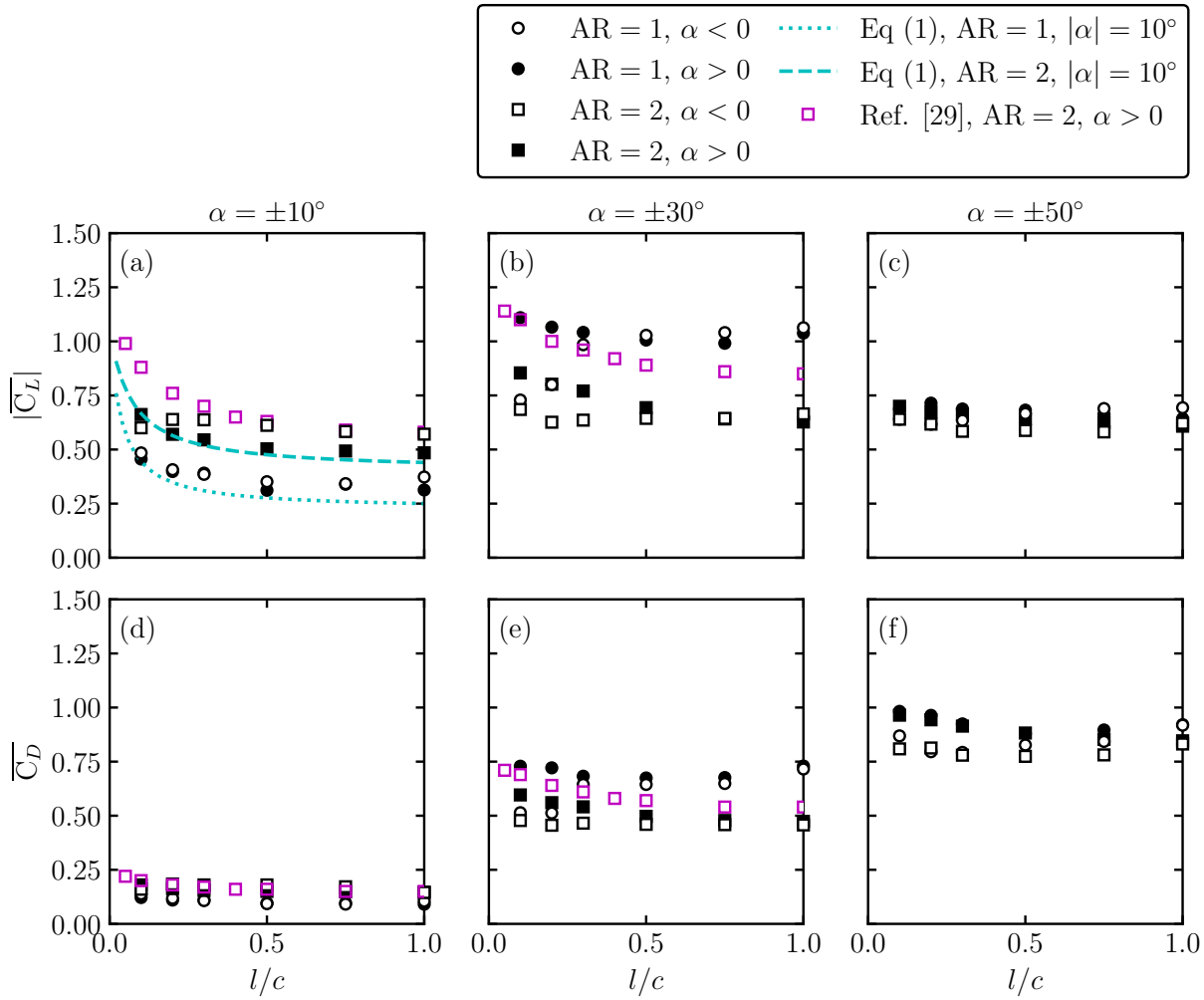


**Figure 4.4:** Lift (top row) and drag (bottom row) variation with $l/c$ for (a,d) $\alpha = \pm 10°$, (b,e) $\alpha = \pm 30°$, and (c,f) $\alpha = \pm 50°$. Experimental data is sourced from Bleischwitz *et al.* [29]. Uncertainty is accommodated by the marker size.

To better elucidate the effect of gap ratio on structural loading $|\overline{C_L}|$ and $\overline{C_D}$ at $\alpha = \pm 10°, \pm 30°$, and $\pm 50°$ are plotted in Fig. 4.4 with respect to $l/c$. Also included are theoretical predictions and experimental measurements for inclined flat plate geometries. The theoretical lift estimations are based on a modification of the Helmbold equation for finite wings[198] given by

$$\overline{C_L} = \frac{2\pi}{\sqrt{1 + \left(\frac{2}{AR_{GE}}\right)^2} + \frac{2}{AR_{GE}}}\alpha, \tag{4.1}$$

where

$$AR_{GE} = AR\left(1 - \frac{1 - 1.32\,(l/c)}{1.05 + 7.4\,(l/c)}\right). \tag{4.2}$$

Equation 4.1 predicts the lift coefficient for a plate in ground effect based on an effective ground effect aspect ratio, $AR_{GE}$, which is estimated from Prandtl's lifting line theory [199].

For $\alpha = \pm 10°$ and $\pm 30°$ (Figs. 4.4a and 4.4b), the lift coefficient changes by at least 5% relative to free flight for $l/c < 0.5$. Previous studies have reported critical gap ratios between 0.8 to 1 for two-dimensional geometries [155–157]. As such, Fig. 4.4 suggests that the onset of ground effect is dependent on aspect ratio.

At $\alpha = \pm 10°$, the lift coefficient for both aspect ratios, on average, increases with decreasing gap ratio (Fig. 4.4a), following the trend expected from Eq. 4.1 for low angles [198, 199]. Results from Bleischwitz *et al.* [29] for AR = 2 also show an increase in lift coefficient with decreasing gap ratio, though their reported lift coefficient is higher, likely due to their rounded leading edge geometry and moving ground [29]. At $\alpha = \pm 30°$, the effect of gap ratio on lift varies based on specific conditions. The lift coefficient increases with decreasing gap ratio at positive angles of attack for both aspect ratios, while a decrease is observed for negative angles at AR = 1. These differences are attributed to associated changes in the stall angle, which is discussed using flow measurements in the next section. At $\alpha = \pm 50°$, the lift coefficients are largely insensitive to changes in gap ratio, with relatively minor variations seen in Fig. 4.4c.

The effect of gap ratio on drag coefficient is presented in Figs. 4.4d–4.4f. At $\alpha = \pm 10°$, the drag coefficient shows minimal sensitivity to changes in gap ratio. As the angle is changed to $\alpha = \pm 30°$, the drag coefficient generally follows the trends observed in the lift coefficient at the same incidence angles. Furthermore, the results reported by Bleischwitz *et al.* [29] for $\alpha = 10°$ and 30° show good agreement with those from the present study. For $\alpha = 50°$ the drag increases with decreasing gap ratio due to the ram effect [154]. At $\alpha = -50°$, there are only minor variations in the drag coefficient with respect to gap ratio. The loading results in Fig. 4.4 indicate that the ground effect phenomenon is dependent on the specific flow configuration (angle of attack and aspect ratio) and does not always result in increased aerodynamic loading.

## 4.4 Midspan Flow Development

To elucidate the physical mechanisms behind the observed changes in aerodynamic loading with aspect ratio, gap ratio, and angle of attack, flow velocity measurements are analyzed for a subset of characteristic conditions (Table 4.1). Herein the discussion focuses on $\alpha = \pm 10°$, $\pm 30°$, and $\pm 50°$ for AR = 1. The AR = 1 at $\alpha = \pm 30°$ flow measurements are also compared to AR = 2 results at $\alpha = \pm 30°$ to assess differences in ground effect phenomenon for low and high AR inclined flat plates.

Figure 4.5 presents time-averaged streamwise velocity fields computed from the midplane planar PIV measurements for AR = 1 at $l/c = 0.1$ and 1. For $\alpha = \pm 10°$, the flow fields are equivalent in free flight between the two orientations (Figs. 4.5a and 4.5g). For both orientations, a recirculation region covering approximately one-third of the plate chord is observed on the suction surface as the leading edge shear layer reattaches onto the model. For $\alpha = 10°$, as the model is placed near the ground, the suction side flow development does not change appreciably. The average velocity on the pressure side decreases, which is expected to result in higher static pressure values, leading to the increase in the forces, as observed in Figs. 4.4a and 4.4d. For $\alpha = -10°$, the

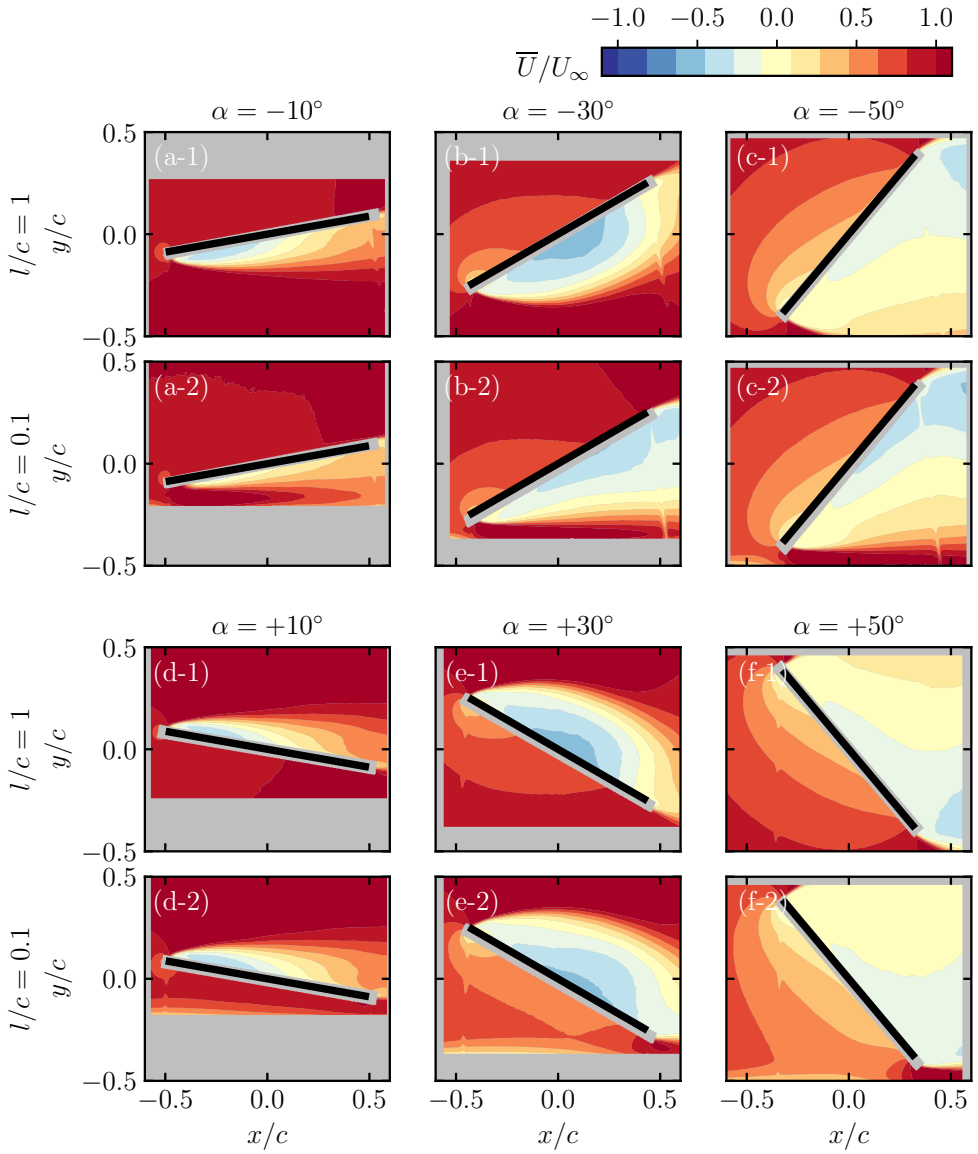


**Figure 4.5:** Time-averaged streamwise velocity fields along the midspan of the AR = 1 plate at $l/c = 1$ and 0.1 for (a) $\alpha = -10°$, (b) $\alpha = -30°$, (c) $\alpha = -50°$, (d) $\alpha = +10°$, (e) $\alpha = +30°$, and (e) $\alpha = +50°$.

recirculation region on the suction side diminishes when the plate is placed at $l/c = 0.1$. This is attributed to the notable increase in average flow velocity over the suction side due to ground proximity. Consequently, the increase in edge velocity is expected to increase suction and hence to increases the lift magnitude (Fig. 4.4a).

For $\alpha = \pm 30°$ at $l/c = 1$, which is near the maximum lift condition, a recirculation region that encompasses the full length of the suction surface is observed. For $\alpha = 30°$, as the gap ratio is decreased to 0.1, the location of the maximum height of the separated flow region moves downstream. The extent of the zero-velocity contour extends beyond the trailing edge, indicating

the plate is stalled. At the same time, the average velocity decreases over the pressure side with decreasing gap ratio. The combined result is an increase in the lift magnitude (Fig. 4.4b). For $\alpha = -30°$, the separated flow topology changes substantially, with the separated shear layer failing to reattach, leading to stall. The substantial changes to the flow over the suction side are accompanied by a notable decrease in the lift and drag coefficients in the vicinity of the ground for this plate orientation (Figs. 4.4b and 4.4e).

For AR = 1 at $\alpha = \pm 50°$, a stalled flow topology is observed in both free flight ($l/c = 1$) and in immediate proximity to the ground ($l/c = 0.1$) for both orientations, resulting in lower lift and higher drag compared to $\alpha = \pm 30°$ (Figs. 4.4c and 4.4f). At $\alpha = 50°$, similar to other positive angles of attack, a decrease in the average velocity over the pressure side is observed with decreasing gap ratio due to the ram effect, which results in an increase in the drag coefficient (Fig. 4.4f). At $\alpha = -50°$, flow over the pressure side remains largely unchanged when $l/c$ is reduced to 0.1. Despite increased streamwise acceleration over the leading edge, the stalled flow topology over the suction side does not change appreciably. Consequently, loading changes with gap ratio are less pronounced for this flow orientation (Figs. 4.4c and 4.4f).

The time-averaged streamwise velocity fields for AR = 1 and 2 at $\alpha = \pm 30°$ and $l/c = 0.1$, 0.2, 0.5, and 1 are presented in Fig. 4.6 to highlight the effect of aspect ratio on flow development. In free flight (top row), the recirculation region that forms due to pinning of the leading edge shear layer by tip vortex downwash is only observed for AR = 1, where influence of the tip vortex over the suction side flow is greater [19, 23]. Results for $\alpha = -30°$ (two leftmost columns) show that flow over the suction side of the AR = 2 model is fully separated in free flight and remains as such for all gap ratios, despite notable changes in flow development near the leading edge at low $l/c$. This is reflected in the loading results (Figs. 4.3 and 4.4), where a discernible change in the forces for AR = 2 is not observed for $\alpha < 0°$ with decreasing $l/c$. In contrast, for AR = 1, the separated shear layer over the suction side reattaches for $l/c = 1$ and stalled conditions are observed only for $l/c < 0.5$. Consequently, higher lift magnitudes are attained at AR = 1 compared to AR = 2 sufficiently far from the ground plane (Fig. 4.4b). For $l/c < 0.5$, the stalled conditions at AR = 1 bring about flow development over the suction side that is similar to AR = 2 for decreasing gap ratio, eventually leading to equivalent lift coefficient values at $l/c = 0.1$.

At $\alpha = 30°$ (two right most columns), the flow fields for AR = 2 show a separated flow topology for all gap ratios investigated, similar to the negatively oriented counterparts. As the gap ratio is decreased, the average pressure side velocity decreases. A similar effect of gap ratio on flow topology at AR = 1 can be observed, with a lower average pressure side velocity for AR = 2 relative to AR = 1. For both aspect ratios, the decrease in velocity is expected to result in an overall increase in static pressure on the lower side of the plate, increasing the lift magnitude, which agrees with the measured loads (Figs. 4.4b and 4.4e).

The results presented in Figs. 4.5 and 4.6 show that, as expected, the effect of ground proximity on the flow over the plate is most pronounced on the side facing the ground. The associated changes in flow development discussed earlier affect the surface pressure distribution and thus aerodynamic loading. To quantify changes in surface pressure due to ground effect, the mean relative pressure fields were computed based on the Reynolds-Averaged Navier-Stokes formulation of the Poisson equation [200–202] using the algorithm developed by McClure and Yarusevych [203]. In nearly all cases, a Dirichlet boundary condition based on the Bernoulli equation is

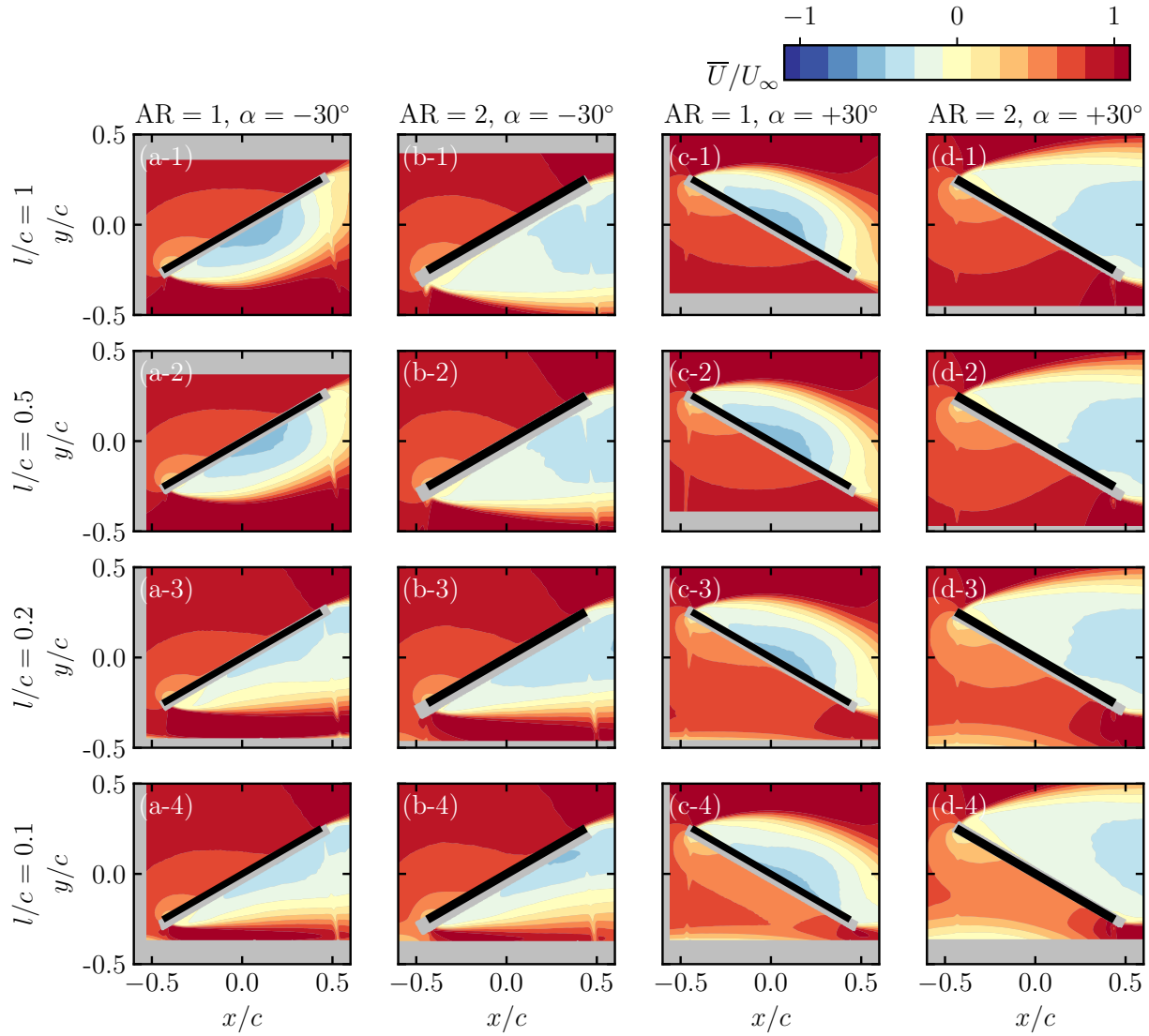


**Figure 4.6:** Time-averaged streamwise velocity at the plate midspan for (a) AR = 1 at $\alpha = -30°$, (b) AR = 2 at $\alpha = -30°$, (c) AR = 1 at $\alpha = +30°$, and (d) AR = 2 at $\alpha = +30°$ between $l/c = 1$ and $l/c = 0.1$.

applied along the top FOV boundary. The exception to this is for the AR = 2 model in free flight at negative angles of attack and for the AR = 1 model at $l/c = 0.1$ and positive angles of attack, where a Dirichlet boundary condition is applied along the bottom FOV boundary to obtain physically realistic pressure distributions. For all other boundaries, a Neumann boundary condition based on the pressure gradient computed using the Navier-Stokes equations is applied. The results are depicted in Fig. 4.7 for AR = 1 and 2 at $\alpha = \pm 30°$.

At $\alpha = -30°$, the suction side pressure magnitudes for AR = 1 are higher in free flight relative to $l/c = 0.1$ due to the presence of the recirculation region (Fig. 4.6). As the stall angle decreases for $l/c < 0.5$ (Fig. 4.3), peak negative pressure magnitudes decrease, leading to a decrease in lift and drag coefficients (Figs. 4.4b and 4.4e). The relative pressure fields for the AR = 2 plate

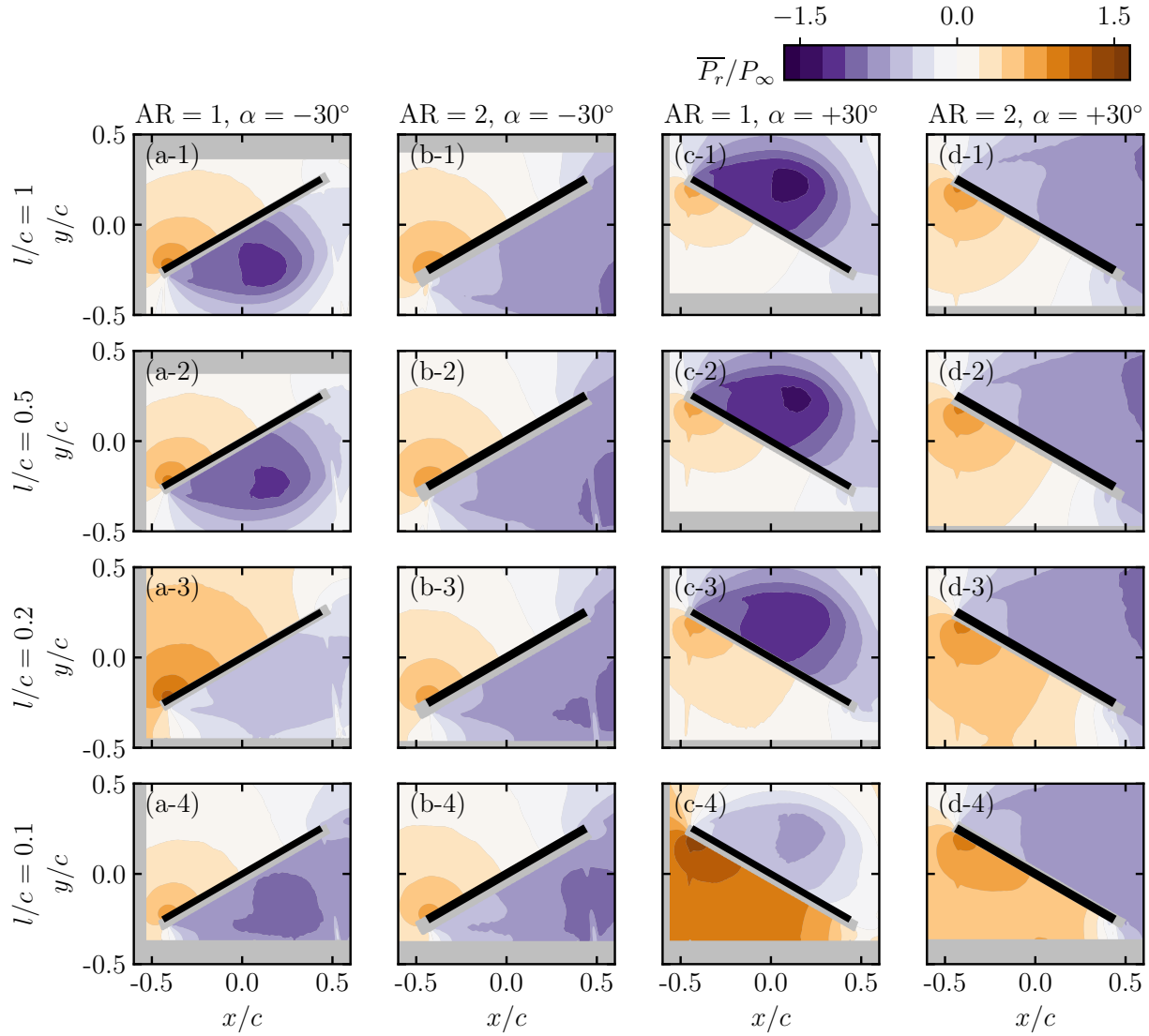


**Figure 4.7:** Mean relative pressure fields computed from midspan velocity measurements in Fig. 4.6 for (a) AR = 1 at $\alpha = -30°$, (b) AR = 2 at $\alpha = -30°$, (c) AR = 1 at $\alpha = +30°$, and (d) AR = 2 at $\alpha = +30°$ between $l/c = 1$ and $l/c = 0.1$.

at $\alpha = -30°$ do not change significantly with decreasing $l/c$, as the flat plate is stalled, which supports the observed low sensitivity of $|\overline{C_L}|$ and $\overline{C_D}$ to changes in $l/c$ (Figs. 4.4b and 4.4e). At $\alpha = 30°$, the average pressure beneath the plate increases with decreasing $l/c$ for both aspect ratios due to the increase in ram pressure, which agrees with the decrease in average velocity underneath the plate seen in the streamwise velocity fields in Fig. 4.6.

Since the discussed flow measurements and pressure reconstructions pertain to the centre plane of the highly three-dimensional flow, it is instructive to consider if the sectional flow behaviour reflects the associated change in the total plate loading due to ground effect. To this end, Fig. 4.8 compares the sectional lift coefficient, $\overline{C_l}$, based on the reconstructed mean pressure fields and measured time-averaged lift coefficients. Pressure distributions along the upper and lower surfaces

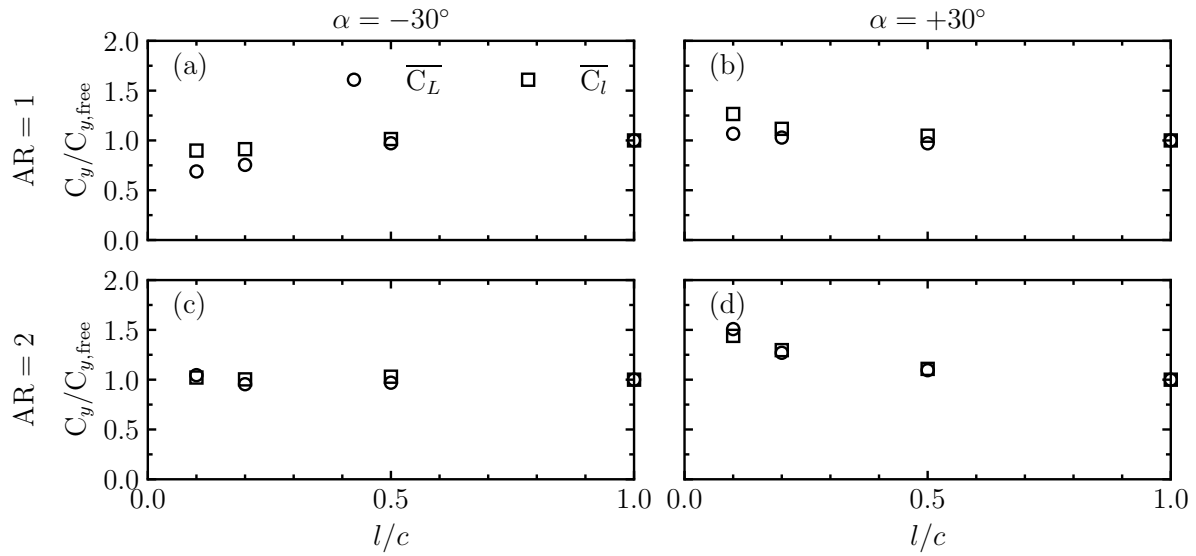


**Figure 4.8:** Time-averaged lift coefficients based on force balance measurements ($\overline{C_L}$) and sectional lift coefficients based on mean relative surface pressures ($\overline{C_l}$) for (a) AR = 1 at $\alpha = -30°$ (b) AR = 1 at $\alpha = +30°$, (c) AR = 2 at $\alpha = -30°$, and (d) AR = 2 at $\alpha = +30°$. Both total and sectional lift coefficients are normalized by the respective forces under free flight conditions. Uncertainty is accommodated by the marker size.

of the masked region (greyed out areas in Fig. 4.6) are used due to the high uncertainty of the measurements near the model surfaces. To facilitate comparisons between the sectional and measured lift coefficients, both are normalized by the corresponding free flight values. Overall, the sectional lift coefficient estimates follow the trends seen in the total lift coefficient. Notable differences between the sectional and total lift coefficients are observed only for AR = 1 when $l/c < 0.5$, which is attributed to the increase in the spanwise flow variation compared to the higher aspect ratio. For these cases, the sectional lift coefficients are larger, providing a conservative estimate of actual lift. These results are expected to be particularly useful for in-field deployments of high AR solar panels, where surface pressure measurements combined with free flight loading coefficients can be utilized for load estimations in lieu of more laborious velocity measurements.

## 4.5 Tip Vortex Characteristics

The foregoing discussion of the aerodynamic loading and streamwise flow field measurements highlights a significant effect of aspect ratio on flow development for all gap ratios tested. This suggests tip vortices significantly influence aerodynamic performance of low aspect ratio plates and wings [19, 130, 204]. The development of the tip vortices was investigated using cross plane flow measurements following the same test matrix as the streamwise flow measurements (Table 4.1). The results are analyzed in the following discussion to characterize the effect of angle of attack, gap ratio, and aspect ratio.

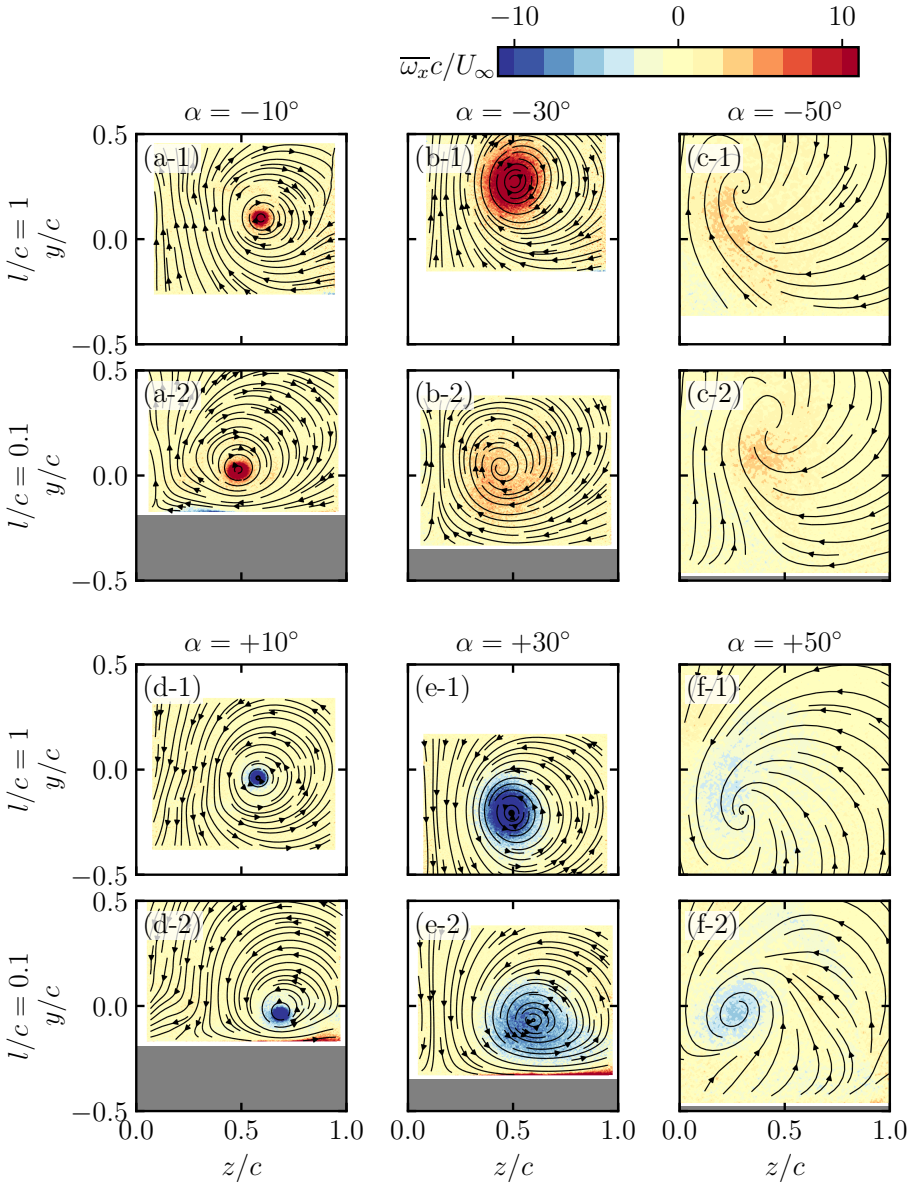


**Figure 4.9:** Time-averaged streamwise vorticity one chord length away from the trailing edge of the AR = 1 plate at $l/c = 1$ and 0.1 for (a) $\alpha = -10°$, (b) $\alpha = -30°$, (c) $\alpha = -50°$, (d) $\alpha = +10°$, (e) $\alpha = +30°$, and (e) $\alpha = +50°$. The ground is indicated by the grey regions.

Figure 4.9 presents time-averaged streamwise vorticity contours and streamlines capturing one tip vortex for the AR = 1 model at the smallest gap ratio ($l/c = 0.1$) and in free flight ($l/c = 1.0$). For $\alpha = \pm 10°$ in free flight, the vortex core is located nearly level with the spanwise edge of the model ($z/c = 0.5$) and aligned with the trailing edge in the wall-normal direction ($y/c = \pm 0.10$). With decreasing gap ratio, the vortex core position for $\alpha = -10°$ shifts towards the plate centre, whereas for $\alpha = 10°$, it moves outboard. These changes in the vortex core location are consistent with the expected influence of the image vortex system reflected across the ground plane.

As the angle of attack is increased to $\alpha = \pm 30^\circ$, the centre of the vortex remains relatively close to the trailing edge position in the wall normal direction ($y/c = \pm 0.25$) and near the plate end location ($z/c = 0.5$) for free flight ($l/c = 1$). As the gap ratio is decreased to $l/c = 0.1$, the vortex moves outboard and inboard for positive and negative orientations, respectively, similar to the $\alpha = \pm 10^\circ$ case, and the average vorticity magnitude decreases. However, the vortex core is notably larger and becomes more eccentric with decreasing gap ratio in comparison to the lower angle of attack. The decrease in average vorticity magnitude is greater for negative orientations due to the onset of stall with decreasing gap ratio (Fig. 4.6), leading to the formation of a weaker tip vortex. Although the flow is in an early stage of stall for positive orientations at $l/c = 0.1$, the average tip vortex vorticity is higher relative to negative orientations at the same gap ratio. This is attributed to the ram effect observed only for $\alpha > 0$, which results in an increase in pressure difference between pressure and suction sides and a stronger tip vortex.

Increasing the angle of attack to $\pm 50^\circ$ results in a decrease in the average vorticity magnitude in the cross plane for both $l/c$ values. The streamlines indicate that there is a swirling motion of the in-plane flow and a relatively weak tip vortex is present based on the vorticity magnitude. The low vorticity magnitude is attributed to the post-stall flow at $\alpha = \pm 50^\circ$ (Fig. 4.5) expected to produce a weaker tip vortex.

Figure 4.10 presents the cross-plane vorticity fields for AR = 1 and 2 at $\alpha = \pm 30^\circ$ for $l/c$ =0.1, 0.2, 0.5, and 1.0. As discussed earlier, for this angle of attack, notably higher aerodynamic loads are observed on the plate at AR = 1 compared to those at AR = 2 (Fig. 4.4). Furthermore, earlier stall is observed in free flight conditions for the higher aspect ratio model (Fig. 4.6). The results in Fig. 4.10 confirm the earlier speculation that the observed changes in force and flow behaviours at the midplane are closely related to the tip vortex characteristics. Specifically, at AR = 1, a considerably stronger tip vortex is observed than at AR = 2 at the same gap ratio. The results for AR = 1 also clearly illustrate a progressive decrease in streamwise vorticity magnitude for the tip vortices, lateral movement of the vortex core, and core deformation with decreasing gap ratio. The reduction in vorticity magnitude is most notable for $l/c \leq 0.2$, correlating with the onset of stall (Fig. 4.6). In contrast, the relative changes in tip vortex characteristics for AR = 2 are less substantial since the plate remains in a stalled configuration for all gap ratios.

To facilitate quantitative analysis of tip vortex strength, circulation estimates were obtained using a vortex identification routine based on the $\lambda_2$ criterion [189]. The tip vortex boundary was identified as the largest continuous closed contour of $\lambda_2$ verified to contain the vortex cores observed in Figs. 4.9 and 4.10. A convergence study was conducted using computed circulation of the identified vortex with respect to the threshold $\lambda_2$ value as a metric. The threshold $\lambda_2$ level was selected to be the lowest value wherein the computed circulation was converged to within 3%. The tip vortex circulation, $\overline{\Gamma_{TV}}$, was computed by integrating the vorticity contained within the selected closed contour of $\lambda_2$.

To quantify the effect of vortex tilt on computed circulation, a Lamb-Oseen vortex was used to create a synthetic velocity volume and the vortex identification routine was implemented on velocity fields projected onto a slice plane with tilt angles between $0^\circ$ and $90^\circ$ to the vortex centre axis. By assuming the local vortex tilt angle is equivalent to the plate angle as a conservative estimate, the variation of computed circulation relative to zero tilt was found to be less than 8% for all cases. The maximum uncertainty in computed circulation estimates incorporating

the methodology and effects of vortex tilt relative to the measurement plane is estimated to be $\overline{\Gamma_{TV}}/(cU_\infty) = \pm 0.04$.

The effect of angle of attack on the normalized tip vortex circulation $\overline{\Gamma_{TV}}/(cU_\infty)$ is quantified in Fig. 4.11a for AR = 1. Tip vortex circulation increases for pre-stall angles, similar to the results of Linehan and Mohseni [23]. A notable decrease in the tip vortex circulation is observed post-stall ($\alpha > 30°$ in the present study). On the average, decreasing gap ratio leads to reduction in circulation magnitude, with the effect being more pronounced at negative angles angles of

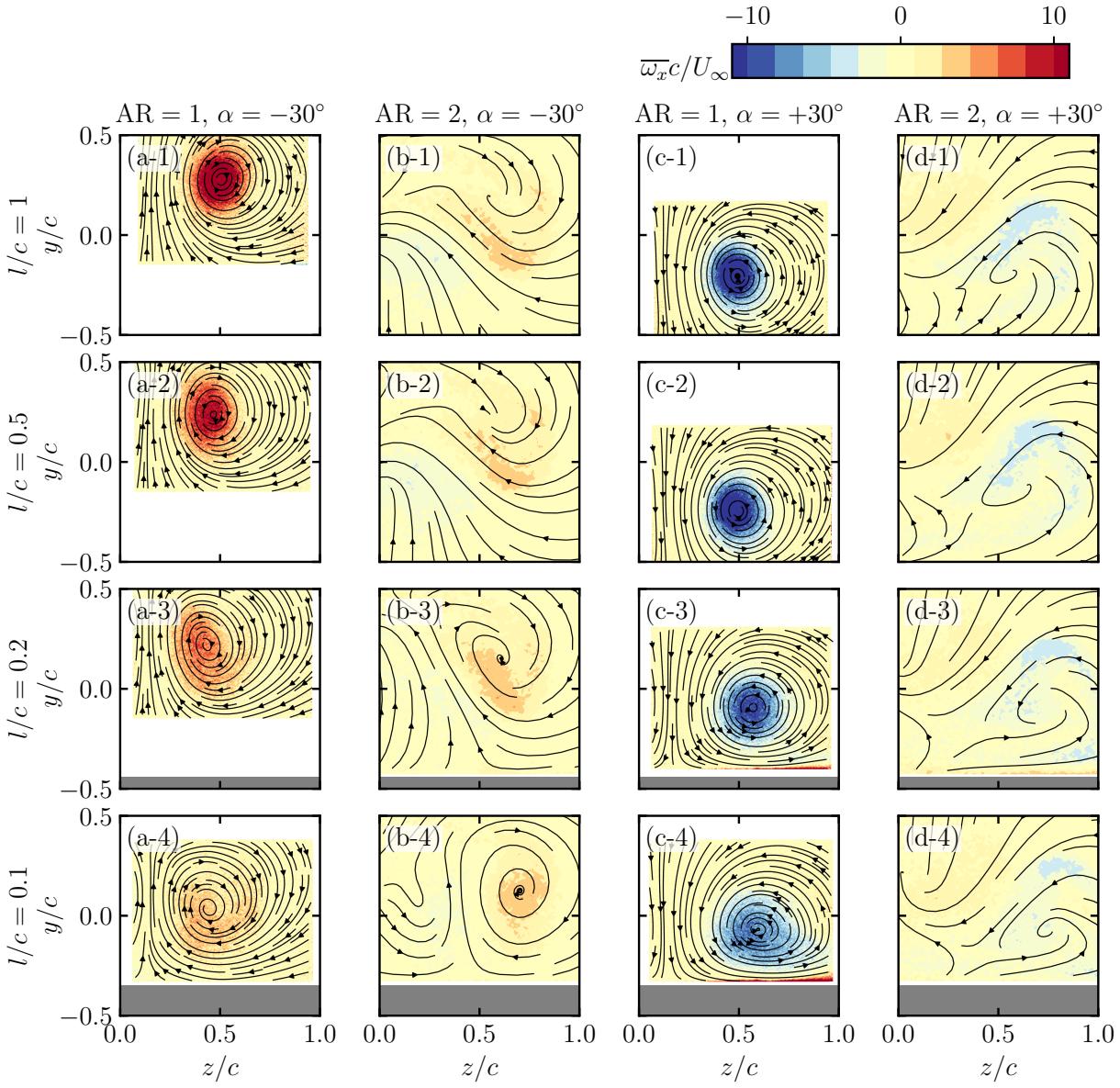


**Figure 4.10:** Time-averaged streamwise vorticity fields one chord length away from the trailing edge for (a) AR = 1 at $\alpha = -30°$, (b) AR = 2 at $\alpha = -30°$, (c) AR = 1 at $\alpha = +30°$, and (d) AR = 2 at $\alpha = +30°$ between $l/c = 1$ and $l/c = 0.1$. The ground is indicated by the grey regions.

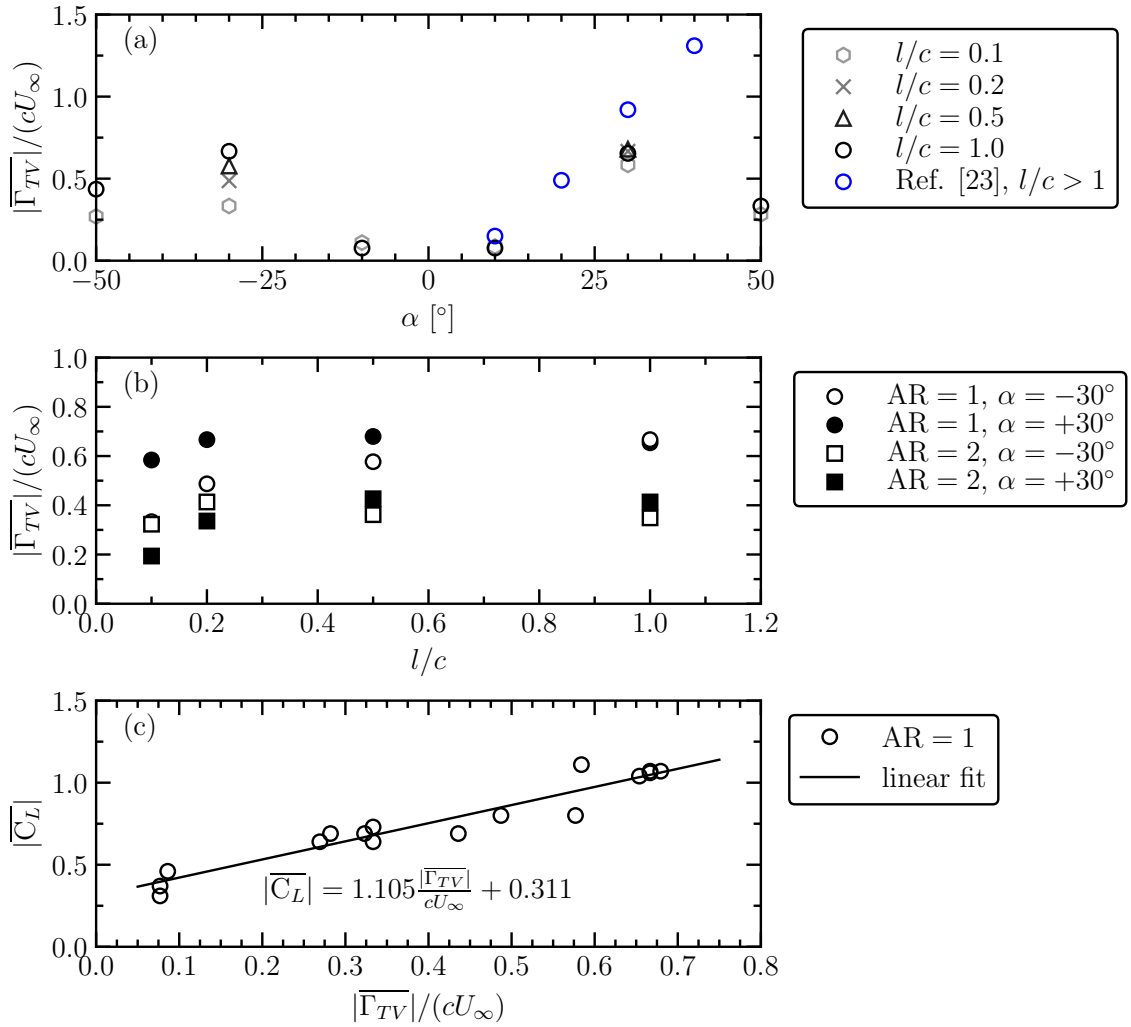


**Figure 4.11:** Variation of tip vortex circulation estimates based on $\lambda_2$ criterion with (a) $\alpha$ and (b) $l/c$. Lift coefficients are plotted against the normalized tip vortex circulations in (c) for AR = 1. Data plotted using blue empty circles is sourced from Linehan & Mohseni [23] in (a). Uncertainty is accommodated by the marker size.

attack (Fig. 4.3). This is also seen in Fig. 4.11b, which presents the circulation magnitude as a function of $l/c$ for $\alpha = \pm 30°$ (corresponding to the angle of attack with maximum circulation from Fig. 4.11a). For AR = 1 at $\alpha = -30°$, tip vortex circulation is observed to decrease from $l/c = 1$ to 0.5 prior to fully stalled flow at the midspan (Fig. 4.10), suggesting the tip flow is more sensitive to $l/c$ compared to the midspan flow. In contrast, for $\alpha = 30°$, tip vortex circulation is relatively constant for $l/c \geq 0.2$. Below $l/c = 0.2$, the plate stalls (Fig. 4.6) and tip vortex vortex circulation drops. Tip vortex circulation is significantly lower for AR = 2 due to onset of stall at lower angles of attack. In combination with the lower loading observed for AR = 2, this provides quantitative evidence in support of the speculation that tip vortices may delay stall and lead to higher aerodynamic loads on low AR plates [19].

The relation between the lift coefficient and tip vortex circulation is explored in Fig. 4.11c for AR = 1. A linear fit to the data provides an empirical relationship given by

$$\overline{C_L} = 1.1105 \frac{|\overline{\Gamma_{TV}}|}{cU_\infty} + 0.311, \tag{4.3}$$

which can be useful to estimate lift forces using tip vortex characteristics, when direct force measurements are not readily available.

## 4.6 Concluding Remarks

This chapter presented an experimental investigation that explored the effect of ground proximity on time-averaged flow around, and loads on, finite-span inclined flat plates. Two plates of AR = 1 and 2 were explored with gap ratios between the plate and ground ranging from free flight ($l/c = 1$) to ground effect regimes ($l/c = 0.1$, 0.2, 0.3, 0.5, and 0.75). The streamwise flow over the plate midspan and the tip vortex one chord away from the trailing edge were captured using two- and three-component planar PIV, respectively, at a chord based Reynolds number of 50 000. The flow measurements were accompanied by direct mean lift and drag characterization to elucidate the physical mechanisms related to plate loading when in ground effect.

Direct force measurements in free flight show that stall occurs at $\alpha = \pm 30°$ and $\pm 20°$ for AR = 1 and 2, respectively. Ground effect is most significant near the stall angle for $l/c < 0.5$ for both aspect ratios, however, the loading increments are dependent on AR and orientation. For AR = 1, the loads increase at low pre-stall angles ($|\alpha| \approx 10°$) with a decrease in $l/c$. With an increase in angle of attack, close to the free flight stall angle, the loads increase for positive angles, but decrease for negative angles. For AR = 2, the combined loading has a relatively low sensitivity to $l/c$ for all negative orientations tested and increases for positive angles up to deep-stall ($\alpha \leq 50°$). Ground proximity has a lessened effect on overall loading for both aspect ratios at deep-stall angles. The maximum lift and drag increased within a range from 4% to 26% between $l/c = 1$ and $l/c = 0.1$ for both AR at positive angles of attack. At negative angles of attack for AR = 1, the ground effect resulted in a lift coefficient decrease of 31% and a drag coefficient increase of 8%, whereas at AR = 2, as appreciable change in loading with gap ratio was not observed between $l/c = 1$ and $l/c = 0.1$.

Flow measurements revealed the aerodynamic mechanisms responsible for structural load variations with $l/c$. Variations to the midplane streamwise flow topology near the stall angle were observed below $l/c = 0.5$. These changes were also accompanied by a notable decrease in the strength of the tip vortex, reflected in a decrease in circulation. For AR = 1 at low pre-stall angles ($|\alpha| \approx 10°$), there is an increase in edge velocity over the suction side and the tip vortices are largely unaffected by the lower gap ratios, causing increased suction relative to free flight, increasing lift with minimal changes in drag. Increasing the angle of attack close to the stall angle, the leading-edge shear layer reattachment point on the suction side moves downstream towards the trailing edge, aiding in high lift generation in free flight. At gap ratios below $l/c = 0.5$, midspan streamwise flow topologies change towards modified stall conditions for both orientations. However, pressure reconstructions at the midspan plane show a significant ram effect, i.e., increase

in pressure on the pressure side, is attained in ground proximity for positive angles of attack, which results in an overall increase in loading at positive orientations despite signs of stall onset at the midspan. The absence of ram effect for negative orientations results in a decrease in aerodynamic loading with the onset of stall as the gap ratio is decreased. Consequently, for a given gap ratio, the tip vortex is stronger for positive orientations relative to negative orientations. For AR = 2, the lack of significant ground effect on loading at negative plate orientations is shown to be attributed to lack of changes in the midspan flow and tip vortex development. At positive orientations, however, the ram effect leads to increased loads similar to the lower aspect ratio. Under deep-stall conditions, a significant portion of the plate is expected to be out of ground effect with the flow remaining largely unchanged with $l/c$, diminishing ground effect related loading variations.

The results of the present study suggests that ground effect has the most substantial influence on aerodynamic loads generated on inclined plates placed near the stall angle ($20^\circ \leq \alpha \leq 40^\circ$), particularly for aspect ratios close to unity. In terms of photovoltaic installations, based on the typical angles used for maximizing solar irradiance [32, 117], such plates angles are most relevant to installations between latitudes $\pm 30^\circ$ to $\pm 50^\circ$ (e.g., United States of America, central Asia and Europe, and southern Canada, Australia, and Africa). In these regions, maximum loading on plates installed in ground vicinity ($l/c < 0.5$) may change between 20% to 30% relative to cases where ground effect is not present. Consequently, ground effect should be taken into design considerations for isolated installations and perimeter units. Additionally, similar considerations are warranted for other civil structures, such as windbreaks.

# Chapter 5

# Impact of Yaw Angle on Steady Aerodynamics of Flat Plates in Ground Effect

*The results presented in Chapter 4 demonstrate that ground proximity effects are strongly dependent on the wind direction. As such, the effects of the yaw angle on aerodynamic loading, suction side flow development, and tip vortex development are considered here for a square flat plate in ground effect near the free flight stall angle. The results show that ground effect is significantly modified by yaw angle. The analysis of qualitative and quantitative flow measurements are used to explain the flow physics at play and link it to the observed loading trends.*

Parts of this chapter have been adapted from

Pieris, S., Yarusevych, S., & Peterson, S. D. 2023 Effect of yaw angle on aerodynamics of square inclined flat plates in ground effect. *Phys. Fluids* **35** (5). DOI.

## 5.1 Introduction

The results presented in Chapter 4 and discussion of previous literature in Sections 2.3.3 and 2.4 point to notable variations in aerodynamics of finite-span inclined flat plates in close ground proximity with wind direction (or yaw angle). Particularly, under headwind conditions ($\beta = 0°$), the ram effect leads to increased loading, while for tailwind conditions ($\beta = 180°$), the increased edge velocity near the trailing edge leads to earlier stall and decreased aerodynamic loading when in close ground proximity. Previous studies on aerodynamic effects of $\beta$ focused primarily on force measurements and have not addressed the relation between the observed loading and changes in flow topology for low AR plates with respect to $\beta$. However, some insight into the associated aerodynamic mechanisms can be gained based on studies that examine low AR plates in side-slip, where $\alpha$ is kept constant with varying $\beta$. Devoria and Mohseni [19, 120] measured forces on and flow around a square flat plate inclined at $\alpha = 35°$ for $\beta < 35°$ at $\mathrm{Re}_c = 80\,000$. As $\beta$ increased, the circulations associated with the tip vortices decreased and the "pinning" effect on the leading-edge shear layer reduced, marked by disappearance of stall cell flow patterns [121]. This led to a decrease in the relatively high lift and drag observed at $\beta = 0°$ with increasing $\beta$. For a yawed configuration, as $\beta \to 90°$, effective $\alpha$ tends to zero, resulting in a decrease in lift and drag coefficients from their peak values at $\beta = 0°$ [26, 28, 31]. Although in both side-slip and yawed configurations the loading is expected to decrease, it is not expected to decrease at the same rate as $\beta \to 90°$ due to the difference in the relationship between $\beta$ and $\alpha$, which is also expected to results in significantly different flow development between the two configurations.

The results of the previous chapter and relevant literature points to a notable variation in ground effect aerodynamics with respect to $\beta$. Previous studies that have examined ground effect aerodynamic mechanisms have been limited to either $\beta = 0°$ or 180°. Although a number of studies motivated by photovoltaic applications have investigated other $\beta$ values, the effects of $l/c$ and $\alpha$ on structural loading were not decoupled [26, 30, 31, 205], confounding the effect of $\beta$ on the aerodynamics. The investigation presented in this chapter addresses a need for a systematic investigation that considers the effects of $l/c$ and $\beta$ on low AR aerodynamics. Experimental flow and force measurements are used to clarify ground effect-related aerodynamic mechanisms associated with variations of key parameters relevant to photovoltaic installations.

## 5.2 Experiment Details

The flow development around a square inclined flat plate and the associated aerodynamic loading was investigated experimentally for the full range of wind direction ($0° \leq \beta \leq 180°$) and gap ratios spanning free flight and moderate ground effect conditions ($0.1 \leq l/c \leq 1$). In alignment with relevant literature on low aspect ratio aerodynamics and wind tunnel testing terminology, the term free flight is used to indicate operating conditions sufficiently far away from the ground, while freestream indicates flow unaffected by the ground surface The experimental setup is shown in Fig. 5.1. A Cartesian coordinate system was established with the origin at the intersection of the ground plane and sting rotation axis. The coordinate system was aligned such that the freestream flow was along the $x$ direction, the $y$ direction was wall-normal, and $z$ defined the transverse

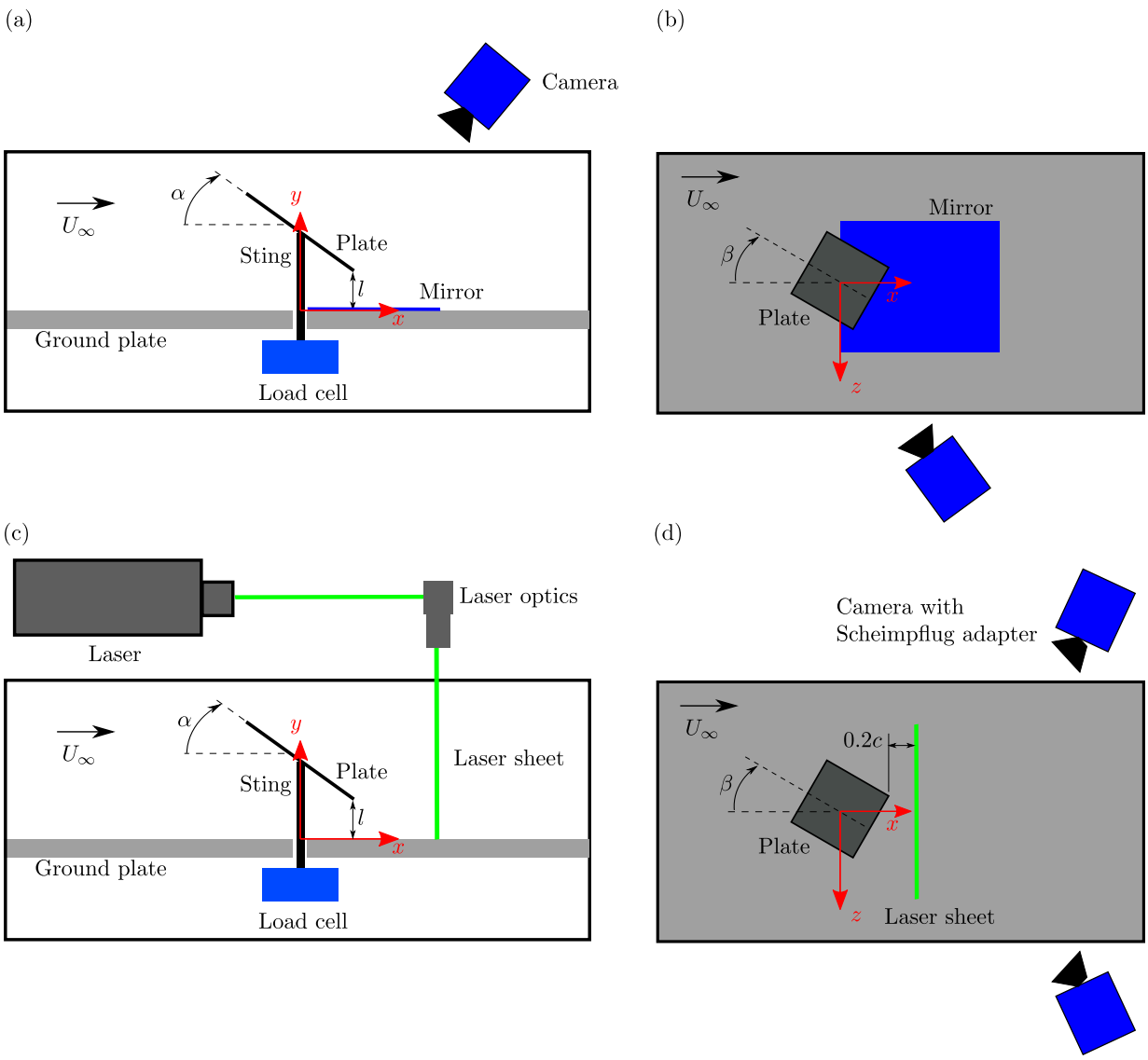


**Figure 5.1:** Schematic of the experimental setup for (a) and (b) flow visualization and (c) and (d) cross-plane SPIV measurements. Side view is shown in the left column and top view is shown in the right column.

direction. A square flat plate model with chord length $c = 102$ mm made of 3.18 mm thick acrylic was used. The model was placed at a fixed angle of attack $\alpha = 30°$ at a minimum gap distance $l$ away from the ground surface. This angle of attack corresponds to the stall angle for a square plate [18, 19] and represents a typical panel angle encountered in the latitude range of 20°-50°, which is relevant to leading global solar energy producers [10] (Fig. 2.1). Maximum compound solid blockage at $\beta = 0°$ and 180° was approximately 2.2% and solid blockage correction was applied to reported loading coefficients [197]. The model was placed on a sting that allowed for adjustment of yaw and pitch to within ±0.2°. Gap distance was adjusted by using stings of different lengths to within 0.5 mm. The loading at the investigated Reynolds number was verified to be within the

Reynolds number independent regime through a Reynolds number sweep up between 25 000 to 210 000, at $\alpha = 30°$, $\beta = 0°$, and $l/c = 1$.

All tests were conducted within the recirculating wind tunnel in the Fluid Mechanics Research Laboratory at the University of Waterloo. The glass test section had a length 2.4 m and a square cross section of side length 0.6 m. Upstream of the test section, flow was conditioned by a honeycomb and set of five mesh screens before accelerating through a 9:1 area ratio contraction. The empty test section freestream uniformity was within ±0.5% over 95% of its cross section and turbulence intensity was less than 0.1%. A ground plate assembly with an elliptical leading edge and an adjustable flap at the trailing edge was placed within the test section for mounting the model assembly. Freestream velocity at the model streamwise position was set based on the contraction pressure drop, calibrated against a Pitot-static tube placed in the center of the test section between the ground plate and the top wall without the solar panel model. The resulting uncertainty of the freestream velocity was less than 3%.

Structural loading, suction surface flow, and cross-plane near wake flow were investigated based on the test matrix specified in Table 5.1. Loads were measured for the full range of yaw angles at finer increments of $\beta$ relative to flow measurements at gap ratios of $l/c = 0.1$, 0.2, 0.5, and 1. Suction surface and cross-plane flow measurements were limited to $l/c = 0.1$ and 1 and $\beta = 0°$, 30°, 45°, 60°, 120°, 150°, and 180°.

Forces and moments along all three axes were measured using a JR3-30E12A4 six degree-of-freedom force/torque sensor mounted underneath the ground plate as shown in Fig. 5.1a. The loading signals were amplified by a JR3 amplifier, which was factory calibrated jointly with the load cell. The calibration and minimum resolution were verified to match the factory specifications using precision weights and were incorporated into the uncertainty estimates of the loading coefficients. For each test case, 300 000 samples were collected at 10 000 Hz, which were ensemble averaged to compute mean forces and moments. For all test cases, sting loads were characterized by decoupling the model from the sting using a separate sting assembly. Time-averaged loads in this decoupled configuration were subtracted from test measurements to account for the contribution of the sting to the measured structural loading. The measured force and moments were normalized by $q_c c^2$ and $q_c c^3$, respectively, where $q_c$ is the solid blockage corrected freestream dynamic pressure [197]. The maximum uncertainty in the reported force coefficients were ±0.04 for lift, ±0.03 for drag and side forces, and ±0.03 for all moment coefficients. The differences in the uncertainties between the force coefficients are a result of the resolution associated with each loading component.

The suction side flow topology was captured using surface oil flow visualization. A thin coating of a mixture consisting of mineral oil, diesel, and fluorescent dye at a ratio of 3:1:1 was

**Table 5.1:** Test matrix of measurements

| Measurement | $\beta$ [°] | $l/c$ |
|---|---|---|
| Loading | 0 - 180, $\Delta = 10$<br>45, 135 | 0.1, 0.2, 0.5, 1 |
| Flow | 0, 30, 45, 60, 120, 150, 180 | 0.1, 1 |

applied to the suction side surface. The oil mixture was brushed onto the surface under quiescent conditions, then the tunnel was immediately started. A 50 W ultraviolet light source was used to illuminate the model. Images were collected every minute for at least two hours after starting the tunnel using a Nikon D7200 camera equipped with a 50 mm lens. A number of optical arrangements were used as shown in Figs. 5.1a and 5.1b, including a mirror in order to provide optical access to the suction side for $\beta > 90°$. Before every run, a calibration target was placed on the model and a snapshot was taken to facilitate dewarping of the images in the presented results.

Three-component, planar stereo-PIV (SPIV) in the cross-flow plane ($z$-$y$) was used to capture the streamwise flow and tip vortex characteristics. Table 5.2 provides an overview of the SPIV parameters. Seeding particles were generated using a glycol-water fog mixture with a mean particle diameter of approximately 1 µm. Illumination of the particles was provided by a Photonics DM20-527 single cavity dual pulsed laser, conditioned into a laser sheet and introduced through the top of the tunnel as shown in Fig. 4.1b. The laser sheet thickness was measured to be approximately 2 mm at the power level used for experiments. Particle images were acquired with two 5.5 Mpx LaVision Imager sCMOS cameras outfitted with Nikon 50 mm lenses set to an aperture number $f_\# = 5.6$. The cameras and lenses were mounted to Scheimpflug adapters resulting in a combined optical angle of 80°. Flow field measurements were collected $0.2c$ downstream of the most leeward point on the model for each test case as shown in Figs. 5.1c and 5.1d. The total field of view was 216.5 mm by 153.1 mm ($2.12c \times 1.50c$). Both the cameras and laser optics were mounted on motorized traverses allowing for precise translation of the imaging plane. A physical calibration using a LaVision 3D calibration plate 106-10 was performed initially, then self-calibration [182] was performed using 100 low seeding density particle images. For each test case, 750 images were

**Table 5.2:** SPIV measurement parameters

| Parameter | Value | Unit |
|---|---|---|
| Laser | Photonics DM20-527 | - |
| PIV Mode | Double frame | - |
| Cameras | LaVision Imager sCMOS CLHS | - |
| Sensor size | $2560 \times 2160$ | px × px |
| Lens focal length | 50 | mm |
| Numerical aperture | 5.6 | - |
| Magnification | 0.08 | - |
| Field of view | $216.5 \times 153.1$ | mm |
| | $2.12c \times 1.50c$ | - |
| Pulse separation | 100 | µs |
| Final window size | $24 \times 24$ (75% overlap) | px×px |
| Vector pitch | 0.5 mm | mm |
| | $0.0049c$ | - |
| Combined optical angle | 80° | |
| Sample rate | 20 | Hz |
| Number of images | 750 | - |

captured at 20 Hz in double frame mode with a pulse separation of 100 µs resulting in particle displacements of less than 10 px. The number of images collected was validated to be sufficient for convergence of relevant time-averaged flow statistics.

Synchronization of the laser and cameras was facilitated by LaVision High Speed V2 controller and DaVis 10 software. The latter was also used for processing of particle images. Prior to calculation of velocity vector fields, the particle images were processed using a sliding minimum subtraction to improve the signal-to-noise ratio. Velocity vector fields were computed using an iterative, multi-pass, cross-correlation algorithm, with a final window size of $24 \times 24$ px with 75% overlap, resulting in vector pitches of 0.5 mm ($0.0049c$). The uncertainty due to random errors in the velocity fields was estimated using the correlation statistics method [186] and uncertainty propagation was used for derived quantities [194]. Associated maximum uncertainty of ensemble-averaged velocities in the wake of the plate away from the ground surface is estimated to be 3% of $U_\infty$ for all three components.

## 5.3 Time-averaged Loading Coefficients

Figure 5.2a presents the time-averaged lift coefficient magnitude for all gap ratios tested. As expected, peak values are observed at $\beta = 0°$ and 180°, and the lift coefficient decreases to a minimum as $\beta \to 90°$ due to the reduction in effective angle of attack. The peak values for free flight range from 1.03 to 1.05 and show good agreement with the previously reported range of 1.04 to 1.38 for a square flat plate pitched close to stall ($30° \leq \alpha \leq 35°$) for $\mathrm{Re}_c \geq 50\,000$ [18, 19, 23]. The loading curves reveal variation of ground effect on lift coefficient with $\beta$. Specifically, for $\beta < 90°$, lift coefficient increases with decreasing gap ratio. The greatest absolute change in the lift coefficient between free flight and $l/c = 0.1$ is observed at $\beta = 60°$. At this yaw angle, lift coefficient increases by 0.21 (48% increase relative to free flight) with decreasing gap ratio. In comparison, lift coefficient at $\beta = 0°$ increases by only 7% with decreasing gap ratio. For

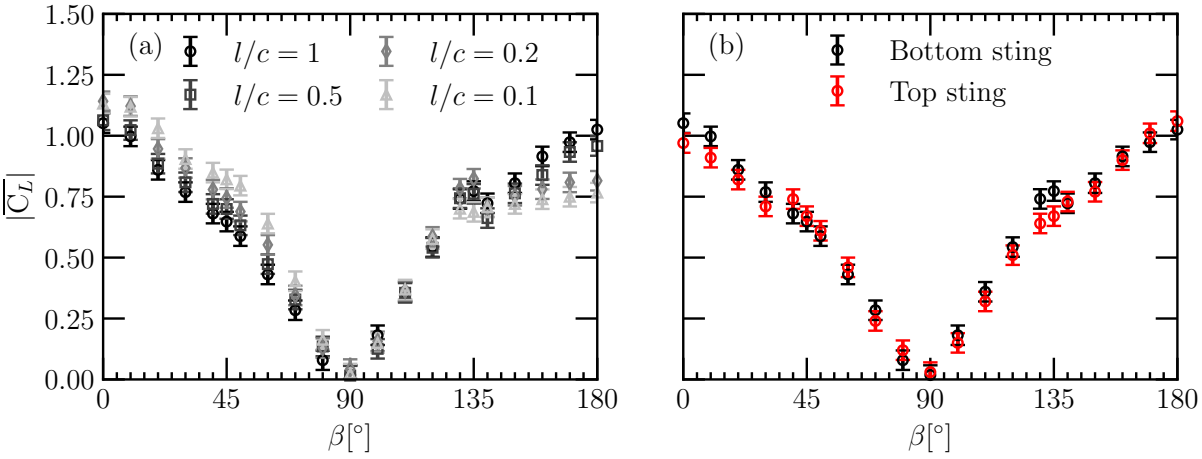


**Figure 5.2:** Time-averaged lift coefficient (a) for all gap ratios tested with a bottom sting mount and (b) for top and bottom sting configurations at $l/c = 1$.

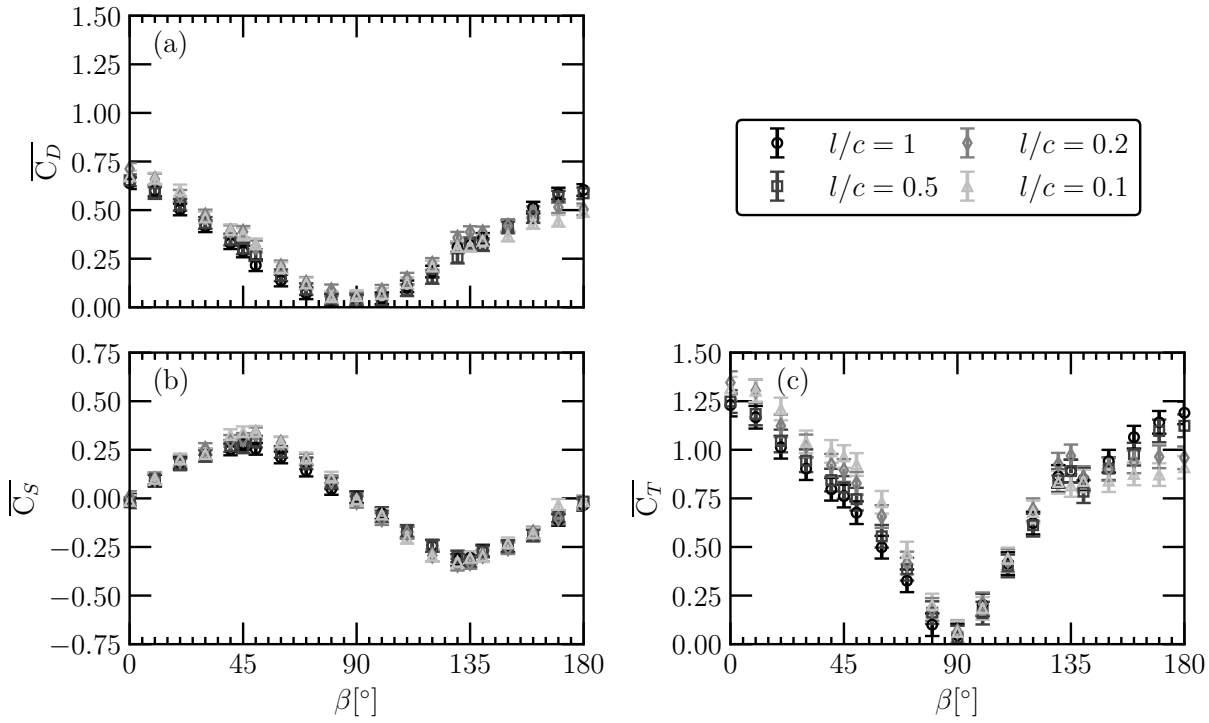


**Figure 5.3:** Time-averaged (a) drag, (b) side, and (c) total force coefficients for all gap ratios tested.

$90° \leq \beta \leq 120°$, no significant changes with gap ratio are observed in lift coefficient magnitudes. For $150° \leq \beta \leq 180°$, there is a marked decrease in lift coefficient as $l/c$ decreases. In this range, the decrease in lift between free flight and ground effect cases becomes greater with an increase in $\beta$, with the greatest difference of 0.26 (34%) observed at $\beta = 180°$.

At $\beta \approx 135°$, there is a local maximum observed in the lift coefficient magnitudes at $l/c = 1$ (Fig. 5.2a), which is not observed for $0° < \beta < 90°$. The asymmetry in the loading profiles about $\beta = 90°$ is attributed to the sting placement, which was verified using a top side (non-ground facing) sting attachment. The lift coefficient magnitudes for the two sting configurations are presented in Fig. 5.2b for $l/c = 1$. The results show nearly mirrored lift coefficient distributions about $\beta = 90°$ for the two configurations, with the local peak observed at $\beta = 40°$ and 135° for the top and bottom sting placements, respectively. The results suggest that the sting effect is most prominent when the sting is placed on the suction side. Although it was verified to diminish in ground effect, the observed influence of stings should be taken into account for load characteristic of actual installations and when comparing experimental data with different model support arrangements (e.g., in Refs. [25, 26, 122, 206]). Here, the remaining results are presented for the bottom sting configuration, which is representative of common photovoltaic support designs [13].

Figure 5.3 presents time-averaged drag, side, and total force coefficients for all test cases. The drag coefficient closely follows the trends observed in lift coefficient. Peaks free flight values are observed at $\beta = 0°$ and 180° within the range 0.60 to 0.64 and are in agreement with the results reported in Chapter 4 and by Ortiz *et al.* [18] (0.67 to 0.75) for flat edge square plates near stall. The gap ratio effects are modulated by $\beta$ similar to those seen in lift with some minor differences. For $\beta < 90°$, decreasing gap ratio results in an increase in drag coefficient and the largest increase of 0.10 (33%) is observed at $\beta = 50°$. Comparatively, peak drag coefficient at $\beta = 0°$ increases by 7%. For $90° < \beta \leq 120°$, the drag coefficient shows minor sensitivity to $l/c$, but the ground effect appears to be more substantial than that of lift. Between $120° < \beta < 150°$, the drag coefficient variations with $l/c$ do not follow a consistent pattern, which is attributed to the sting placement. For $\beta \geq 150°$, the drag coefficient is reduced with decreasing $l/c$, with the maximum reduction due to ground effect observed at $\beta = 180°$.

The time-averaged side force coefficient is presented in Fig. 5.3b. The side force coefficient follows a sinusoidal shape with equivalent opposingly signed peaks at $\beta = 45°$ and 135°, matching critical side force coefficients for square solar panel geometries [43, 110, 111]. At $\beta = 0°$ and 180°, the side force coefficient is approximately zero due to spanwise symmetry, while at $\beta = 90°$, zero effective angle of attack leads to a zero side force coefficient. The ground effect manifests in an increase in the side force coefficient magnitude between $30° \leq \beta \leq 80°$, with peak side force coefficient increasing from 0.28 to 0.34 (21%) as $l/c$ is decreased to 0.1. For $\beta > 90°$, the side loading does not change appreciably with $l/c$.

Total force magnitude coefficient, comprising contributions from lift, drag, and side force components, is presented in Fig. 5.3c. Notably, the shape of the total force with respect to $\beta$ is positively correlated with lift and drag coefficients due to the relatively low magnitude of the side force. Since the lift force is the largest contributing force component to the total force, particularly as $\beta \to 0°$ or 180°, the same trends observed in the lift coefficient with respect to gap ratio and yaw angle are also observed in the total force coefficient, that is the yaw angle acts to modify effects of the gap ratio on loading. In free flight, equivalent peak force coefficients ($1.21 \pm 0.02$) are observed at $\beta = 0°$ and 180°. As the gap ratio decreases, total force coefficient increases by 7% at $\beta = 0°$ and decreases by 24% at $\beta = 180°$ relative to free flight levels.

Force coefficients are compared to both side-slip and yawed configurations in Fig. 5.4. Side-slip lift and drag coefficients reported in previous studies are presented in Figs. 5.4a and 5.4b, respectively. To facilitate the comparison to present results, force coefficients are normalized by corresponding values at $\beta = 0°$. For $\beta < 10°$, the current results show good agreement to side-slip results since variations in effective angle of attack are negligible. With further increase in $\beta$, the effective angle is significantly altered, and analytical estimates of lift and drag coefficients begin to deviate from the present results, though the experimental results show better agreement. In particular, the rate of change of the normalized lift and drag coefficients with $\beta$ is comparable between the present work and experimental investigations on flat plates in side-slip.

Present force results are compared to previous experimental results at $l/c \approx 0.5$ [25, 26] in Figs. 5.4d–5.4f. In general, the present results show good agreement with previously reported force coefficients. However, some deviations are noteworthy and can be traced to features of model geometry and/or setup. Lift and drag coefficients reported by Mohapatra [25] are lower than present results as $\beta \to 0°$ or 180°, however, as $\beta \to 90°$, the drag coefficient is higher. This is

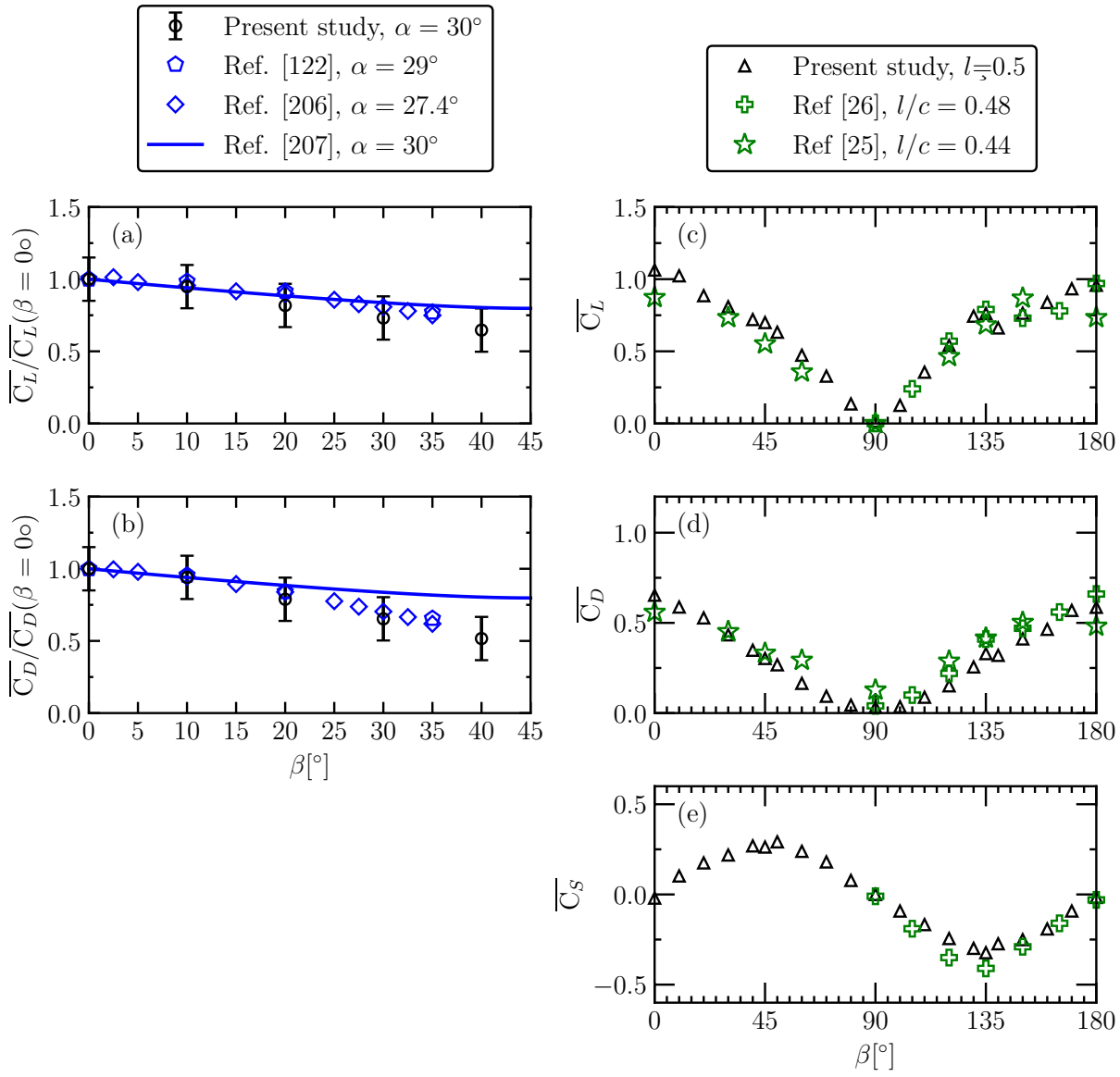


**Figure 5.4:** Comparison of (a) lift and (b) drag coefficients normalized by values at $\beta = 0°$ for flat plates in free flight side-slip. Yawed flat plate (c) Lift magnitude, (d) drag, and (e) side force, are compared with previous results at $l/c \approx 0.5$. Reproduced data are for AR = 1, $\alpha = 30°$, and $l/c \geq 1$, unless otherwise specified. Experimental data are shown using markers, while analytical estimates are shown using solid lines. Experimental data are sourced from Shields & Mohseni [122], Hartlin [206], Merarda *et al.* [26], and Mohapatra [25]. Analytical force estimates are reproduced from DeVoria & Mohseni [207]. Uncertainty for the present results is accommodated by marker size unless otherwise indicated by error bars.

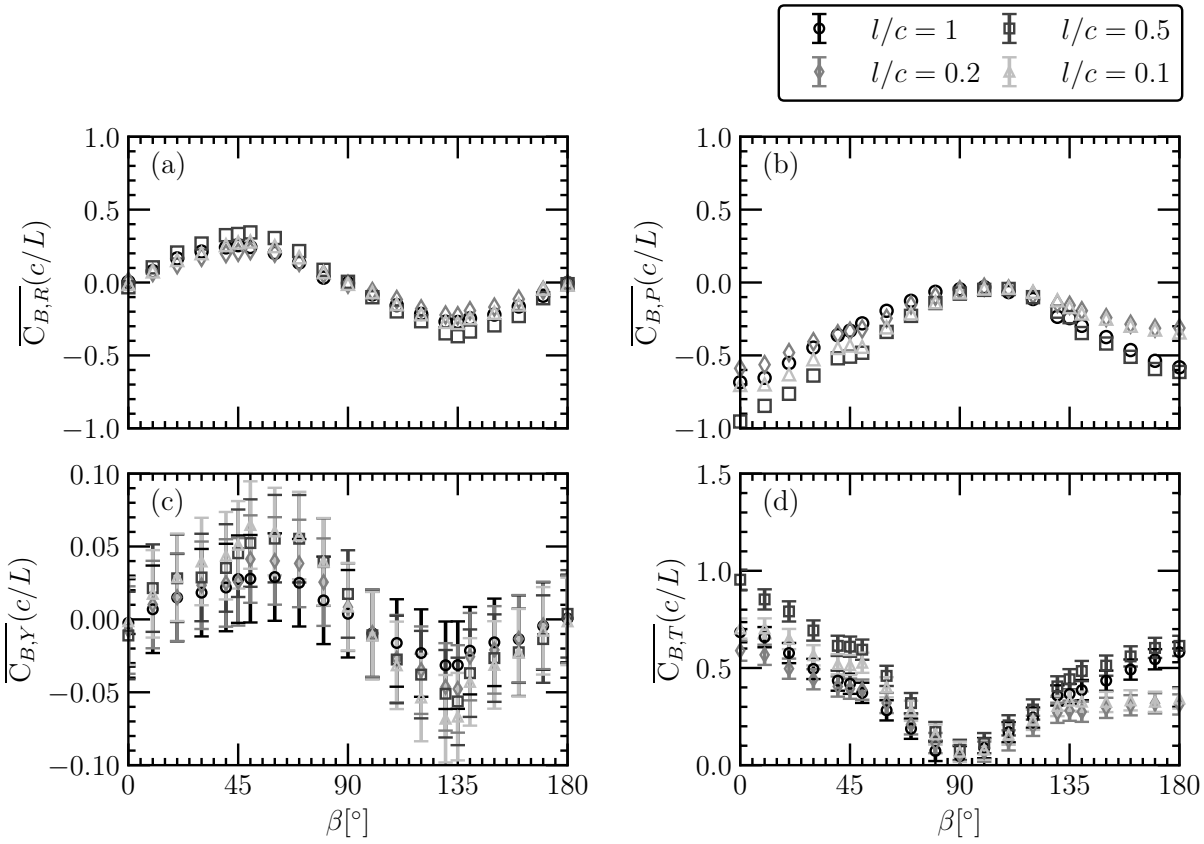


**Figure 5.5:** Time-averaged (a) roll, (b) pitch, (c) yaw, and (d) total moment coefficients at the sting base for all gap ratios tested. For roll and pitch moment coefficients, uncertainty is accommodated by the marker size

attributed to the use of a scaled photovoltaic model with fin-like support structures on the ground facing side of the panel in Ref. [25]. Underside fins are expected to disrupt the high lift and drag generation due to leading-edge shear layer attachment as $\beta \to 0°$ or 180°, and lead to higher drag due to the increase in surface area as $\beta \to 90°$. Further, the lift coefficient reported by Merarda *et al.* [26] at $\beta = 90°$ is approximately 0.16, suggesting that sting effect was not compensated for in their measurements, as done herein. The sting effect also appears to manifest in the results reported by Merarda *et al.* [26] as a local maximum in the lift coefficient near $\beta = 140°$(cf. Fig. 5.2b).

All time-averaged base and total moment coefficients scaled by the normalized sting length, $L/c$ are presented in Fig. 5.5. The base roll moment coefficient (Fig. 5.5a) follows the same trends as the side force with peak values at $\beta = 45°$ and 135°. Notably, the scaled base roll moment coefficient remains constant with changes in the gap ratio. Based on these results, base roll moments can be decreased by about 50% by decreasing $l/c$ from 1 to 0.1, however, this is accompanied by the increase in lift and drag for $\beta < 90°$ (Figs. 5.2a and 5.3a). The base pitch moment coefficient (Fig. 5.5b) is negatively correlated with the lift and drag force coefficients. For $\beta < 90°$, the pitch moment coefficient magnitudes generally increase with decreasing gap ratio, exhibiting an increase in the peak values of approximately 12% at $\beta = 0°$ between $l/c = 1$ and

0.2. For $\beta > 120°$, base pitch moment coefficient magnitudes decrease with decreasing gap ratio. With increasing $\beta$, differences between free flight and $l/c = 0.1$ pitch moment coefficient values increase, which matches the observed changes in lift and drag coefficient. Notably, a decrease of 41% relative to free flight levels is observed at $\beta = 180°$. Although the expected sinusoidal variation with respect to $\beta$ can be observed in the yaw moment profiles presented in Fig. 5.5c, effects of $\beta$ and $l/c$ on the yaw moment coefficient are too small to be resolved.

For a given $l/c$, the total moment (Fig. 5.5d) closely follows total force coefficient magnitude and the pitch moment: as $\beta \to 90°$ the moment coefficient approaches zero. Notably, the total moment coefficient at $\beta = 180°$ is 15% lower compared to $\beta = 0°$ in free flight, with the source of this difference stemming from the pitch moment coefficient. For the same yaw angles, lift coefficient difference is approximately 2.5%, while drag coefficient differs by 5%. The higher difference in the pitch and total moment coefficients are therefore attributed to variations in the center-of-pressure between the yaw angle extrema due to the sting placement switch from pressure to the suction side at $\beta = 90°$. Gap ratio related trends in the total moment coefficient match those of lift, drag, and pitch moment coefficients. The total moment coefficient increased by 12% between $l/c = 1$ and 0.2, while a decrease of 44% is observed for $\beta = 180°$ between $l/c = 1$ and 0.1.

## 5.4 Suction Side Surface Flow Topology

To gain an understanding of the physical mechanisms underpinning the aerodynamic loading changes with $\beta$ and $l/c$, surface oil flow visualization snapshots over the suction side are analyzed for a subset of loading test cases (Table 4.1). Still visualization images presented in this section are supplemented by videos, which help better highlight certain surface flow features. A surface attached coordinate system is used for discussion of the results with $\zeta$ and $\eta$ defining the chordwise and spanwise coordinates, respectively. Figure 5.6 presents visualization after at least two hours of run time for $\beta = 0°$, 30°, 45°, and 60° for $l/c = 0.1$ and 1. For $\beta = 0°$ at $l/c = 1$, three critical points can be identified: two foci located along $\zeta/c \approx 0.2$ and one node along the midspan position at $\zeta/c \approx -0.45$. At the node, reverse flow is notable in supplemental videos, while flow toward the trailing edge can also be seen, suggesting reattachment of the leading-edge shear layer as observed in previous studies through quantitative flow measurements [207]. As the oil moves toward the leading-edge due to reverse flow, interaction with flow associated with tip vortex formation creates two foci, each resembling stall cells [121], positioned symmetrically about the midspan. Tip vortices develop downstream along the plate edges ($\eta/c = \pm 0.5$) as indicated by the pooling of oil. At $\beta = 0°$, the surface flow topology matches previously reported surface streamline patterns [207]. The observed shear layer reattachment is credited for the peak lift and drag coefficients attained in this orientation (Figs. 5.2a and 5.3a).

At $\beta = 30°$ and 45°, only one focus point can be identified, which moves inboard relative to $\beta = 0°$. The extent of oil pooling at the upstream edge ($\eta/c = -0.5$) extends toward the middle of the plate, while less oil collects along the downstream edge, suggesting the upstream tip vortex moves inboard, while the downstream tip vortex moves farther from plate surface after formation. Flow toward the upstream edge tip and the leading-edge can be observed along the freestream

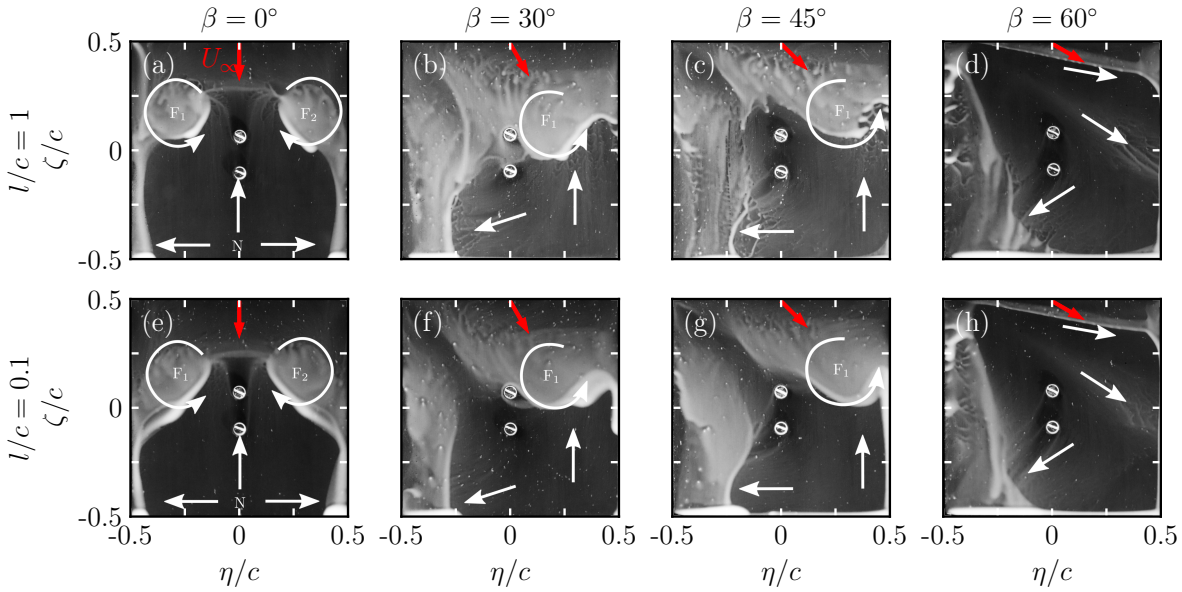


**Figure 5.6:** Surface oil on the suction side for $\beta < 90°$. Red and white arrows indicate freestream and oil flow directions, respectively. $\zeta/c = -0.5$ corresponds to the model edge closest to the ground.

direction, however, a node is not observed. For $\beta \leq 45°$, the results suggest that the upstream tip vortex trajectory moves inboard relative to $\beta = 0°$, reducing the available space for development of the leading-edge shear layer, accompanied by a decrease in lift and drag relative to those at $\beta = 0°$ (Figs. 5.2a and 5.3a).

At $\beta = 60°$, no critical points nor reverse flow can be observed on the suction side. Along $\eta/c = -0.5$ oil pooling is present, marking the formation and evolution of a tip vortex over the plate, which is less pronounced compared to $\beta = 30°$ and 45°. Along $\zeta/c = 0.5$, oil patterns reveal a distinct boundary that is at an angle to $\zeta/c = 0.5$, while a more smeared pattern is identifiable between this boundary and the plate edge. This flow pattern is characteristic of primary and secondary flow separation on a non-slender delta wing due to formation of edge vortices [177, 208, 209]. Absence of a recirculation region over the plate at this yaw angle, as suggested by the lack of foci (Fig. 5.6d), critical for generation of aerodynamic loads, results in a significant decrease in lift and drag coefficients. It is of interest to note that side force and base roll moment coefficients observed for $\beta = 60°$ in free flight are equivalent to values at $\beta = 30°$ (Figs. 5.3b and 5.5a), despite notable changes in the suction side flow topology seen in Fig. 5.6.

As the gap ratio is decreased to 0.1, no notable changes in the suction side flow development are observed in the surface oil flow visualizations for $\beta < 90°$ (Fig. 5.6). However, lift magnitude, drag, and side force coefficients show a notable increase with decreasing gap ratio (Figs. 5.2a, 5.3a, and 5.3b). Since the suction side flow appears to be largely insensitive to $l/c$, the changes in aerodynamic loads are attributed to changes in the pressure side flow. The ram effect [154] is expected to lead to increased pressure magnitudes on the ground facing side resulting in increased aerodynamic loads for $\beta < 90°$, where the effective angle is positive.

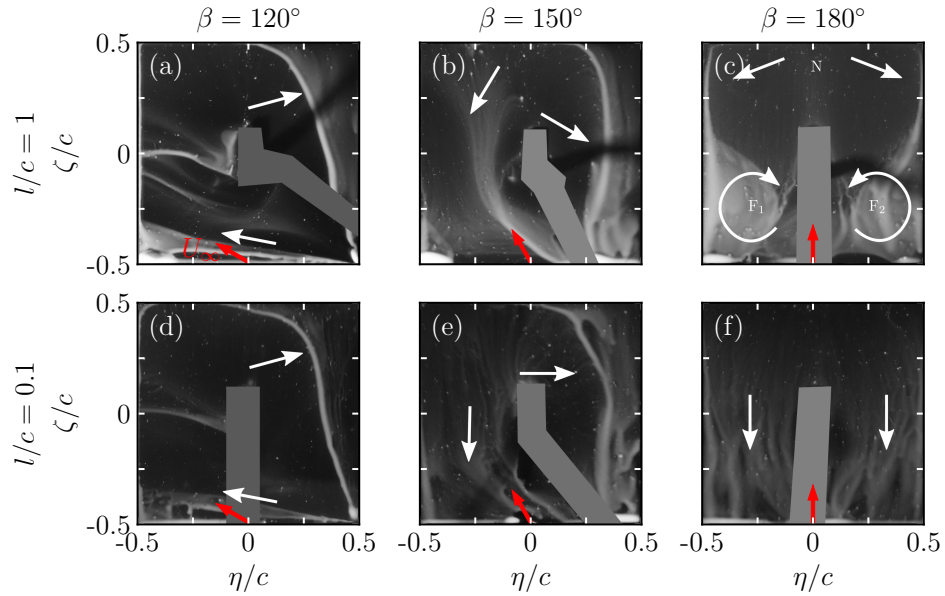


**Figure 5.7:** Surface oil on the suction side for $\beta > 90°$. Red and white arrows indicate freestream and oil flow directions, respectively. $\zeta/c = -0.5$ corresponds to the model edge closest to the ground.

Suction side surface oil flow visualizations for $\beta = 120°$, 150°, and 180° in free flight ($l/c = 1$) and ground effect ($l/c = 0.1$) are shown in Fig. 5.7. At $\beta = 120°$ under free flight conditions, the flow topology is largely similar to that of $\beta = 60°$, and the relatively minor differences in lift and drag coefficients are attributed to the sting effect. At $\beta = 150°$, a focus point similar to that of $\beta = 30°$ is not observed, however, equivalent loading values are measured for these cases. At $\beta = 30°$, the focal point is located close to the midspan near the sting mounting location (Fig. 5.6b), which should also be the case for $\beta = 150°$ under free flight conditions given the equivalent flow configurations. The placement of the sting on the suction side at $\beta = 150°$ is expected to disturb the local oil flow near the critical point. In contrast, at $\beta = 180°$, the flow topology is equivalent to that of $\beta = 0°$ with matching peak loading coefficient values.

As the gap ratio is decreased to 0.1, the suction flow topology at $\beta = 120°$ remains unchanged, in agreement with the insensitivity of aerodynamic loading coefficients to gap ratio for this yaw angle. For $\beta = 150°$, a decrease in gap ratio leads to less distinct surface oil flow patterns throughout the plate surface, particularly in the reversed flow region observed for $\eta/c < 0$. The most notable changes in the surface oil flow patterns with $l/c$ are observed at $\beta = 180°$. Specifically, all critical points disappear as the gap ratio is decreased from free flight to $l/c = 0.1$, and average oil motion is along the streamwise direction toward the leading-edge, suggesting fully separated flow over the plate. At $l/c = 0.1$, the surface flow topology at $\beta = 180°$ is similar to that observed for $\eta/c < 0$ at $\beta = 150°$, which points to partially stalled flow over the suction side for $\beta = 150°$. For both $\beta = 150°$ and 180°, the results suggest that the ground effect leads to the formation of a larger separated flow area on the suction side (either fully stalled at $\beta = 180°$, or partially at $\beta = 150°$) leading to a decrease in aerodynamic loads seen in Figs. 5.2a, 5.3a, 5.3c, 5.5b, and 5.5d.

## 5.5 Wake Flow Development Near the Trailing Edge

The preceding discussion of suction side surface flow visualizations provided qualitative insights into the surface flow topology and helped explain the main trends observed in the aerodynamic loading. To assess the effects of yaw angle and gap ratio on the flow development, cross-plane flow measurements were performed with SPIV (Table 4.1). The results are presented and analyzed in this section, focusing on the effects of yaw angle and gap ratio.

Figure 5.8 presents time-averaged streamwise velocity fields normalized by the freestream velocity for $\beta = 0°$, $30°$, $45°$, and $60°$ for tested gap ratio extrema. The presented streamline patterns clearly identify two tip vortices, whose footprints were inferred earlier in surface flow visualization images. As expected, a notable velocity deficit region is produced by the plate. When $\beta$ is increased, the velocity deficit progressively diminishes, correlating with the decrease in the size of the separated flow region seen in surface flow visualizations (Fig. 5.6) and the associated decrease in drag coefficient (Fig. 5.3a). In ground effect ($l/c = 0.1$), the average velocity deficit in the wake increases for a given $\beta$, which agrees with the observed increase in drag coefficient (Fig. 5.3a).

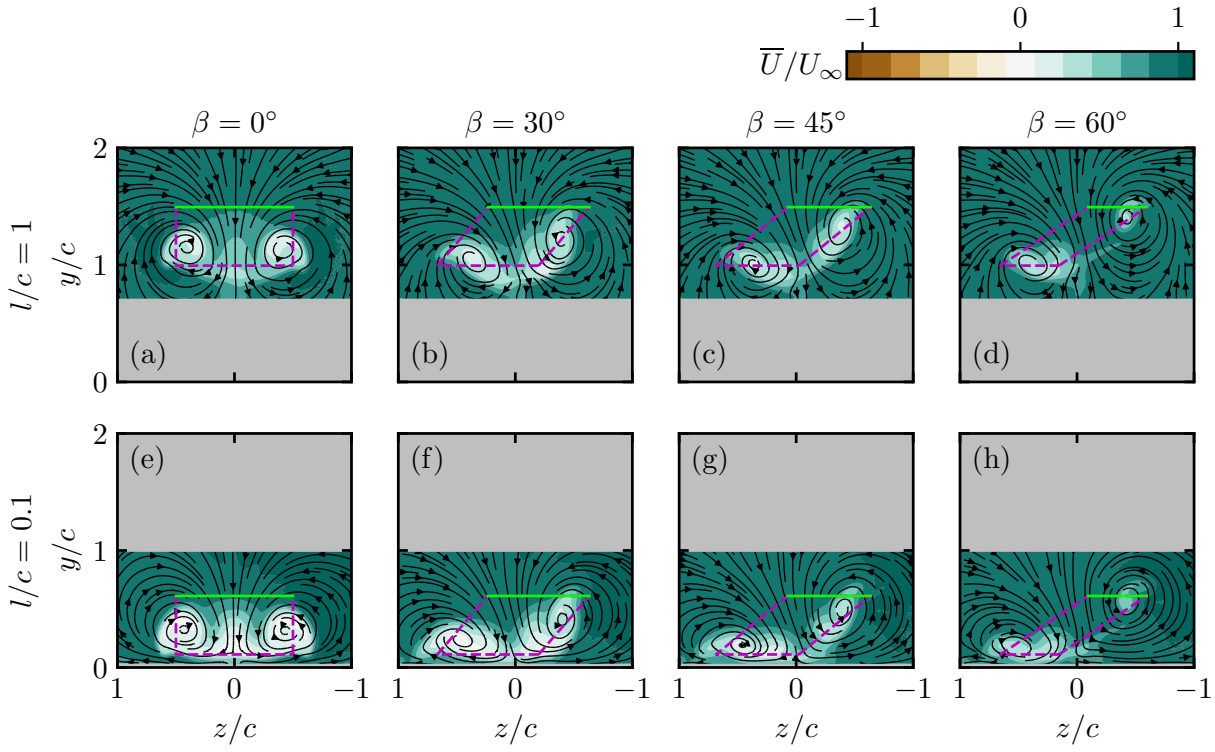


**Figure 5.8:** Normalized streamwise velocity contours overlaid with planar streamlines at $0.2c$ downstream of the model for $\beta < 90°$ at $l/c = 1$ (top row) and $l/c = 0.1$ (bottom row). Projected plate position is indicated by the dashed lines. Leading-edge for $\beta = 0°$ is indicated by the green solid line.

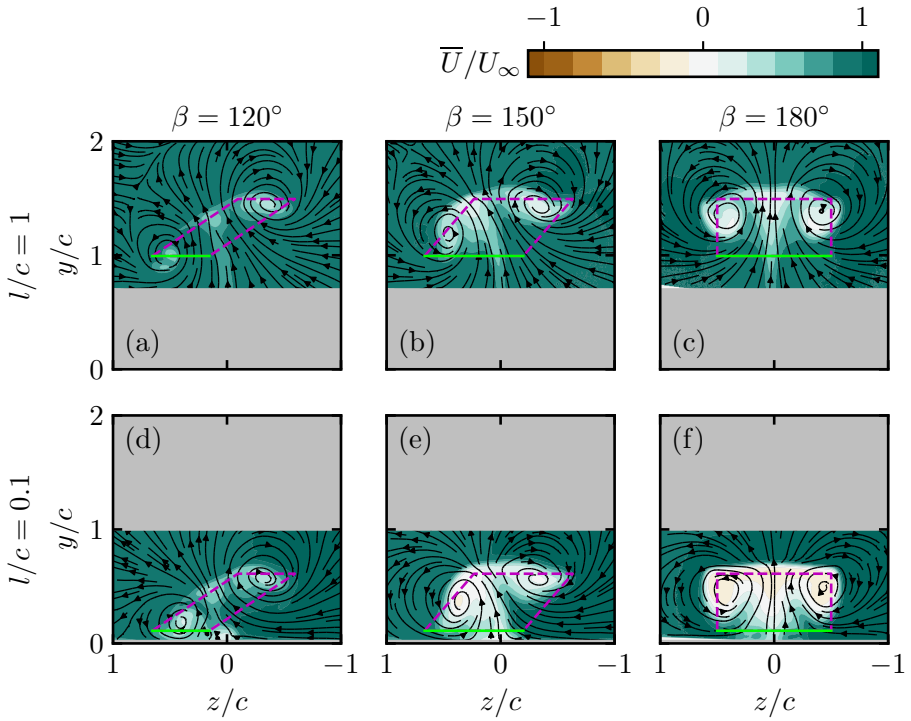


**Figure 5.9:** Normalized streamwise velocity contours overlaid with planar streamlines at $0.2c$ downstream of the model for $\beta > 90°$ at $l/c = 1$ (top row) and $l/c = 0.1$ (bottom row). Projected plate position is indicated by the dashed lines. Leading-edge for $\beta = 180°$ is indicated by the green solid line.

Time-averaged normalized streamwise velocity fields for $\beta = 120°$, 150°, and 180° at $l/c = 1$ and 0.1 are presented in Fig. 5.9. Under free flight conditions ($l/c = 1$), similar results are seen in Fig. 5.8 and Fig. 5.9 for the symmetric yaw angle pairs about $\beta = 90°$ (i.e., $\beta = 0°$ and 180°; $\beta = 30°$ and 150°), with the exception of the modified velocity deficit due to the sting near $z/c = 0$. However, on the average, the ground effect on the wake flow is more notable for $\beta > 90°$ cases, and becomes more pronounced at higher yaw angles. While at $\beta = 120°$ a marginal increase in the velocity deficit is observed for $l/c = 0.1$ (Fig. 5.9d), a notably stronger decrease in streamwise velocity is seen at $\beta = 150°$ (Fig. 5.9e) with decreasing $l/c$. At this yaw angle, negative streamwise velocities are observed with the near wake, supporting the inferred partial stall from the surface oil flow visualization (Fig. 5.7) and the associated decrease in lift and drag coefficients (Figs. 5.2a and 5.3a). At $\beta = 180°$, the greatest decrease in near wake streamwise velocity is observed as $l/c$ decreases, which is in agreement with the stalled flow observed in the flow visualization images (Fig. 5.7f). The onset of stall as $l/c$ decreases is further substantiated by the observed decrease in lift and drag at $\beta = 180°$ (Figs. 5.2a and 5.3a).

As tip vortices are critical for relatively high aerodynamic loading of low AR flat plates [19, 23], the effect of yaw angle on the tip vortex topology is characterized by analyzing streamwise vorticity fields for both free flight and ground effect conditions. Time-averaged normalized streamwise vorticity contours for $\beta = 0°$, 30°, 45°, and 60° under free flight ($l/c = 1$) and ground

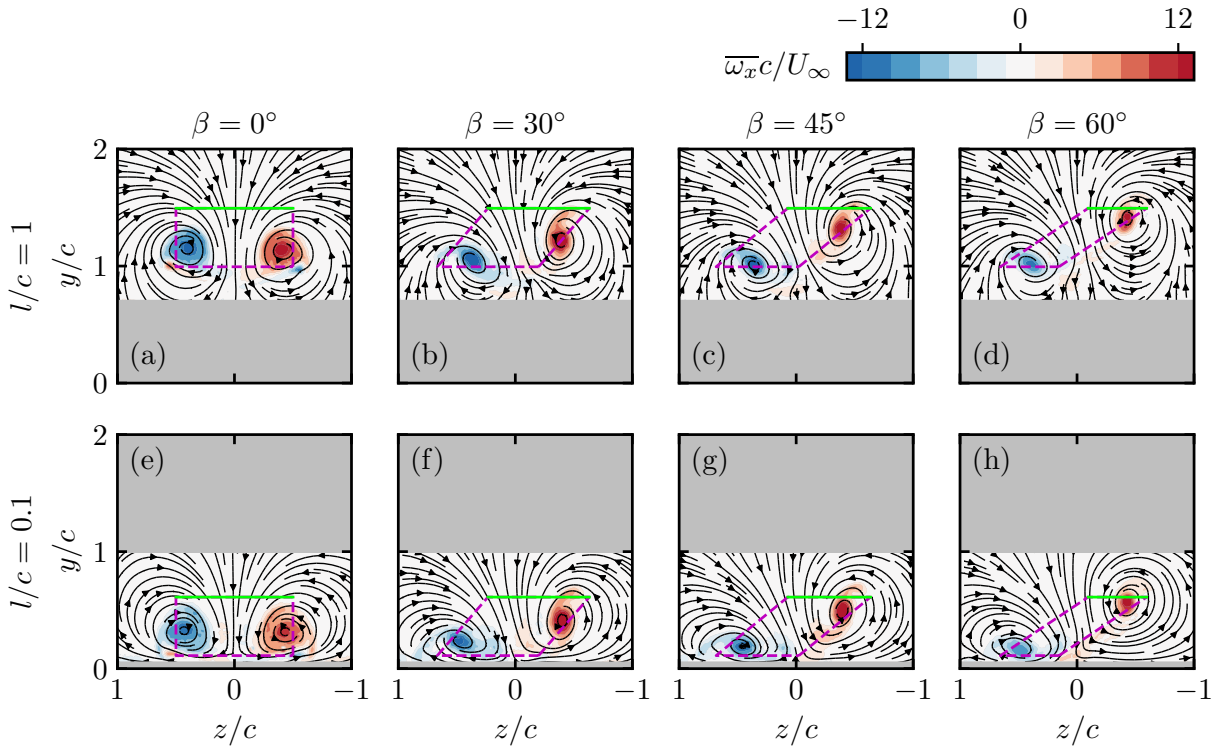


**Figure 5.10:** Normalized streamwise vorticity contours overlaid with planar streamlines at $0.2c$ downstream of the model for $\beta < 90°$ at $l/c = 1$ (top row) and $l/c = 0.1$ (bottom row). Projected plate position is indicated by the dashed lines. Leading-edge for $\beta = 0°$ is indicated by the green solid line.

effect ($l/c = 0.1$) conditions are displayed in Fig. 5.10. As expected, two vortices with opposingly signed vorticity can be identified for all cases. When $\beta$ is increased, the positive tip vortex moves upward diagonally, while the negative tip vortex is repositioned more inboard along a constant $y/c$ level. When $l/c$ is decreased, a similar streamwise vorticity topology is observed for all $\beta < 90°$ cases in agreement with the earlier presented surface flow visualization results (Fig. 5.6). For these cases, notable changes in the vorticity levels with $\beta$ and $l/c$ are not observed in Fig. 5.10.

Figure 5.11 presents time-averaged normalized vorticity fields for $\beta = 120°$, $150°$, and $180°$ for free flight ($l/c = 1$) and ground effect ($l/c = 0.1$) conditions. As expected from the normalized streamwise velocity results (Figs. 5.8 and 5.9), symmetric yaw angle pairs about $\beta = 90°$ produce a similar topology when considering the disturbance of the suction side flow by the sting under free flight conditions. At $\beta = 120°$, the streamwise vorticity fields do not differ appreciably between free flight and ground effect conditions, while at $\beta = 150°$ and $180°$, a significant decrease in the average vorticity levels can be observed, supporting the preceding observations of stall onset for these cases. The position variation of the vortex pair are similar between free flight and ground effect cases as $\beta$ increases, with the positive vortex moving upward diagonally toward the projected trailing edge, while the motion of the negative vortex is mainly lateral in the outboard direction.

To clarify the flow topology observed in the flow visualization and cross-plane SPIV results, conceptual sketches of the tip vortices at $l/c = 1$ are shown in Fig. 5.12. The results are grouped

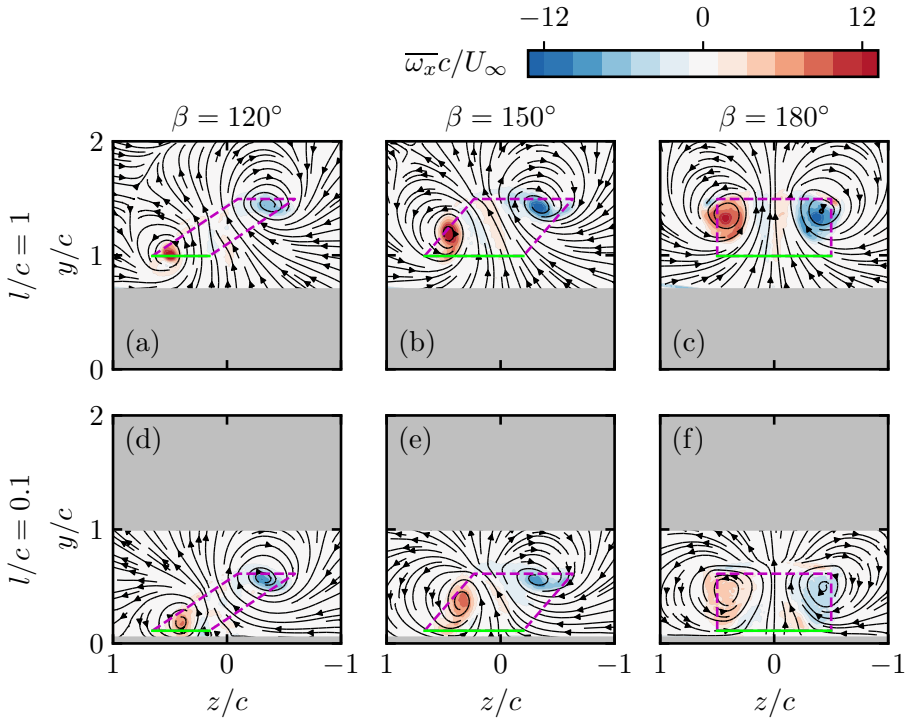


**Figure 5.11:** Normalized streamwise vorticity contours overlaid with planar streamlines at $0.2c$ downstream of the model for $\beta > 90°$ at $l/c = 1$ (top row) and $l/c = 0.1$ (bottom row). Projected plate position is indicated by the dashed lines. Leading-edge for $\beta = 180°$ is indicated by the green solid line.

based $\beta$ levels with equivalent flow topologies and ignores sting placement for clarity. At $\beta = 0°$ or 180°, the tip vortices are symmetric about the midspan position and develops downstream aligned with the plate tips and trailing edge. For $30° \leq \beta \leq 45°$ or $\beta = 150°$, the topology is asymmetric about the midspan and the negative tip vortex develops along the plate, while the positive tip vortex departs the plate at an chordwise position closer to the leading edge. At $\beta = 60°$ or 120°, the tip vortex topology closely resembles that of a tilted delta wing. These topological sketches are representative of the flow both in and out of ground effect for $\beta \leq 60°$. However, for $\beta \geq 120°$, the sketches are only representative of $l/c = 1$ configurations as the closer ground proximity results in less discernible surface oil patterns over the plate.

The qualitative descriptions in the tip vortex characteristics in the preceding discussion are quantified by their circulation and centre positions. Circulation estimates, used as a measure of vortex strength, are facilitated through the use of $\lambda_2$ criterion [189]. The tip vortex boundary was identified as the largest continuous closed contour of $\lambda_2$ that were verified to contain the detected tip vortex cores. Circulation was computed via a line integral of in-plane velocity around the closed contour. The selected $\lambda_2$ level used for circulation estimates was determined based on the convergence of computed circulation for varying $\lambda_2$ and a convergence criteria of 3%. Vortex centers were identified using the $\Gamma_1$ method [192]. The maximum uncertainty accounting for

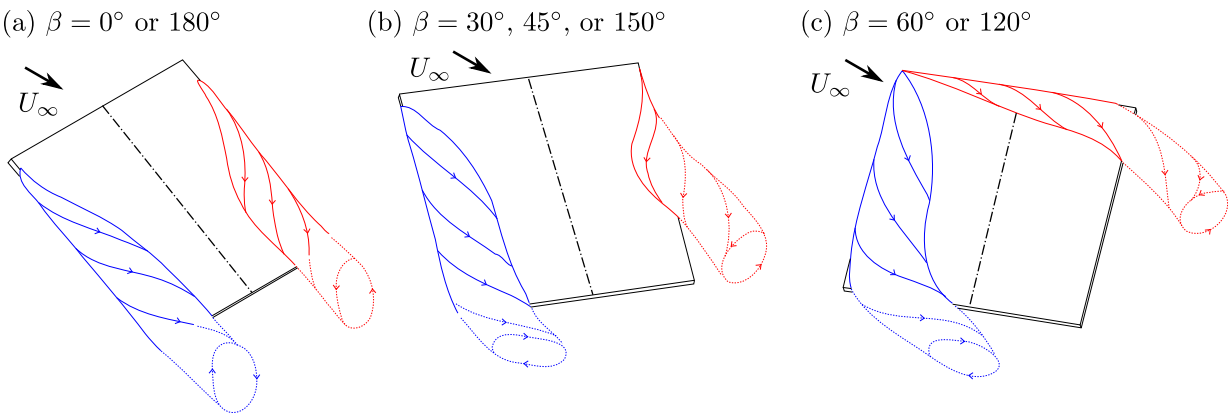


**Figure 5.12:** Conceptual sketches of tip vortex topology on the suctions side for (a) $\beta = 0°$ or 180°, (b) $\beta = 30°$, 45°, or 150°, and (c) $\beta = 60°$ or 120°. Solid lines mark footprints of tip vortices observed in flow visualization results, while dashed lines indicate flow development inferred from both flow visualization and SPIV results. Sting placement is ignored for clarity. The midspan of the plate at $\beta = 0°$ is indicated by a dash-dot line.

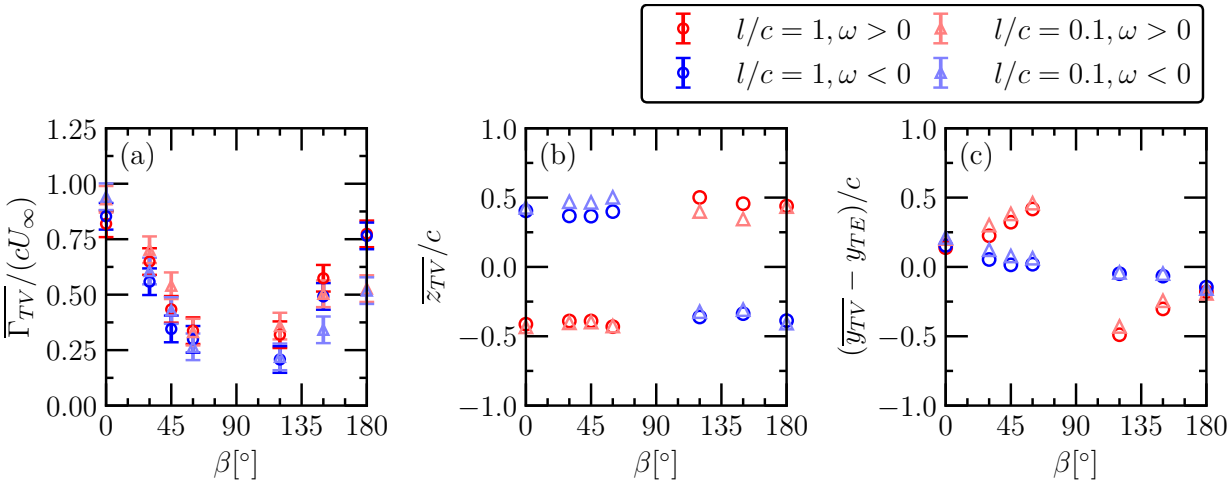


**Figure 5.13:** (a) Normalized tip vortex circulations, (b) vortex core spanwise positions and (c) wall normal distance of the vortex core relative to the trailing edge. Tip vortex circulation is estimated based on $\lambda_2$ criterion [189] and core locations are determined using the $\Gamma_1$ method [192]. Uncertainty in the vortex core positions is accommodated by the marker size unless otherwise indicated by error bars.

measurement and methodological uncertainty is $\overline{\Gamma_{TV}}/(cU_\infty) = \pm 0.06$ for circulation estimates and $\pm 0.04c$ for vortex positions.

Time-averaged normalized tip vortex circulation estimates, $\overline{\Gamma_{TV}}/(cU_\infty)$, are presented in Fig. 5.13a. As $\beta \to 90°$ normalized tip vortex circulation of both vortices decreases and tends toward zero in line with the lift and drag coefficients results (Figs. 5.2a and 5.3a). Notably, the circulations for $\beta > 90°$ are lower than their corresponding $\beta$ pairs under free flight conditions, which is attributed to the disruption to the suction side flow by the sting placement for these cases.

For $\beta < 90°$, as the gap ratio is decreased from $l/c = 1$ to 0.1, there is an appreciable increase in in the normalized tip vortex circulation at the measurement plane, which is consistent with the ram effect phenomenon [154] and the corresponding increase in lift (Fig. 5.2a) and drag (Fig. 5.3a). The exception to this is the normalized circulation at $\beta = 60°$, which appears to be insensitive to $l/c$, despite an increase in loading. The earlier noted absence of critical points, and therefore a recirculation region, over the suction side at this $\beta$ suggests that the tip vortices do not play a significant role in the loading generation at $\beta = 60°$. A similar observation is made for $\beta = 120°$ when the gap ratio is decreased, however, as the ram effect does not manifest for $\beta > 90$, the loading is also insensitive to gap ratio variations. At $\beta = 150°$ and 180°, the tip vortex circulations decrease with closer ground proximity in agreement with the observed stall behaviour at these yaw angles. Notably, the relative decrease in tip vortex circulation is greatest at $\beta = 180°$, where separated flow over the full extent of the plate is observed from the surface flow visualizations (Fig. 5.7f). For all cases except $\beta = 0°$ and 180°, the negative tip vortices have moderately lower circulations compared to their positive counterparts. When $\beta \neq 0°$ and 180°, the negative tip vortex convects a greater distance along the plate surface in comparison to the positive tip vortex as inferred from the surface flow visualizations (Figs. 5.6 and 5.7), leading to increased entrainment of lower momentum flow (Figs. 5.8 and 5.9) and reducing the vortex circulation.

Time-averaged normalized lateral vortex core position, $\overline{z_{TV}}/c$ is presented in Fig. 5.13b. The lateral positions are largely insensitive to changes in $\beta$ at the measurement plane. A minor ground effect on lateral vortex core position is observed for the vortex closer to the ground as $l/c$ is decreased for a given $\beta$ value. As $l/c$ is decreased, the vortex closer to the ground is shifted outboard for $0° < \beta < 90°$, while being repositioned inboard for $90° < \beta < 180°$, consistent with the expected induced effects by an image vortex pair reflected about the ground plane. In contrast, the vortex farther away from the ground is observed to be insensitive to $l/c$ variations, in agreement with the expected decrease in induced velocity from the ground-bound vortex pair.

Figure 5.13c presents the time-averaged normalized mean wall normal tip vortex positions, $\overline{y_{TV}}/c$ relative to that of the trailing edge ($y_{TE}$). The variations in wall normal positions with $\beta$ shows a notable change in wall normal position of the positive vortex, while the negative vortex remains close to trailing edge as expected from the vorticity fields. Based on the circulation difference in the tip vortex pair, mutual induction is expected to lead to relative motion of the vortex pair in a counter clockwise sense for $\beta < 90°$ and clockwise sense for $\beta > 90°$. Thus, the expected effect is aligned with the observed increase in the vertical separation of the positive and negative vortex pair cores in Fig. 5.13c, particularly when coupled with the earlier departure from the suction surface of the positive vortex based on the surface flow visualization results (Figs. 5.6 and 5.7). On the other hand, the ground effect on the vertical vortex core position in negligible.

## 5.6 Concluding Remarks

The investigation presented in this chapter examined aerodynamics of an inclined square flat plate in ground effect at different yaw angles. The experiments considered a flat plate at a fixed pitch angle of 30°, corresponding to the maximum loads at zero yaw based on results in Chapter 4. Direct force measurements revealed variation in ground effect related on loading with yaw angle

$\beta$ in the total force and base moment coefficients. For $\beta < 90°$, loading is greater in ground effect relative to free flight conditions. For $90° \leq \beta \leq 120°$, aerodynamic loading was mainly insensitive to $l/c$ variations, while a decrease was observed for $150° \leq \beta \leq 180°$. Notably, the sting effect confounded the ground effect related total force changes for $120° \leq \beta \leq 150°$ verified by force measurements with a top side sting placement. As the gap ratio decreased, an increase of 7% and 3% in total force and moment coefficients, respectively, were observed for $\beta = 0°$. Comparatively, at $\beta = 180°$ a decrease of 24% and 44% was observed for total force and moment coefficients, respectively, as $l/c$ was decreased from 1 to 0.1.

Flow measurements were used to elucidate the physical mechanisms responsible for aerodynamic loading variations with $\beta$ and $l/c$. For $\beta < 90°$, as the gap ratio was decreased, changes to the suction side surface flow and tip vortex topology were minimal, while an increase in loading was observed. These loading variations were attributed to the ram effect, expected to occur for $\beta < 90°$. Between $90° \leq \beta \leq 120°$, a marked change in the loading was not observed as $l/c$ varied, which coincided with the lack of changes to the suction side surface and streamwise near wake flow topology. For $\beta \geq 150°$, onset of stalled flow development over the plate and the lack of ram effect resulted in a decrease in the overall loading with closer ground proximity.

In the context of photovoltaic installations, the results reveal that the yaw angle is an important consideration for square panel arrangements, particularly for $l/c < 0.5$, as the changes in aerodynamic loads with gap ratio are dependent on the incoming wind direction, which can vary between $0° \leq \beta \leq 180°$. Based on the investigated angle of attack, the current results are applicable to latitudes close to ±40° (i.e., central North America, southern Europe, northern regions of Asia, southern regions of South America, and Australia), thus being of relevance to regions with a major share of solar energy production. The results suggests that the variability of wind direction and ground clearance at a particular installation site of both isolated and perimeter photovoltaic requires careful assessment for cost-effective and targeted design of support structures.

# Chapter 6

# Aerodynamics of an Impulsively Yawed Flat Plate in Close Ground Proximity

*Chapters 4 and 5 focused on steady state effects of aspect ratio, ground proximity, angle of attack, and wind direction on the flow development and loading on finite-span inclined flat plates. However, solar panel installations are ground-mounted in open environments, subjecting them to gusts, which may result in sudden wind direction variations. This chapter details an experimental investigation carried out to gain insight into the transient aerodynamic effects of a sudden wind direction change on a square flat plate in close ground proximity using lift and wake flow measurements. A transient change in wind direction is modelled by a model rotation in steady incoming flow. Notable hysteresis is observed in the lift coefficient depending on the direction of model rotation, which is found to originate from differences in tip vortex development. The lift coefficient is found to exhibit a mild overshoot of 10% compared to steady state values.*

Parts of this chapter have been adapted from

Pieris, S., Yarusevych, S. V., & Peterson, S. D. 2023 Effect of dynamic wind direction changes on aerodynamics of a square inclined flat plate in ground effect. In *AIAA Aviat. 2023 Forum*, San Diego, CA. DOI.

Pieris, S., Yarusevych, S., & Peterson, S. D. Transient lift coefficient and tip vortex development of an isolated solar panel subjected to a sudden wind direction change. *J. Wind Eng.*, [**In Review**: INDAER-D-23-00660].

## 6.1 Introduction

To maximize incoming solar irradiance, solar panels are typically installed in open terrain and are subjected to effects of wind direction variations. Wind direction (i.e., yaw angle) may vary substantially due to large scale weather patterns [105]. Previous investigations have been limited to static yaw configurations in their examination of aerodynamic loading. Peak lift and drag coefficients are observed for $\beta = 0°$, representing headwind conditions when $\alpha > 0$, and also at 180° under tailwind conditions, following typical aerodynamic conventions [25, 26, 31]. Expectedly, the side-force coefficient is zero at $\beta = 0°$ and sinusoidal with a period of 180° [26]. The base roll and yaw moment coefficients are positively correlated with the side force, while the base pitch moment is negatively correlated and is the most significant contributor to the overall moment coefficient [26]. The incomplete understanding of the connection between loading and flow was addressed in Chapter 5, using a square aspect ratio plate at $\alpha = 30°$ and $\mathrm{Re}_c = 50\,000$. The results show that as $\beta \to 90°$, the tip vortex circulation decreases, reducing the total force and moment coefficients as the leading-edge shear layer reattachment responsible for load generation is disrupted, highlighting the key role that the tip vortices play in steady load generation of square flat plates.

Open environments expose photovoltaic installations to sudden changes in wind directions during extreme weather events, causing structural damage and increasing costs. A sudden change in yaw angle of an inclined flat plate in close ground proximity has not yet been investigated at scales relevant to photovoltaic installations. Such an event is expected to cause notable transient tip vortex characteristics and modify the aerodynamic loads on low AR inclined plates. This motivates the work carried out in this chapter. The main objective is to experimentally characterize the aerodynamic loading and relate this to driving flow features during a sudden change in yaw angle.

## 6.2 Experiment Details

Experiments were conducted in a recirculating wind tunnel in the Fluid Mechanics Research Laboratory at the University of Waterloo. The tunnel has a 9:1 contraction ratio and a settling chamber consisting of a honeycomb insert and five mesh screens installed upstream of the test section, which has a length of 2.4 m and a square cross-section with a side length of 0.61 m. The turbulence intensity is less than 0.08% and freestream uniformity is within ±0.5% over 95% of the cross-section. The freestream velocity uncertainty is less than 3% based on centerline Pitot-static tube calibration of the contraction pressure drop at the model location without the model present.

The experimental setup and coordinate system are shown in Fig. 6.1. An aluminium square flat plate model of chord $c$ =102 mm and thickness of 3.18 mm was employed. For all measurements, the Reynolds number was maintained at $\mathrm{Re}_c = 50\,000$ ($U_\infty$ =7.5 m s$^{-1}$), which is within the Reynolds number independence range for loading on flat plates [124]. The model was fixed at $\alpha = 30°$, corresponding to the stall angle for $\beta = 0°$. Importantly, this angle of attack is of relevance to major global solar energy producers [10] (Fig. 2.1). The model was mounted to a vertical sting with a diameter of 6 mm, representative of a ground-mounted solar panel. A gap

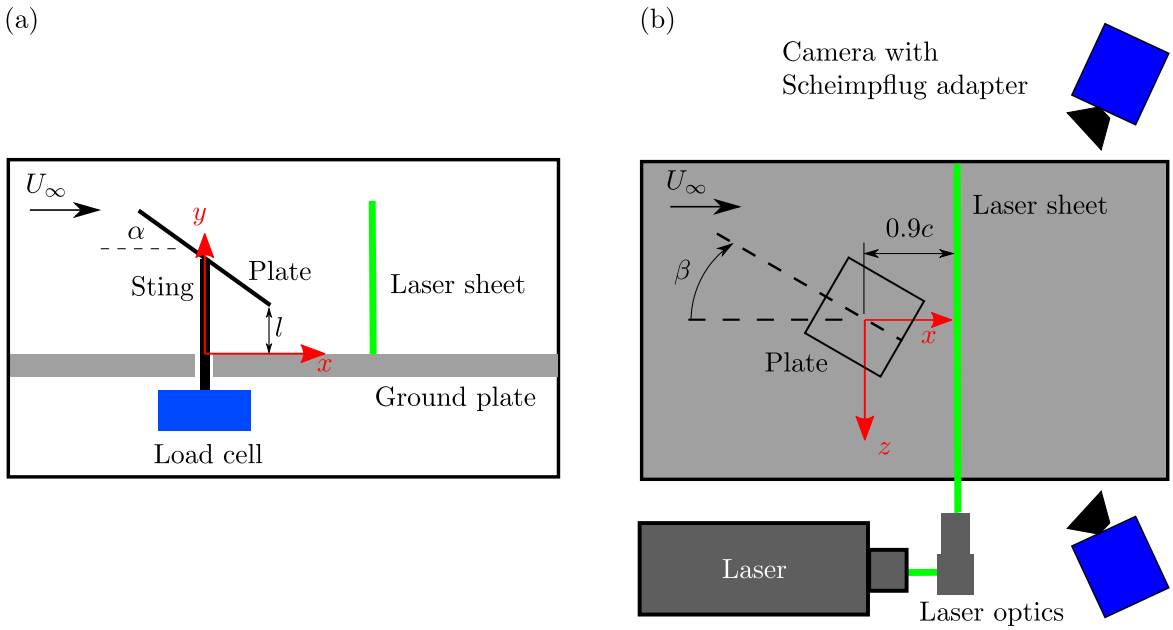


**Figure 6.1:** Schematic of the experimental setup for cross-plane SPIV measurements and coordinate system employed for data presentation. (a) side view and (b) top view.

ratio of $l/c = 0.1$ was used to simulate a solar panel under moderate ground effect conditions. In this configuration, the vertical plate position, $\alpha$, and $\beta$ were set to within ±0.5 mm, ±0.2°, and ±0.2°, respectively.

Lift was measured using a JR3-30E12A4 load cell mounted underneath the ground plate as shown in Fig. 6.1a. The lift signal was amplified using a JR3 amplifier. The load cell and amplifier were factory calibrated jointly, which was verified in situ using precision weights. The resultant resolution and calibration uncertainty were incorporated into the lift coefficient uncertainty. Contribution of the sting to the lift measurements was evaluated by decoupling the model and sting by the way of a separate sting assembly and orienting the model at the tested $\beta$ values. The ensemble averaged sting loads were centred about zero with fluctuations equivalent to quiescent measurements and are not expected to significantly augment instantaneous lift measurements. Raw lift measurements were filtered using a sixth order Chebyshev type II filter to achieve a steep roll-off and minimal passband ripple. A cut off frequency of 15 Hz was used to remove structural response and noise inherent to the load cell associated with frequencies well above that of dominant hydrodynamic events. The compound solid blockage was 2.2% which was accounted for by applying a solid blockage correction to the freestream dynamic pressure used to normalize the measured lift force [169, 197]. After accounting for notable sources of experimental uncertainty, the maximum uncertainty in the time-averaged lift coefficient is estimated to be ±0.04 over a 95% confidence interval.

Time-resolved stereoscopic planar particle image velocimetry (SPIV) in the cross-flow plane ($y$-$z$) was used to capture tip vortex development. Seeding particles were generated using a glycol-water fog mixture with a mean particle diameter of approximately 1 µm. Illumination of the tracer particles was facilitated by a Photonics DM20-527 single cavity dual pulsed laser,

**Table 6.1:** SPIV parameters

| Parameter | Value | Unit |
|---|---|---|
| Laser | Photonics DM20-527 | - |
| PIV Mode | Double frame | - |
| Cameras | $2 \times$ Photron SA4 | - |
| Sensor size | $1000 \times 1000$ | px $\times$ px |
| Lens focal length | 105 | mm |
| Magnification | 0.2 | - |
| Field of view | $150 \times 121$ | mm |
| | $1.47c \times 1.19c$ | - |
| Pulse separation | 100 | µs |
| Final window size | $16 \times 16$ (75% overlap) | px $\times$ px |
| Vector pitch | 0.43 mm | mm |
| | $0.0042c$ | - |
| Combined optical angle | 80° | |
| Sample rate | 1 | kHz |
| Number of images | 2700 | - |

conditioned into a laser sheet and introduced through the side of the tunnel as shown in Fig. 6.1. The laser sheet thickness was measured to be approximately 2 mm. Two 1 Mpx Photron SA4 high speed cameras outfitted with Nikon 105 mm lenses were used to capture particle images at an acquisition frequency of 1 kHz. Lens apertures were independently adjusted to compensate for the difference in particle image intensities due to the forward-backward scattering optical arrangement. The lenses were mounted to Scheimpflug adaptors to adjust the focal plane, resulting in a combined optical angle of 80°. Flow field measurements were collected $0.9c$ downstream of the origin for each test case as shown in Fig. 6.1. A physical calibration using a 106-10 LaVision 3D calibration plate was performed initially, then a self-calibration [182] was applied using 100 low seeding density particle images. The total field of view was 150 mm by 121 mm ($1.47c \times 1.19c$), resulting in a magnification factor of 0.2. The illumination and image acquisition were controlled by a LaVision high speed controller and Davis 8 software. The latter was also utilized for image processing using a multi-pass sequential cross-correlation algorithm with decreasing window sizes. The final window size was 16 px $\times$ 16 px with 75% overlap, resulting in vector pitches of less than $0.0042c$ for all cases. Relevant SPIV parameters are summarized in Table 6.1.

Comprehensive in-field characterizations of sudden changes in wind direction are unavailable in literature, however, IEC 61400-1 international standard provides a representative full-scale definition for wind turbines: $\Delta\beta = 30°$ over a time of 6 s. It stands to reason that photovoltaic installations would also be subjected to similar changes in wind direction. A change in the incoming wind direction was modelled in the present work by rotating the inclined flat plate, sting, and load cell assembly 30° in $t_c \approx 3.8$ (0.052 s) representing an extreme weather event in Ontario, Canada [84, 105]. The sudden yaw angle change was employed for two cases: one from $\beta = 30°$ to 0° (decreasing $\beta$) and another from $\beta = 0°$ to 30° (increasing $\beta$) as presented in Fig. 6.2.

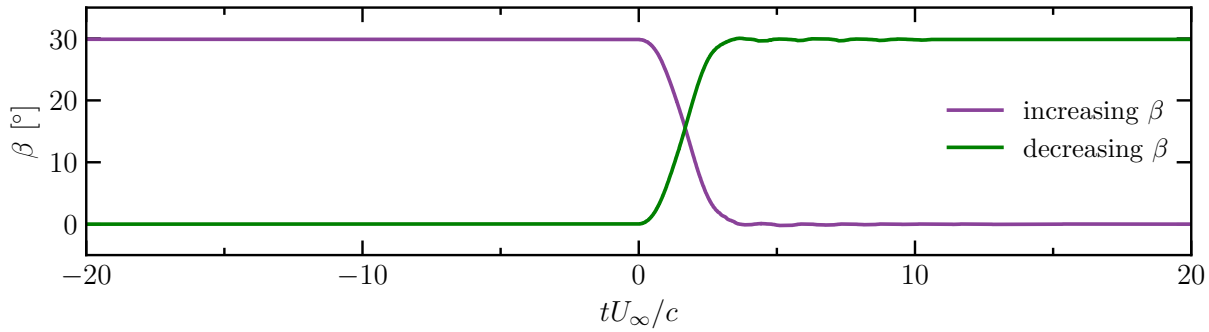


**Figure 6.2:** Ensemble average of prescribed ramp change in yaw angle for two rotation directions tested.

The flow field and force measurements were initiated simultaneously before the rotation of the model and synchronized to the motion using an embedded encoder and the laser Q-switch signal. All measurements apart from SPIV were acquired at 100 kHz. Data were collected between $-50 \leq t_c \leq 150$, where $t_c = 0$ is the motion start. For each of the two yaw angle variations, 20 trials were conducted and averaged to improve the convergence of the results. To determine the structural loading during sudden yaw angle changes, 20 additional trials for each motion profile were conducted under quiescent conditions. To serve as a baseline, steady flow and force measurements were collected at $\beta = 0°$, 10°, 20°, and 30°. For these cases, the PIV acquisition frequency was reduced to 100 Hz and 1000 images were captured. With the consideration of the variability between repeated trails, the maximum uncertainty in the instantaneous lift coefficient is estimated to be ±0.05 over a 95% confidence interval.

## 6.3 Steady State Lift and Flow Development

The time-averaged lift coefficient, $\overline{C_L}$, at $\beta = 0°$, 10°, 20°, and 30° is presented in Fig. 6.3. A maximum lift coefficient of 1.07 ± 0.04 is observed at $\beta = 0°$ and $\overline{C_L}$ decreases at an average rate of -0.004 per degree with respect to $\beta$. Previous lift coefficient results of yawed inclined flat plates from Chapter 5 and Mohapatra [25] are included for comparison. Also included in Fig. 6.3 are results from Shields & Mohseni [122] and Hartlin [206], which considered a "side-slip" plate arrangement, wherein $\alpha$ is kept constant with $\beta$ (i.e., the rotation axis is normal to the plate). Generally, the lift coefficient results from the present study agree well with previously reported values, though side-slip lift coefficients are higher than present results as $\alpha$ remains constant under side-slip, while the effective $\alpha$ decreases with $\beta$ for yawed plates. The results from Chapter 5 were collected under similar experimental conditions as the present study and demonstrates high repeatability. Lift coefficient of a yawed inclined flat plate by Mohapatra [25] (red triangles) show lower values compare to all other results presented in Fig. 6.3. The notably lower lift coefficients are attributed to the presence of under-body fins in their scaled down photovoltaic model, which are expected to reduce the effect of tip vortices and the generated lift, similar to winglets on aircraft wings [210].

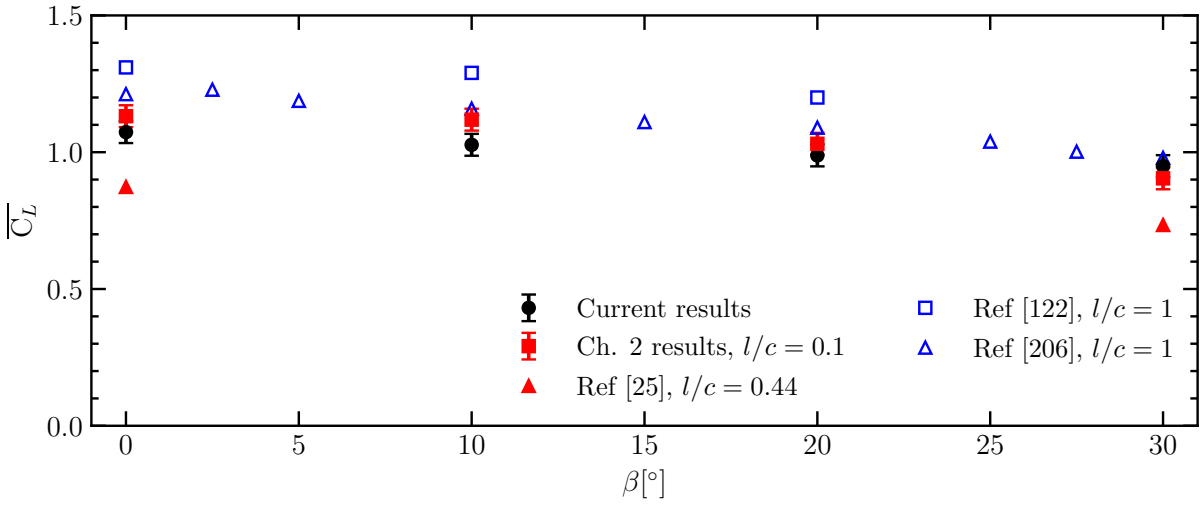


**Figure 6.3:** Time-averaged lift coefficient at fixed $\beta$. Results from the present study are indicated by black markers, while red markers indicate results from previous yawed plate studies. Results pertaining to side-slip configurations are indicated by blue markers, with $\beta$ corresponding to side-slip angle for these results. Experimental data are sourced from Chapter 5 results and Refs. [25, 122, 206]. Reproduced data are for AR = 1 and $\alpha = 30^\circ$.

As tip vortices in the near wake play a critical role in aiding high lift generation of low aspect ratio plates, the steady state effects of $\beta$ on the wake flow characteristics are examined using SPIV measurements downstream of the model (Fig. 6.1). Time-averaged normalized streamwise velocity contours are presented in Figs. 6.4a–6.4d for $\beta = 0^\circ$, $10^\circ$, $20^\circ$, and $30^\circ$. Overlaid on top are vortex core centres identified based on the $\Gamma_1$ method [192] and $\lambda_2$ contours [189] that demarcate the extent of each tip vortex. At $\beta = 0^\circ$, two regions of velocity deficit symmetric about $z/c = 0$ can be seen that correspond to the tip vortices. Another deficit region can be observed at $z/c = 0$ and $y/c \approx 0.15$, which is attributed to the extension of the leading-edge shear layer at this gap ratio for $\alpha = 30^\circ$ previously observed using midspan flow measurements in Chapter 4 (Figs. 4.5 and 4.6). A similar streamwise velocity topology was observed in Fig. 5.8 produced from the wake measurements in Chapter 5. With increasing $\beta$, the velocity deficits attributed to the tip vortices generally aligns with the tip vortex extents. The central deficit shifts towards the positive vortex as the flow between the two vortices is shifted along the $z/c > 0$ direction with $\beta \rightarrow 30^\circ$. The persistence of the central velocity deficit region between $0^\circ \leq \beta \leq 30^\circ$ suggests that the recirculation region over the suction side, though disrupted, is maintained, contributing to the relatively high lift generation (Fig. 6.3). There is an overall decrease in the average velocity deficit from $\beta = 0^\circ$ to $\beta = 30^\circ$, which is expected to result in a decrease in drag, in agreement with the drag coefficient results presented in Chapter 5 (Fig. 5.3a).

Time-averaged normalized streamwise vorticity contours are presented in Figs. 6.4e–6.4h for $\beta = 0^\circ$, $10^\circ$, $20^\circ$, and $30^\circ$. In all cases, two tip vortices of opposingly signed vorticity are observed. Between the two tip vortices, remnants of leading edge shear layer vorticity that rolled up around the tip vortices can be observed [19]. At $\beta = 0^\circ$, the vorticity field is symmetric about $z/c = 0$.

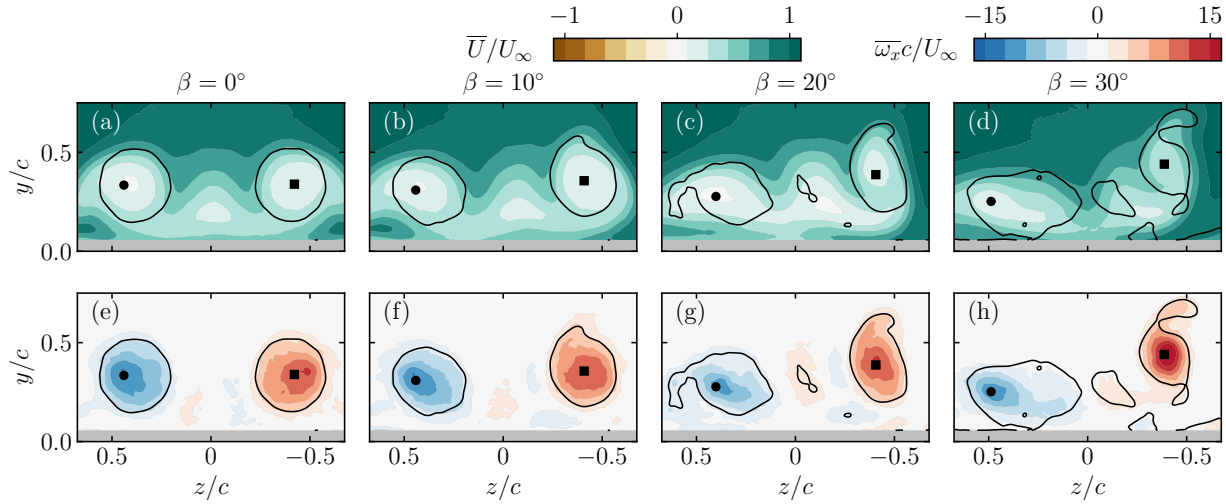


**Figure 6.4:** Time-averaged normalized (a-d) streamwise velocity and (e-h) vorticity contours for $\beta = 0°$, $\beta = 10°$, $\beta = 20°$, and $\beta = 30°$ overlaid with $\lambda_2$ contours. Vortex core centres are indicated by a filled black circle and square for negative and positive vortices, respectively. Closed outermost $\lambda_2$ contours indicated by a solid black line containing vortex cores are used for estimation of vortex circulation.

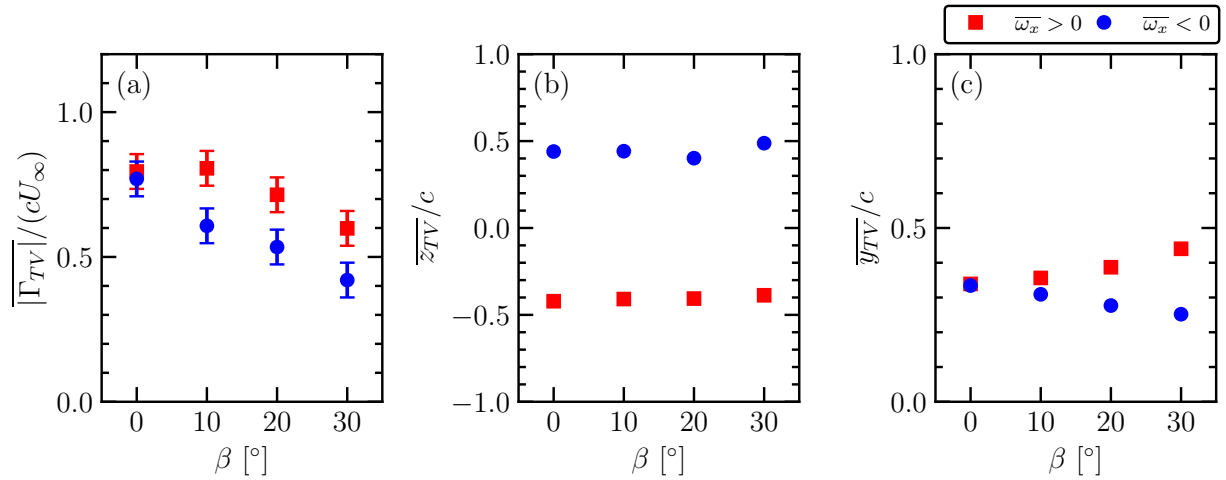


**Figure 6.5:** Steady state tip vortex (a) circulation magnitude, (b) spanwise core positions, and (c) wall normal core positions. Uncertainty is accommodated by marker size unless otherwise indicated with error bars.

Changes in the streamwise vorticity fields become significant for $\beta > 10°$ with notable changes in vortex core positions and average vorticity magnitudes within the $\lambda_2$ contours.

To supplement the qualitative description of the tip vortex topology in the preceding discussion, tip vortex circulations and core positions are extracted from the time-averaged flow fields. Circulation is estimated by computing a line integral of the in-plane velocity around the outermost $\lambda_2$ contour (Fig. 6.4) verified to contain each tip vortex core. This process was repeated for a range of $\lambda_2$ levels spanning several orders magnitudes. The $\lambda_2$ level used for circulation estimation was chosen as the value where the circulation variation for both tip vortices with respect to $\lambda_2$ was less than 3%. The maximum uncertainty is $\overline{\Gamma_{TV}}/(U_\infty c) = \pm 0.06$ for circulation estimates and $0.04c$ for vortex positions when accounting for measurement and methodological uncertainty.

Figure 6.5a presents time-averaged normalized tip vortex circulation magnitudes, $\overline{|\Gamma_{TV}|}/(cU_\infty)$. At $\beta = 0°$, the tip vortex circulations are equivalent, as expected. With increasing $\beta$, the normalized circulation of both tip vortices generally decreases. The circulation associated with the positive vortex remains constant between $\beta = 0°$ and 10°, before reducing with further increase in $\beta$, while the circulation of the negative vortex shows a monotonic decrease with increasing $\beta$. This is also evident in the streamwise vorticity fields shown in Fig. 6.4, where the topological variations of the negative tip vortex is more substantial relative to the positive tip vortex.

The time-averaged normalized lateral and wall normal positions of the vortex cores are shown in Fig. 6.5b and Fig. 6.5c, respectively. The lateral position is largely insensitive to changes in yaw angle, and the tip vortices remain stationary in the $z$ direction, slightly inboard of the spanwise edges of the plate. The wall-normal position of the tip vortices shows opposing trends with increasing $\beta$: the positive vortex moves upward, while the negative vortex moves toward the ground with respect to their positions at $\beta = 0°$. Mutual induction due to the difference in circulations between the tip vortices for $\beta > 0°$ is expected to cause relative motion in the counter-clockwise sense, supporting the increasing vertical gap between the tip vortices with $\beta$. Furthermore, surface flow visualization results in Chapter 5 (Figs. 5.6 and 5.7) demonstrated that the negative vortex develops along the plate tip and is released into the wake at the trailing edge, while the positive vortex departs the plate at a more upstream chordwise position, in alignment with the observed variations in $\overline{z_{TV}}/c$ and $\overline{y_{TV}}/c$ with $\beta$ in Fig. 6.5b and Fig. 6.5c, respectively.

## 6.4 Transient Lift and Flow Development

Ensemble-averaged filtered lift coefficient histories for increasing and decreasing $\beta$ cases are presented in Fig. 6.6. Prior to the inception of motion, the instantaneous lift coefficients are equivalent to corresponding steady state levels, indicated in the figure by horizontal dashed and dash-dotted lines. With the start of the wind direction change at $t_c = 0$, the instantaneous lift coefficient approaches the steady lift coefficient at the other limiting $\beta$ value. After the plate rotation, two to three oscillations with decaying peaks in the instantaneous lift coefficient are observed, which have a frequency that is an order of magnitude below the structural natural frequency and well below notable flow frequencies. For both motions, the oscillations subside within approximately five convective time units after the end of the motion ($t_c = 3.8$). The lift

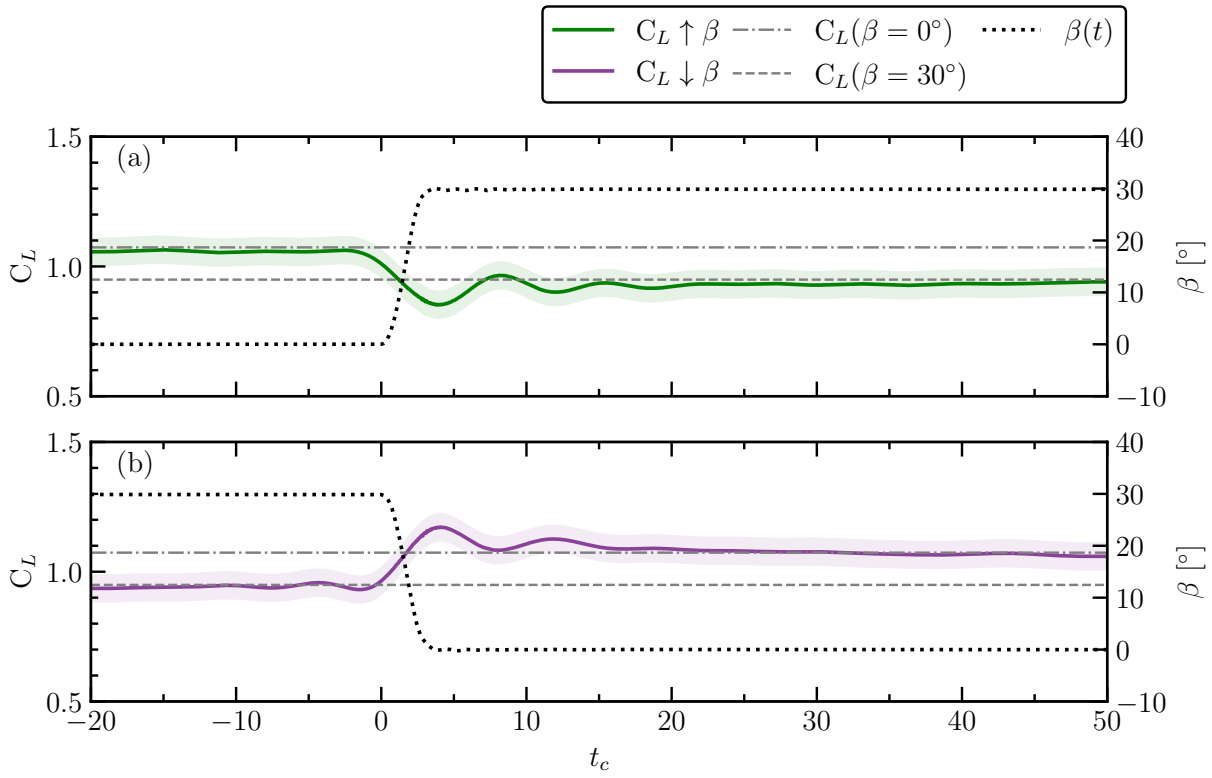


**Figure 6.6:** Instantaneous lift coefficients with respect to convective time for (a) increasing $\beta$, and (b) decreasing $\beta$. Coloured solid lines indicate nominal lift coefficient, and shaded regions indicate uncertainty bounds. Black dotted lines indicate instantaneous $\beta$. Dash-dot and dashed horizontal lines indicate steady state lift coefficients at $\beta = 0°$ and $\beta = 30°$, respectively.

coefficient overshoot after a sudden decrease in $\beta$ is approximately 10% above steady state levels at $\beta = 0°$ (Fig. 6.6b).

To better facilitate comparison of the loading histories for the various cases, the lift coefficient is presented with respect to $\beta$ in Fig. 6.7a. Lift coefficients of the two dynamic cases form a characteristic hysteresis loop about static $\beta$ values. To verify that the structural dynamics does not contribute to the observed hysteresis, the lift coefficient under quiescent flow conditions, shown in Fig. 6.7b, is subtracted from the active flow cases in Fig. 6.7a and the results are presented in Fig. 6.7c. Notably, the lift coefficient exhibits minor hysteretic behaviour in quiescent conditions, however, a hysteresis loop remains in the lift coefficient after removing the structural influence (Fig. 6.7c) that is similar to active flow conditions (Fig. 6.7a). This implies that lift coefficient hysteresis stems from flow behaviour rather than structural dynamics of the model during rotation. Once the transient structural response is accounted for, the lift coefficient for the increasing $\beta$ case matches steady state loading, however, the decreasing $\beta$ exhibits higher than steady state lift coefficient values.

To gain insight into the flow phenomenon responsible for the hysteretic behaviour between the two dynamic cases, normalized streamwise vorticity fields for static, increasing, and decreasing $\beta$ cases are presented in Fig. 6.8 for $\beta = 0°$, 10°, 20°, and 30°. The corresponding flow fields

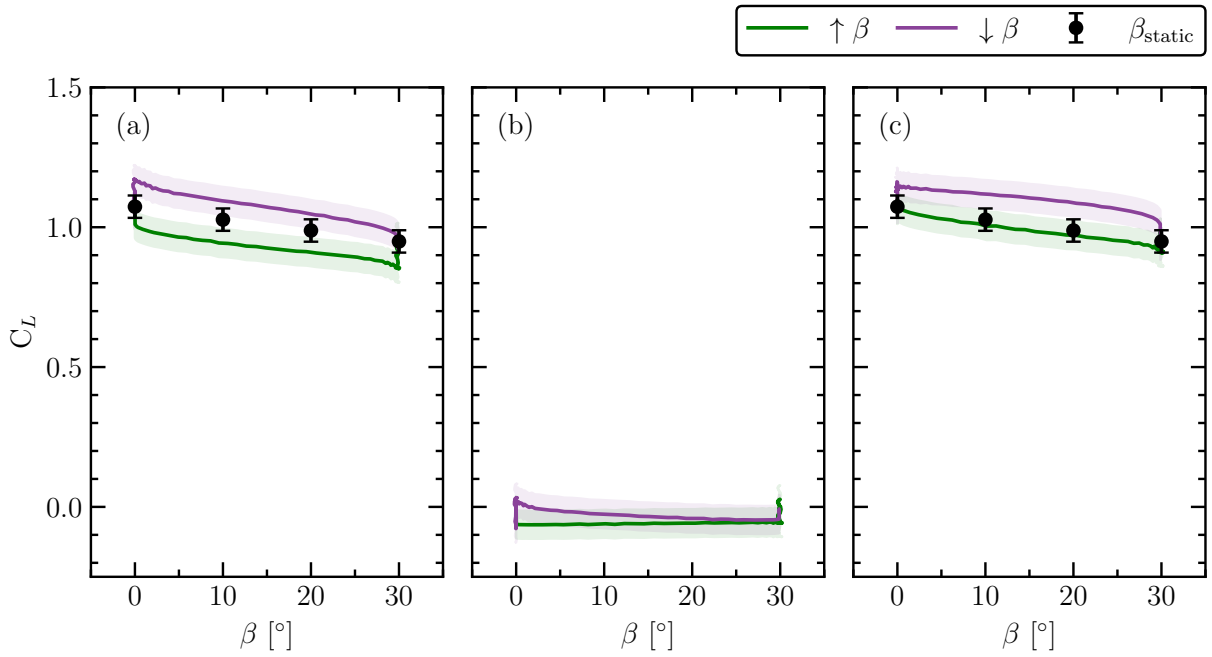


**Figure 6.7:** Instantaneous lift coefficient with respect to $\beta$ for (a) active flow, and (b) quiescent flow. Difference in the lift coefficient between active and quiescent conditions is shown in (c). Shaded regions indicate the uncertainty bounds of instantaneous lift coefficient.

for dynamic cases are marked by open markers in Fig. 6.8d. At $\beta = 0°$, a similar tip vortex topology is observed for all cases. Note, the $\lambda_2$ contours that outline tip vortices are less converged compared to the steady cases due to the limited number of realization used for ensemble averaging. However, the vortex cores are located in approximately the same positions for all the cases. At higher $\beta$ values, for both dynamic cases, the positive vortex is displaced in the positive wall normal direction, while the negative tip vortex translates in the opposite direction to a lesser extent, remaining aligned with the trailing edge of the model. For $\beta > 0°$, the vortex topology of the decreasing $\beta$ case (Fig. 6.8c) more closely resembles that of the static cases (Fig. 6.8a), compared to increasing $\beta$ cases (Fig. 6.8b). The flow response to the sudden yaw angle change for the increasing $\beta$ case appears to be delayed compared to the decreasing $\beta$ case, and supports the observed hysteresis in lift coefficient (Fig. 6.6).

Time histories of tip vortex circulation magnitude are shown in Fig. 6.9. Similar to static $\beta$ results (Section 6.3), the tip vortex circulations are determined using $\lambda_2$ criterion [189]. The selected $\lambda_2$ threshold used for circulation estimates was based on a 3% convergence criteria of the mode circulation in a time series of 1000 ensemble-averaged velocity fields each from both increasing and decreasing $\beta$ cases. Velocity fields acquired between $60 \leq tU_\infty/c \leq 135$ were used for the convergence study to ensure transients in the instantaneous vorticity fields have subsided and did not skew circulation statistics. Considering both measurement and methodological uncertainty, circulations are estimated to within $\pm 0.1\Gamma_{TV}/(cU_\infty)$ and vortex core positions to within $\pm 0.04c$. At limiting $\beta$ values, circulation magnitudes of each tip vortex are comparable. Furthermore, at

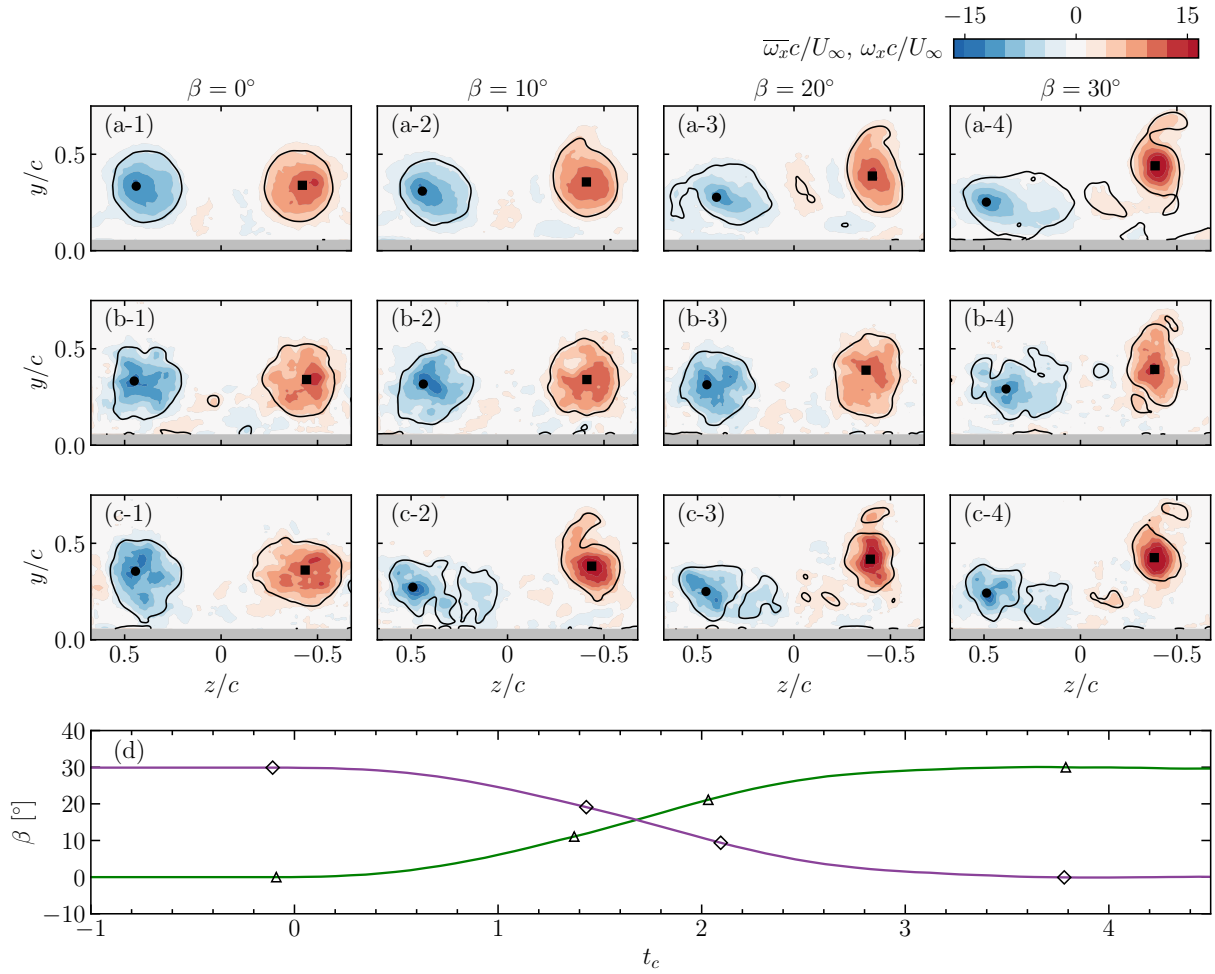


**Figure 6.8:** Normalized vorticity fields for (a) static $\beta$ cases (time-averaged), (b) increasing $\beta$ (ensemble-averaged), and (c) decreasing $\beta$ (ensemble-averaged). (d) Ensemble-averaged $\beta$ for increasing $\beta$ (purple) and decreasing $\beta$ (green) cases. Open face triangles and diamonds in (d) indicate selected snapshots in (b) and (c), respectively. Vortex core centres are indicated by a filled black circle and square for negative and positive vortices, respectively in (a)-(c). $\lambda_2$ contours are indicated by solid black lines.

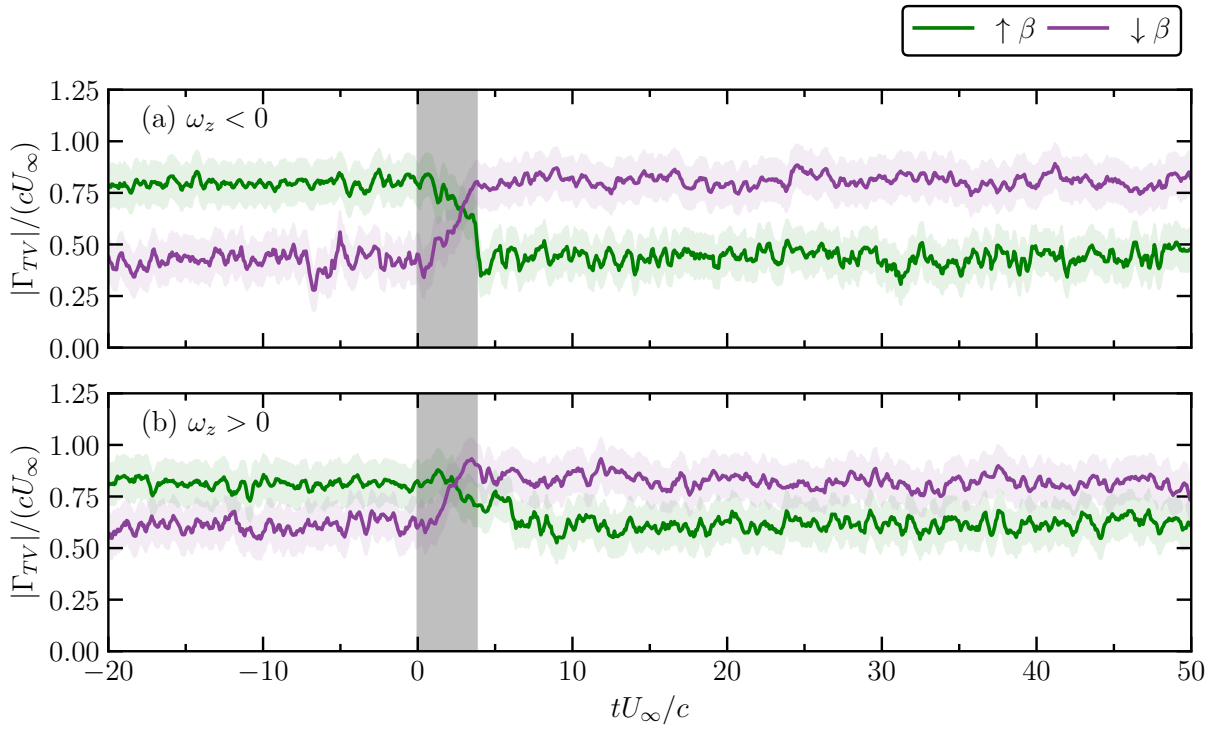


**Figure 6.9:** Normalized tip vortex circulation magnitude time histories for (a) negative, and (b) positive tip vortices. Shaded grey region in (a-b) indicates model rotation, while green and purple shaded regions indicate uncertainty.

times corresponding to $\beta = 0°$, the circulation magnitudes of both tip vortices are equivalent, while for $\beta = 30°$, the positive vortex circulation magnitude is higher relative to that of the negative tip vortex, in agreement with static $\beta$ results (Fig. 6.5a). Model rotation results in a reduction of tip vortex circulation magnitude for increasing $\beta$, while an opposite trend is observed for decreasing $\beta$. Notably, there is an approximate delay of 1 to 2 convective times units after the start of the motion before a change in the circulation magnitude can be reliably detected. In all cases, the duration associated with the circulation magnitude variation is roughly equivalent to the model rotation time, and no detectable transient circulation fluctuations are observed following model rotation.

Circulation magnitudes in Fig. 6.9 are presented in Fig. 6.10 with respect to $\beta$, which exhibit hysteresis loops for both the positive and negative tip vortices, similar to those observed in the lift coefficient in Fig. 6.7c. However, the increasing $\beta$ branch of the circulation magnitude hysteresis loop exhibits higher values in comparison to the decreasing $\beta$ branch, in direct opposition to the observed lift coefficient trends. The direct force measurements provide a measure of the lift without delay, while there is a time lag until the flow reaches the SPIV measurement plane. The distance between tip vortex formation and the measurement plane is $O(c)$, while the average streamwise velocity associated with tip vortices at the measurement plane is $O(U_\infty)$. Thus, the downstream convective time of the tip vortex flow is of $O(t_c)$. This is comparable to the delay observed in the time series of tip vortex circulation in Fig. 6.9. To statistically quantify the

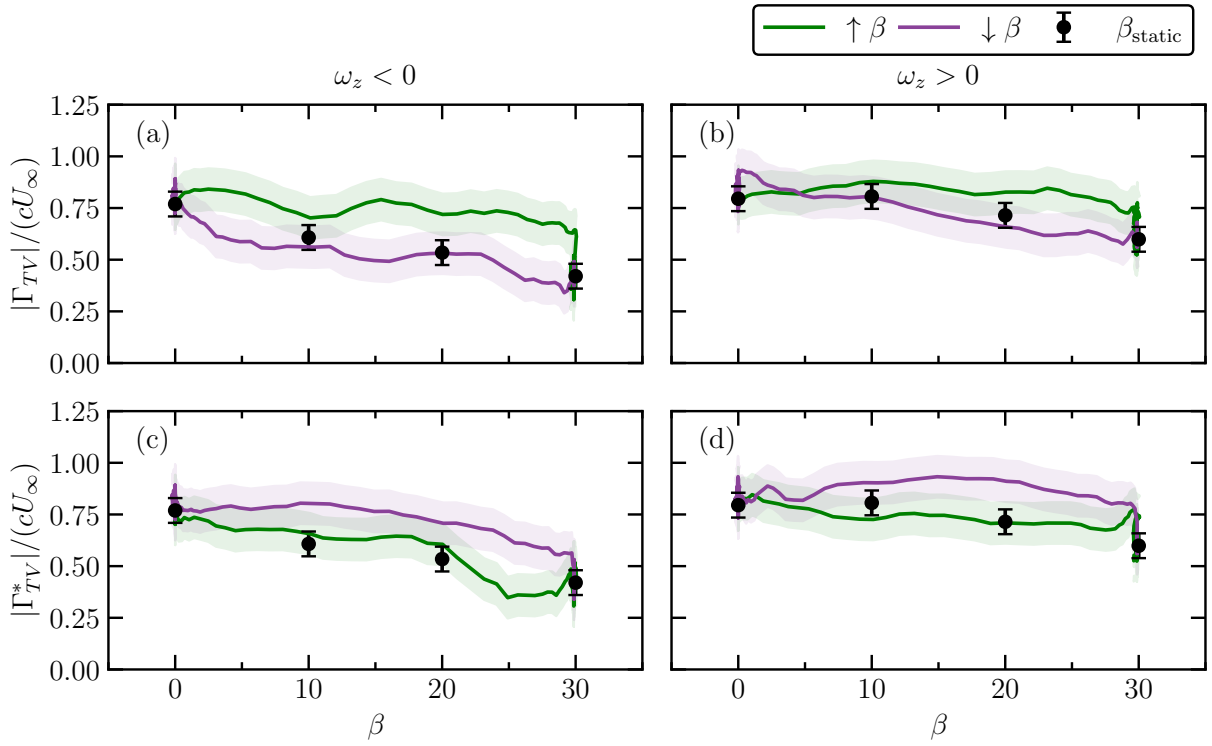


**Figure 6.10:** Normalized tip vortex circulation magnitude with respect to $\beta$. Negative and positive tip vortex circulation magnitudes are presented in the left and right columns, respectively. Circulations in (c) and (d) lead results in (a) and (b) by 1.73 convective time units. Circulation magnitudes for static $\beta$ cases are indicated using black circles. Green and purple shaded regions indicate uncertainty limits.

observed delay, streamwise velocity signal for all locations within $-0.25 \leq z/c \leq 0.25$ from each trial (corresponding to 22 000 individual signals) were cross correlated with the measured instantaneous $\beta$ and a mode time lag of 1.73 convective time units was observed corresponding to the maximum correlation value for both increasing and decreasing $\beta$ cases. Circulation magnitudes accounting for the convective time lag are presented in Figs. 6.10c and 6.10d. A hysteresis loop that matches the lift coefficient trends can be observed in the lag-adjusted normalized circulation magnitudes. These results highlight the key role tip vortices play in lift generation for time-varying $\beta$ that was previously observed for fixed $\beta$ in Chapter 5 and is marked as a source of the lift hysteresis.

In addition to tip vortex strength, their relative position to the inclined plate will also affect downwash over the suction side and consequently modify the lift generated through leading-edge shear layer reattachment [19]. To explore any hysteretic behaviour in the vortex trajectories, lateral and wall-normal positions of the tip vortex cores are presented in Fig. 6.11 for both dynamic and static $\beta$ cases. A hysteresis loop in the position of the negative tip vortex core is not observed and the positions are aligned closely between dynamic and static $\beta$ cases. Similarly, no hysteretic behaviour is observed in the tip vortex wall-normal position. A difference in the wall normal

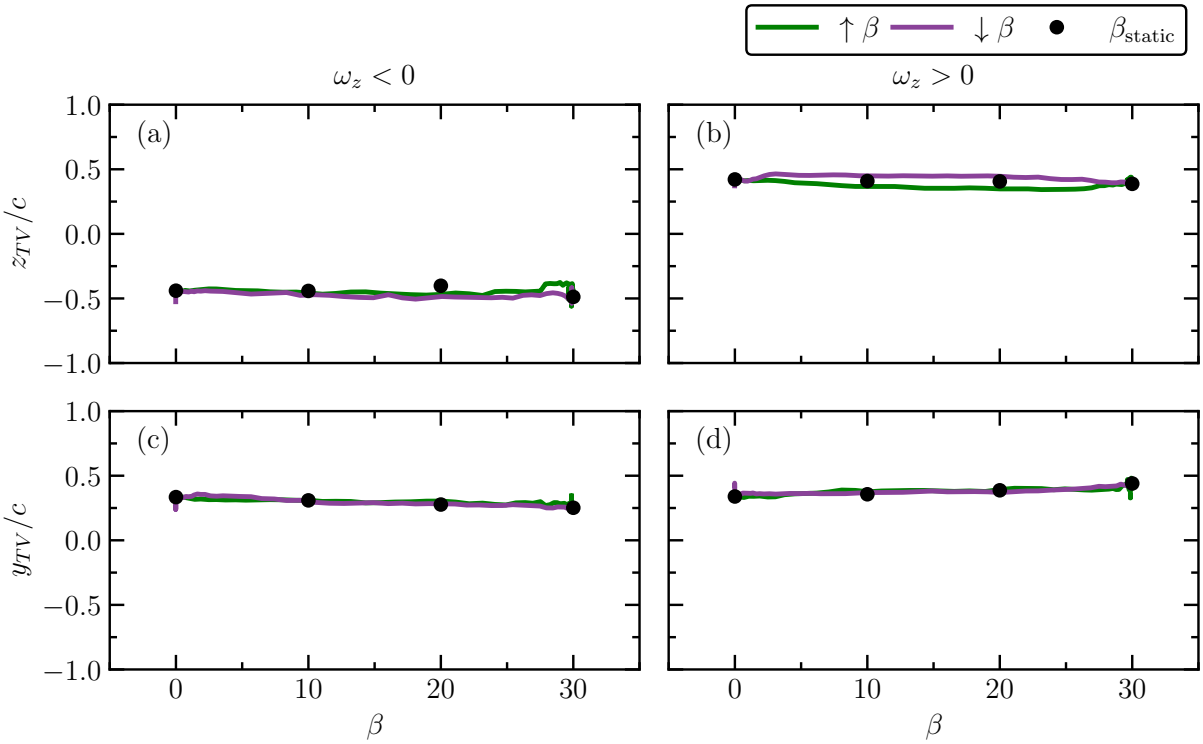


**Figure 6.11:** Lag-adjusted normalized tip vortex (a-b) lateral and (c-d) wall normal position within the measurement window with respect to instantaneous beta. Negative and positive tip vortex positions are presented in the left and right columns, respectively. Positions for static $\beta$ cases are indicated using black circles. Uncertainty limits are accommodated by the line width and marker size for dynamic and static $\beta$ cases, respectively.

position of the positive tip vortex between increasing and decreasing $\beta$ is observed, however, the maximum difference is less than 3%, and is comparable to experimental uncertainty. Based on these results, the tip vortex trajectories are not expected to contribute significantly to the lift coefficient hysteretic behavior (Fig. 6.7).

## 6.5 Concluding Remarks

An investigation was conducted to experimentally model a sudden wind direction change representing an extreme weather event at scales relevant to utility photovoltaic installations. A square inclined flat plate was oriented at $\alpha = 30°$ and $l/c = 0.1$ representing a critical loading case for lift; experiments were carried out at $\mathrm{Re}_c = 50\,000$. Both increasing and decreasing yaw rotations between $\beta = 0°$ and $30°$ were prescribed with rotation duration of $3.8t_c$. Dynamic results were also compared to steady state results at static yaw angles of $\beta = 0°$, $10°$, $20°$, and $30°$. Simultaneous time-resolved force and cross-plane stereoscopic velocity measurements were used to elucidate the connection between observed lift coefficient trends and tip vortex dynamics.

Direct lift measurements during sudden yaw variations demonstrate a ramp change in the lift coefficient with a maximum overshoot of 10%. The lift coefficient returned to steady state levels within five convective time units after cessation of motion. Most importantly, with the structural response removed, lift hysteresis is observed between the increasing and decreasing $\beta$ cases. The forces during increasing $\beta$ motion were comparable to lift at static $\beta$ levels, while greater than steady state lift was observed during a decreasing $\beta$ motion. Simultaneous flow measurements were used to associate lift coefficient trends to transient tip vortex evolution. The time histories of tip vortex circulations indicated a ramp change with a duration of approximately the motion time and transient behavior was undetectable. When accounting for convective time lag between the plate and the flow measurement plane, tip vortex circulations exhibited a hysteresis loop that agrees with lift results. On the other hand, tip vortex trajectories did not exhibit any significant hysteretic behavior.

Based on the angle of attack tested, the results of the present study are most representative of solar panel installations at latitudes near $\pm 40^{\circ}$, thus applicable to a primary global solar energy producers (i.e, China, USA, and Japan) [10]. In the context of photovoltaic installations, a decrease in $\beta$ is the limiting design case due to the increase in loading. To accommodate transient lift during such a sudden wind direction change, only a mild strengthening of solar panel support structures is needed based on the observed moderate lift overshoot. Extreme wind direction changes based on current civil standards are not expected to cause significant damage to photovoltaic installations and disrupt sun tracking abilities of solar panels with active actuators.

# Chapter 7

# Conclusions, Recommendations, & Future Work

*Key findings based on the result chapters are formulated and presented, along with extensions for future research.*

At initiation of this work, research objectives were outlined (Section 1.1) to address some knowledge gaps in the current understanding of finite-span inclined flat plate aerodynamics. In pursuit of these objectives, a series of experimental investigations were carried out to characterize the effect of key parameters relevant to photovoltaic installations. The effects of aspect ratio, angle of attack, yaw angle, and ground proximity on flow over the plate, wake development, and structural loading were examined under steady conditions (Chapters 4 and 5). Additionally, the effect of sudden yaw angle variations, representing extreme weather events, on instantaneous wake flow and lift force was explored (Chapter 6). In these experimental investigations, direct load measurements were facilitated by means of load cells, while both flow over the plate and wake flow development were evaluated using surface flow visualization and planar PIV techniques, providing valuable insight into the relation between loading trends and flow development. A holistic description of the main findings from these investigations are provided in Section 7.1, while extensions for future work are outlined in Section 7.2. The results are expected to aid in development of design guidelines for reducing energy production costs of future photovoltaic support structures.

## 7.1 Conclusions and Recommendations

As part of the investigations outlined in Chapters 4 and 5, the ground proximity of the inclined flat plate model was varied between free flight and moderate ground effect regimes. The influence of the ground clearance on both loading and flow development was experimentally assessed. For all cases, the results showed a notable variation in loading compared to free flight values for $l/c < 0.75$. Most importantly, ground proximity related changes in flow development and loading are dependent on the specific combination of aspect ratio, angle of attack, and yaw angle. From these results, a critical configuration of AR = 1, $\alpha = 30°$, $\beta = 0°$, and $l/c = 0.1$, which produces the maximum lift coefficient, was selected in order to study the aerodynamic effects of a sudden wind direction change in Chapter 6.

In the investigation presented in Chapter 4, ground proximity effects and their variation with aspect ratio and angle of attack was examined under headwind and tailwind conditions. Between pre-stall and stall angles, the lift and drag coefficients increase significantly due to an increase in the average static pressure difference normal to the plate (i.e., ram effect [154]) for headwinds. For tailwind conditions, at pre-stall angles of attack, an increase in edge velocity is observed with decreasing gap ratio and a recirculation region with a greater suction peak is detected on the AR = 1 plate. This significantly increases the lift coefficient with a minor increase in drag. Closer to the free flight stall angle, aerodynamic loading on the AR = 1 plate reduces with decreasing gap ratio due to the onset of stall under tailwinds. From the tests conducted using a plate of AR = 2 under tailwinds, the midspan flow and wake are observed to be insensitive to gap ratio changes leading to gap ratio-invariant aerodynamic loading for all pre-stall angles tested. At post-stall angles of attack, ground effect on both flow and forces are minimal for both aspect ratios tested due to the massively separated leading edge shear layer.

To clarify the opposing trends in the aerodynamic loading variations with gap ratio under headwind and tailwind conditions, a second investigation was conducted using a square flat plate

(Chapter 5). The model was placed at $\alpha = 30°$, corresponding to a maximum lift configuration, and yaw angles between $0° \leq \beta \leq 180°$ representing wind directions between headwinds and tailwinds. For yaw angles $\beta < 90°$, gap ratio-invariant suction surface flow topology and tip vortices are present, and the rise in aerodynamic loading with decreasing gap ratio is driven by the ram effect. For yaw angles $90° \leq \beta \leq 120°$, the suction side flow and tip vortices remain insensitive to gap ratio variations. At $\beta = 120°$, the surface flow topology is comparable to a slender delta wing and lacks a leading edge shear layer essential for generating high aerodynamic loads. Coupled with the absence of ram effect, the aerodynamic loading is gap ratio-invariant for $90° \leq \beta \leq 120°$. Between $120° \leq \beta < 150°$, the sting placement on the suction side surface confounds the effects of ground proximity on the lift coefficient and surface flow topology. A minor increase in wake deficit for $\beta > 90°$ is also present, however, the sting effect on drag and also other loading coefficients are negligible. Close to $\beta \approx 150°$, the ground facing suction side flow is increasingly disrupted with closer ground proximity and the onset of partial stall results in lower aerodynamic loads compared to free flight. This phenomenon becomes increasingly pronounced as the yaw angle approaches 180°, where the greatest decrease in total loading between free flight and in-ground cases is observed due to complete stall.

Under realistic use cases, photovoltaic installations are subjected to unsteadiness in the incoming flow due to transient weather events, which necessitated an investigation into effects of sudden wind direction changes on the aerodynamics of a square flat plate in close ground proximity (Chapter 6). Wind direction variations between $\beta = 0°$ and 30° occurring over 3.8 convective time units were modelled for comparison for both rotation directions. During the wind direction change, the lift coefficient linearly varies, and reaches a local maximum or minimum at the end of the wind direction change, which is followed by notable oscillations that decrease in approximately 12 convective time units. For the decreasing $\beta$ case (from $\beta = 30°$ to 0°), a lift coefficient overshoot of 10% above steady state levels at $\beta = 0°$ is observed. Notable hysteresis is observed in the lift coefficient between the two rotation directions, which is confirmed to originate from differences in the tip vortex characteristics. Specifically, tip vortex circulations show hysteretic behavior matching that of the lift coefficient, highlighting the crucial role played by these vortices in lift generation on low aspect ratio plates under unsteady conditions. Tip vortex trajectories during the yaw motions coincide with steady state core positions and do not contribute significantly to lift hysteresis.

With respect to the main application of photovoltaic installations considered in this work, the investigated angles of attack were most representative of solar power installations at latitudes between ± 25° to 50°, covering geographical regions where 60% of the global solar energy was produced in 2021 [10]. Based on the discussions in Chapters 4 and 5, some practical considerations can be outlined towards the goal of lowering steady wind loading on solar panels. The results point to notable variation in ground effect with wind direction, which can be leveraged for load reduction, following in-field measurements of wind direction at potential installation sites. It is crucial that site assessments are conducted for sufficient duration such that periodic trends in local climate are captured. Ideally, the panel should be placed at $\beta = 90°$, such that all wind loads are nearly zero at any gap distance, however, this is impractical and would result in inefficient power production depending on the geographical location. If the measured wind direction distribution is mainly between 0° and 90°, then the panel should be placed at a minimum gap distance equivalent

to its chord (width) to lower loads. At $\beta = 0°$, where peak loads are observed, this would result in approximately a 10% reduction in loads compared to the lowest gap distance tested. The out-of-ground effect panel placement would also result in improved cooling [211], increasing power production efficiency. On the other hand, if the measured wind direction distribution is greater than 90°, then solar panels should be placed as close to the ground as possible in order to benefit from the load reduction observed for $\beta > 150°$. Specifically, peak loading at $\beta = 180°$ decreased by 20% to 30% when the gap distance was decreased from a out-of-ground effect configuration ($l/c = 1$) to a ground effect configuration ($l/c = 0.1$). The lower ground height may be detrimental for panel cooling [211] due to the overall decrease momentum of the flow over the panel surfaces however, and as such, the decrease in ground height should be balanced with natural cooling performance. If the space permits, and the panel is fixed in position, use of larger aspect ratios is also recommended barring any undesired dynamic structural behaviors stemming from the slender geometry, which has the added benefit of aerodynamic loads that are largely invariant to ground proximity, at least for tailwind conditions ($\beta = 180°$). Although a hysteretic lift response is observed during a sudden wind direction change presented in Chapter 6, the peak lift coefficient overshoot of 10% means that current support structures are sufficient with appropriate safety factors to withstand an extreme weather event as defined by relevant civil structure standards ($\Delta\beta = \pm 30°$ over $\Delta t = 6\,\mathrm{s}$).

## 7.2 Future Work

The present work demonstrated the existence of optimal configurations of panel placement in terms of minimizing wind loading, however, there are other factors relevant to solar panels that must be considered. Recent work has demonstrated that the panel cooling by convection is a function of the ground clearance and the rate of cooling can be increased by 80% by doubling the ground clearance in staggered and uniform height solar farm arrays [211]. Although, aerodynamic loading can be decreased with lower gap ratio under tailwinds, this results in reduced panel cooling and therefore decreasing panel power efficiencies. Ultimately, there is a tradeoff between reducing structural loading and maximizing the power generated, both of which affect the levelized cost of power production. Although research effort has been directed towards understanding variation in thermal [e.g., 211–214] and aerodynamic [e.g., 15, 18, 21] characteristics with relevant parameters, the combination of thermal and aerodynamic performance remains to be investigated under equivalent conditions. Furthermore, examination of the thermal characteristics of the ground surface beneath a solar panel is of interest for mixed-use spaces in both urban and agricultural settings.

Assessment of aspect ratio effects on aerodynamic loading in Chapter 4 demonstrated reduction of loads at higher aspect ratios due to diminished tip effects. Furthermore, at higher aspect ratios, variations in lift and drag with respect to gap ratio were consistent for pre-stall angles relative to lower aspect ratio plates, where opposing trends in loading are observed across the range of pre-stall angles. These characteristics make use of larger aspect ratios an attractive option for reducing wind loading, and therefore costs associated with structural supports. However, actuated pylon designs are desirable for sun tracking [38] and stowing during extreme weather events [24, 42]. Although use of high AR panels leads to an overall reduction in steady wind loads, the same

makes them susceptible to dynamic structural instabilities [215, 216], which are exacerbated by actuated central pylon designs. Additionally, current civil codes provide insufficient guidelines for minimizing resonant loading on high AR solar panels [215]. The influence of panel orientation and placement on the aerodynamics of high AR solar panels under steady incoming wind remains to be systematically investigated. The results will provide an improved understanding of the connection between flow development and dynamic structural response for slender solar panels, which can drive future cost-saving strategies.

Previous investigations have examined the effect of aspect ratio on aerodynamic loading from which a practical demarcation of the low and high aspect ratio range was determined to be AR $\leq 1$ and AR $\geq 2$, respectively [18, 19, 110]. Jardin *et al.* [204] determined that the leading edge vortex formed during a pitching and flapping wing remained attached due to strong tip effects for a flat plate of AR = 1.4. Similarly, Fukuda *et al.* [15] observed leading edge shear layer reattachment facilitated by tip vortices on a plate of AR = 1.3 for steady incoming flow conditions. These studies suggests that there is a critical aspect ratio between $1 \leq$ AR $\leq 2$, where the influence of tip effects weakens and the leading edge shear layer no longer reattaches reducing aerodynamic loads. It is possible that the critical aspect ratio varies with angle of attack, wind direction, and ground proximity as they directly affect the tip vortex characteristics (Chapters 4 and 5). Determination of this critical aspect ratio range remains to be systematically investigated and is expected to benefit the development and implementation of flow control strategies for load reduction.

In Chapter 6, a sudden change in wind direction was modelled based on currently available civil design code guidelines to represent an extreme weather event. In addition to changes in wind directions, a sudden increase in the local wind speed or a combination of both a wind speed and direction is also possible. The peak wind speeds during gusts have been observed to be between 1 to 4 times nominal levels globally [57, 78, 83], though some extreme weather events have resulted in peak wind speeds that are an order of magnitude higher than average wind speeds [57]. Concurrently, infield measurements of non-dimensional gust rise times are within the quasi-steady regime ($> O(10)$) [133] and can be modelled using steady flow conditions. However, a comprehensive characterization of rise times associated with extreme weather events is currently lacking. It is possible that wind velocity changes occurs at the same order of rise times as wind direction changes during extreme weather events, as codified in civil design standards. At such gust rise times ($O(1)$), the dynamic loads have the potential to exceed structural design envelopes and require consideration for appropriate structural sizing. As the structural loads scale with the square of the freestream speed, an extreme gust may significantly increase loading with potential for large capital losses due to damage to solar panels. Under headwind conditions, close ground proximity may amplify these dynamic loads due to ram effect, exacerbating the likelihood of downtime. Thus, the effect of an accelerating freestream representative of an extreme weather event on the ground effect aerodynamics of an inclined flat plate should be investigated.

The present work focused on forging a link between aerodynamic loading and salient features of flow development on inclined flat plates in ground effect, which expectedly lays the foundation for investigation of flow control strategies. The results demonstrate that leading-edge shear layer reattachment due to tip vortices plays a key role in load generation on square plates for both steady and dynamic conditions. Furthermore, lower aspect ratios may reduce undesirable structural instabilities, circumventing the need for stronger support structures. Thus, exploration of flow

control methods specific to lower aspect ratio flat plates in ground effect that target the development of the leading-edge shear layer and tip vortices, is of interest. Particularly, passive methods should be considered over those that use some of the generated solar power, in order to maintain energy production efficiencies. Some possible research avenues include baffle devices or use of eccentric and actuated panel shapes, which has been preliminarily explored [13, 25, 41], yet remains to be systematically investigated. Inspired by bird wings, recent aerodynamic studies employing higher AR flat plates have demonstrated the stabilization of the leading-edge vortex and separation delay through the use of alulas [217, 218], which also presents a possible avenue for passively modifying solar panel wind loading with minimal blockage of incoming solar irradiance. Most importantly, a robust cost-benefit analysis is integral to all future flow control and should be considered to ensure that there is a net reduction in energy production costs.

# References


[1] Pirani, S. 2018 *Burning Up: A Global History of Fossil Fuel Consumption by Simon Pirani*. Pluto Press. ISBN. ↩

[2] Held, I. M. & Soden, B. J. 2006 Robust Responses of the Hydrological Cycle to Global Warming. *J. Clim.* **19** (21), 5686–5699. DOI. ↩

[3] Hansen, J., Sato, M., Ruedy, R., Lo, K., Lea, D. W., & Medina-Elizade, M. 2006 Global temperature change. *Proc. Natl. Acad. Sci. U. S. A.* **103** (39), 14288–14293. DOI. ↩

[4] Polyakov, I. V., Timokhov, L. A., Alexeev, V. A., Bacon, S., Dmitrenko, I. A., Fortier, L., Frolov, I. E., Gascard, J. C., Hansen, E., Ivanov, V. V., Laxon, S., Mauritzen, C., Perovich, D., Shimada, K., Simmons, H. L., Sokolov, V. T., Steele, M., & Toole, J. 2010 Arctic ocean warming contributes to reduced polar ice cap. *J. Phys. Oceanogr.* **40** (12), 2743–2756. DOI. ↩

[5] Houghton, J. 2005 Global warming. *Reports Prog. Phys.* **68** (6), 1343–1403. DOI. ↩

[6] Barbir, F., Veziroğlu, T. N., & Plass, H. J. 1990 Environmental damage due to fossil fuels use. *Int. J. Hydrogen Energy* **15** (10), 739–749. DOI. ↩

[7] Martins, F., Felgueiras, C., Smitkova, M., & Caetano, N. 2019 Analysis of fossil fuel energy consumption and environmental impacts in european countries. *Energies* **12** (6), 1–11. DOI. ↩

[8] Rosa, E. A. & Dietz, T. 2012 Human drivers of national greenhouse-gas emissions. *Nat. Clim. Chang.* **2** (8), 581–586. DOI. ↩

[9] REN21. 2019 Renewables 2019 Global Status Report, Paris, REN21 Secretariat. URL. ↩

[10] REN21. 2022 Renewables 2022 Global Status Report, Paris, REN21 Secretariat. URL. ↩

[11] Ramasamy, V., Zuboy, J., Shaughnessy, E. O., Feldman, D., Desai, J., Woodhouse, M., Basore, P., & Margolis, R. 2022 U . S . Solar Photovoltaic System and Energy Storage Cost Benchmarks , With Minimum Sustainable Price Analysis : Q1 2022. *Tech. rep.* NREL/TP-7A40-83586, National Renewable Energy Laboratory, Golden, CO. URL. ↩

[12] Fu, R., Feldman, D., & Margolis, R. 2018 U . S . Solar Photovoltaic System Cost Benchmark : Q1 2018. *Tech. rep.* NREL/TP-6A20-72399, National Renewable Energy Laboratory, Golden, CO. URL. ↩

[13] Pfahl, A. 2013 Survey of Heliostat Concepts for Cost Reduction. *J. Sol. Energy Eng.* **136** (1), 014501. DOI. ↩

[14] Fage, A. & Johansen, F. C. 1927 On the Flow of Air behind an Inclined Flat Plate of Infinite Span. *Proc. R. Soc. A Math. Phys. Eng. Sci.* **116** (773), 170–197. DOI. ↩

[15] Fukuda, K., Balachandar, R., & Barron, R. M. 2020 Analysis of the ground effect on development of flow structures around an inclined solar panel. *Environ. Fluid Mech.* **20** (6), 1463–1489. DOI. ↩

[16] Pfahl, A., Brucks, A., & Holze, C. 2013 Wind load reduction for light-weight heliostats. *Energy Procedia* **49**, 193–200. DOI. ↩

[17] Jubayer, C. M. & Hangan, H. 2016 A numerical approach to the investigation of wind loading on an array of ground mounted solar photovoltaic (PV) panels. *J. Wind Eng. Ind. Aerodyn.* **153**, 60–70. DOI. ↩

[18] Ortiz, X., Rival, D., & Wood, D. 2015 Forces and moments on flat plates of small aspect ratio with Application to PV wind loads and small wind turbine blades. *Energies* **8** (4), 2438–2453. DOI. ↩

[19] DeVoria, A. C. & Mohseni, K. 2017 On the mechanism of high-incidence lift generation for steadily translating low-aspect-ratio wings. *J. Fluid Mech.* **813**, 110–126. DOI. ↩

[20] Dong, L., Choi, K. S., & Mao, X. 2020 Interplay of the leading-edge vortex and the tip vortex of a low-aspect-ratio thin wing. *Exp. Fluids* **61** (9), 1–15. DOI. ↩

[21] Shademan, M. & Naghib-Lahouti, A. 2020 Effects of aspect ratio and inclination angle on aerodynamic loads of a flat plate. *Adv. Aerodyn.* **2** (1). DOI. ↩

[22] Gutierrez-Castillo, P., Aguilar-Cabello, J., Alcalde-Morales, S., Parras, L., & del Pino, C. 2021 On the lift curve slope for rectangular flat plate wings at moderate Reynolds number. *J. Wind Eng. Ind. Aerodyn.* **208** (December 2020), 104459. DOI. ↩

[23] Linehan, T. & Mohseni, K. 2017 Leading-edge flow reattachment and the lateral static stability of low-aspect-ratio rectangular wings. *Phys. Rev. Fluids* **2** (11), 1–23. DOI. ↩

[24] Emes, M. J., Ghanadi, F., Arjomandi, M., & Kelso, R. M. 2018 Investigation of peak wind loads on tandem heliostats in stow position. *Renew. Energy* **121**, 548–558. DOI. ↩

[25] Mohapatra, S. 2011 *Wind tunnel investigation of wind load on a ground mounted photovoltaic tracker*. Master, Colorado State University. ↩

[26] Merarda, H., Aksas, M., & Andrianne, T. 2020 Shape effects on aerodynamic loading of heliostats. *Mech. Ind.* **21** (6), 1–16. DOI. ↩

[27] Yemenici, O. & Aksoy, M. O. 2021 An experimental and numerical study of wind effects on a ground-mounted solar panel at different panel tilt angles and wind directions. *J. Wind Eng. Ind. Aerodyn.* **213** (April), 104630. DOI. ↩

[28] Shademan, M., Barron, R., Balachandar, R., & Hangan, H. 2014 Numerical simulation of wind loading on ground-mounted solar panels at different flow configurations. *Can. J. Civ. Eng.* **41** (8), 728–738. DOI. ↩

[29] Bleischwitz, R., de Kat, R., & Ganapathisubramani, B. 2016 Aeromechanics of membrane and rigid wings in and out of ground-effect at moderate Reynolds numbers. *J. Fluids Struct.* **62**, 318–331. DOI. ↩

[30] Emes, M. J., Jafari, A., Ghanadi, F., & Arjomandi, M. 2019 Hinge and overturning moments due to unsteady heliostat pressure distributions in a turbulent atmospheric boundary layer. *Sol. Energy* **193** (September), 604–617. DOI. ↩

[31] Fadlallah, S. O., Anderson, T. N., & Nates, R. J. 2021 Flow behaviour and aerodynamic loading on a stand-alone heliostat: wind incidence effect. *Arab. J. Sci. Eng.* **46** (8), 7303–7321. DOI. ↩

[32] Yadav, A. K. & Chandel, S. S. 2013 Tilt angle optimization to maximize incident solar radiation: A review. *Renew. Sustain. Energy Rev.* **23**, 503–513. DOI. ↩

[33] Warsido, W. P., Bitsuamlak, G. T., Barata, J., & Gan Chowdhury, A. 2014 Influence of spacing parameters on the wind loading of solar array. *J. Fluids Struct.* **48**, 295–315. DOI. ↩

[34] Sahu, A., Yadav, N., & Sudhakar, K. 2016 Floating photovoltaic power plant: A review. *Renew. Sustain. Energy Rev.* **66**, 815–824. DOI. ↩

[35] Benghanem, M. 2011 Optimization of tilt angle for solar panel: Case study for Madinah, Saudi Arabia. *Appl. Energy* **88** (4), 1427–1433. DOI. ↩

[36] Ma, T., Yang, H., Lu, L., & Peng, J. 2014 Technical feasibility study on a standalone hybrid solar-wind system with pumped hydro storage for a remote island in Hong Kong. *Renew. Energy* **69**, 7–15. DOI. ↩

[37] Carrilho da Graça, G., Augusto, A., & Lerer, M. M. 2012 Solar powered net zero energy houses for southern Europe: Feasibility study. *Sol. Energy* **86** (1), 634–646. DOI. ↩

[38] Eldin, S. A., Abd-Elhady, M. S., & Kandil, H. A. 2016 Feasibility of solar tracking systems for PV panels in hot and cold regions. *Renew. Energy* **85**, 228–233. DOI. ↩

[39] Kamalapur, G. D. & Udaykumar, R. Y. 2011 Rural electrification in India and feasibility of Photovoltaic Solar Home Systems. *Int. J. Electr. Power Energy Syst.* **33** (3), 594–599. DOI. ↩

[40] Saidan, M., Albaali, A. G., Alasis, E., & Kaldellis, J. K. 2016 Experimental study on the effect of dust deposition on solar photovoltaic panels in desert environment. *Renew. Energy* **92**, 499–505. DOI. ↩

[41] Pfahl, A., Randt, M., Holze, C., & Unterschütz, S. 2013 Autonomous light-weight heliostat with rim drives. *Sol. Energy* **92**, 230–240. DOI. ↩

[42] Emes, M. J., Arjomandi, M., Ghanadi, F., & Kelso, R. M. 2017 Effect of turbulence characteristics in the atmospheric surface layer on the peak wind loads on heliostats in stow position. *Sol. Energy* **157** (February), 284–297. DOI. ↩

[43] Gong, B., Li, Z., Wang, Z., & Wang, Y. 2012 Wind-induced dynamic response of Heliostat. *Renew. Energy* **38** (1), 206–213. DOI. ↩

[44] Raine, J. & Stevenson, D. 1977 Wind protection by model fences in a simulated atmospheric boundary layer. *J. Wind Eng. Ind. Aerodyn.* **2** (2), 159–180. DOI. ↩

[45] Jubayer, C. M. & Hangan, H. 2015 Numerical simulation of wind effects on a stand-alone ground mounted Photovoltaic (PV) system. *J. Wind Eng. Ind. Aerodyn.* **134**, 1–37. DOI. ↩

[46] Peterka, J., Hosoya, N., Bienkiewicz, B., & Cermak, J. 1986 Wind load reduction for heliostats. *Tech. rep.* SERI/STR-253-2859, National Renewable Energy Laboratory, Golden, CO. DOI. ↩

[47] Yu, J. S., Emes, M. J., Ghanadi, F., Arjomandi, M., & Kelso, R. 2019 Experimental investigation of peak wind loads on tandem operating heliostats within an atmospheric boundary layer. *Sol. Energy* **183** (June 2018), 248–259. DOI. ↩

[48] Garratt, J. R. 1992 *The Atmospheric Boundary Layer*. Houghton, J., Rycroft, M., & Dessler, A., editors. Cambridge University Press. ISBN. ↩

[49] Azad, R. S. 1993 *The Atmospheric Boundary Layer for Engineers*, vol. 17 of *Fluid Mechanics and Its Applications*. Springer Netherlands. DOI. ↩

[50] Stull, R. B. 1988 *An Introduction to Boundary Layer Meteorology*. Springer Netherlands. DOI. ↩

[51] Metzger, M., McKeon, B., & Holmes, H. 2007 The near-neutral atmospheric surface layer: turbulence and non-stationarity. *Philos. Trans. R. Soc. A Math. Phys. Eng. Sci.* **365** (1852), 859–876. DOI. ↩

[52] Monty, J. P., Chong, M. S., Hutchins, N., & Marusic, I. 2006 Surface shear stress fluctuations in the atmospheric surface layer. In *Proc. Elev. Asian Congr. Fluid Mech.* Number May. URL. ↩

[53] Hommema, S. E. & Adrian, R. J. 2003 Packet Structure of Surface Eddies in the Atmospheric Boundary Layer. *Boundary-Layer Meteorol.* **106** (1), 147–170. DOI. ↩

[54] Hutchins, N., Chauhan, K., Marusic, I., Monty, J., & Klewicki, J. 2012 Towards reconciling the large-scale structure of turbulent boundary layers in the atmosphere and laboratory. *Boundary-Layer Meteorol.* **145** (2), 273–306. DOI. ↩

[55] Clauser, F. 1954 Turbulent Boundary Layers in Adverse Pressure Gradients. *J. Aeronaut. Sci.* **21** (2), 91–108. DOI. ↩

[56] Degraaff, D. B. & Eaton, J. K. 2000 Reynolds-number scaling of the flat-plate turbulent boundary layer. *J. Fluid Mech.* **422**, 319–346. DOI. ↩

[57] Fu, J. Y., Li, Q. S., Wu, J. R., Xiao, Y. Q., & Song, L. L. 2008 Field measurements of boundary layer wind characteristics and wind-induced responses of super-tall buildings. *J. Wind Eng. Ind. Aerodyn.* **96** (8-9), 1332–1358. DOI. ↩

[58] Teunissen, H. W. 1970 Characteristics of the Mean Wind and Turbulence in the Planetary Boundary Layer. URL. ↩

[59] Flay, R. G. & Stevenson, D. C. 1988 Integral length scales in strong winds below 20 m. *J. Wind Eng. Ind. Aerodyn.* **28** (1-3), 21–30. DOI. ↩

[60] Counihan, J. 1969 An improved method of simulating an atmospheric boundary layer in a wind tunnel. *Atmos. Environ.* **3** (2), 197–214. DOI. ↩

[61] Sheih, C. M., Tennekes, H., & Lumley, J. L. 1971 Airborne hot-wire measurements of the small-scale structure of atmospheric turbulence. *Phys. Fluids* **14** (2), 201–215. DOI. ↩

[62] Wilson, D. K., Brasseur, J. G., & Gilbert, K. E. 1999 Acoustic scattering and the spectrum of atmospheric turbulence. *J. Acoust. Soc. Am.* **105** (1), 30–34. DOI. ↩

[63] Davenport, A. 1960 Rational for determining design wind velocities. *J. Struct. Div.* **86** (5), 39–68. URL. ↩

[64] Emes, M. J., Arjomandi, M., Kelso, R. M., & Ghanadi, F. 2016 Integral length scales in a low-roughness atmospheric boundary layer. In *Proc. 18th Australas. Wind Eng. Soc. Work.* Number July, pp. 1–4, McLaren Vale, South Australia. URL. ↩

[65] Abiola-Ogedengbe, A., Hangan, H., & Siddiqui, K. 2015 Experimental investigation of wind effects on a standalone photovoltaic (PV) module. *Renew. Energy* **78**, 657–665. DOI. ↩

[66] Mier-Torrecilla, M., Herrera, E., & Doblaré, M. 2014 Numerical Calculation of Wind Loads over Solar Collectors. *Energy Procedia* **49**, 163–173. DOI. ↩

[67] Hess, G. D., Hicks, B. B., & Yamada, T. 1981 The impact of the Wangara experiment. *Boundary-Layer Meteorol.* **20** (2), 135–174. DOI. ↩

[68] Paetzold, J., Cochard, S., Fletcher, D. F., & Vassallo, A. 2016 Wind effects in solar fields with various collector designs. *AIP Conf. Proc.* **1734** (May). DOI. ↩

[69] Cook, N. J. 1997 The Deaves and Harris ABL model applied to heterogeneous terrain. *J. Wind Eng. Ind. Aerodyn.* **66** (3), 197–214. DOI. ↩

[70] Tieleman, H. W. 2008 Strong wind observations in the atmospheric surface layer. *J. Wind Eng. Ind. Aerodyn.* **96** (1), 41–77. DOI. ↩

[71] Gualtieri, G. 2017 Wind resource extrapolating tools for modern multi-MW wind turbines: Comparison of the Deaves and Harris model vs. the power law. *J. Wind Eng. Ind. Aerodyn.* **170** (August), 107–117. DOI. ↩

[72] Sun, H., Gong, B., & Yao, Q. 2014 A review of wind loads on heliostats and trough collectors. *Renew. Sustain. Energy Rev.* **32**, 206–221. DOI. ↩

[73] Cook, N. J. 1973 On simulating the lower third of the urban adiabatic boundary layer in a wind tunnel. *Atmos. Environ.* **7** (7), 691–705. DOI. ↩

[74] Kozmar, H. 2011 Truncated vortex generators for part-depth wind-tunnel simulations of the atmospheric boundary layer flow. *J. Wind Eng. Ind. Aerodyn.* **99** (2-3), 130–136. DOI. ↩

[75] Von Karman, T. 1948 Progress in the statistical theory of turbulence. *Proc. Natl. Acad. Sci.* **34** (11), 530–539. DOI. ↩

[76] Davenport, A. G. 1961 The spectrum of horizontal gustiness near the ground in high winds. *Q. J. R. Meteorol. Soc.* **87** (372), 194–211. DOI. ↩

[77] Holmes, J. D., Allsop, A. C., & Ginger, J. D. 2014 Gust durations, gust factors and gust response factors in wind codes and standards. *Wind Struct.* **19** (3), 339–352. DOI. ↩

[78] Hu, W., Letson, F., Barthelmie, R. J., & Pryor, S. C. 2018 Wind gust characterization at wind turbine relevant heights in moderately complex terrain. *J. Appl. Meteorol. Climatol.* **57** (7), 1459–1476. DOI. ↩

[79] Jarraud, M. 2008 Guide to meteorological instruments and methods of observation (WMO-No. 8). *World Meteorol. Organ. Geneva, Switz.* (8). ISBN. ↩

[80] Solari, G. & Kareem, A. 1998 On the formulation of ASCE7-95 gust effect factor. *J. Wind Eng. Ind. Aerodyn.* **77-78**, 673–684. DOI. ↩

[81] Perrotta, G. & Jones, A. R. 2018 Quasi-steady approximation of forces on flat plate due to large-amplitude plunging maneuvers. *AIAA J.* **56** (11), 4232–4242. DOI. ↩

[82] Davis, F. K. & Newstein, H. 1968 The Variation of Gust Factors with Mean Wind Speed and with Height. *J. Appl. Meteorol.* **7** (3), 372–378. DOI. ↩

[83] Jungo, P., Goyette, S., & Beniston, M. 2002 Daily wind gust speed probabilities over Switzerland according to three types of synoptic circulation. *Int. J. Climatol.* **22** (4), 485–499. DOI. ↩

[84] Cheng, C. S., Li, G., Li, Q., Auld, H., & Fu, C. 2012 Possible impacts of climate change on wind gusts under downscaled future climate conditions over Ontario, Canada. *J. Clim.* **25** (9), 3390–3408. DOI. ↩

[85] Bardal, L. M. & Sætran, L. R. 2016 Wind Gust Factors in a Coastal Wind Climate. *Energy Procedia* **94** (January), 417–424. DOI. ↩

[86] Rakib, M. I., Evans, S. P., & Clausen, P. D. 2020 Measured gust events in the urban environment, a comparison with the IEC standard. *Renew. Energy* **146**, 1134–1142. DOI. ↩

[87] Letson, F., Barthelmie, R. J., Hu, W., & Pryor, S. C. 2019 Characterizing wind gusts in complex terrain. *Atmos. Chem. Phys.* **19** (6), 3797–3819. DOI. ↩

[88] Hufstedler, E. A. L. 2017 *Experimental Generation and Modeling of Vortical Gusts and Their Interactions with an Airfoil*. Doctoral, California Institute of Technology. URL. ↩

[89] Davenport, A. 1964 Note on the Distribution of the Largest Value of a Random Function With Application To Gust Loading. *Proc. Inst. Civ. Eng.* **28** (2), 187–196. DOI. ↩

[90] Thorarinsdottir, T. L. & Johnson, M. S. 2011 Probabilistic Wind Gust Forecasting Using Nonhomogeneous Gaussian Regression. *Mon. Weather Rev.* **140** (3), 889–897. DOI. ↩

[91] Boettcher, F., Renner, C., Waldl, H. P., & Peinke, J. 2003 On the statistics of wind gusts. *Boundary-Layer Meteorol.* **108** (1), 163–173. DOI. ↩

[92] Bergström, H. 1987 A statistical analysis of gust characteristics. *Boundary-Layer Meteorol.* **39** (1-2), 153–173. DOI. ↩

[93] Brasseur, O. 2001 Development and application of a physical approach to estimating wind gusts. *Mon. Weather Rev.* **129** (1), 5–25. DOI. ↩

[94] Bartels, R. 2013 Developing an Accurate CFD Based Gust Model for the Truss Braced Wing Aircraft. In *31st AIAA Appl. Aerodyn. Conf.* Reston, Virginia. American Institute of Aeronautics and Astronautics. DOI. ↩

[95] Heinrich, R. & Reimer, L. 2013 Comparison of different approaches for gust modeling in the CFD code Tau. *IFASD 2013 - Int. Forum Aeroelasticity Struct. Dyn.* URL. ↩

[96] Foerster, M. & Breitsamter, C. 2015 Aeroelastic Prediction of Discrete Gust Loads Using Nonlinear and Time-Linearized. *ASDJournal* **3** (3), 19–38. DOI. ↩

[97] Lancelot, P. M., Sodja, J., Werter, N. P., & Breuker, R. D. 2017 Design and testing of a low subsonic wind tunnel gust generator. *Adv. Aircr. Spacecr. Sci.* **4** (2), 125–144. DOI. ↩

[98] Poorte, R. E. & Biesheuvel, A. 2002 Experiments on the motion of gas bubbles in turbulence generated by an active grid. *J. Fluid Mech.* **461**, 127–154. DOI. ↩

[99] Yang, Y., Li, M., Ma, C., & Li, S. 2017 Experimental investigation on the unsteady lift of an airfoil in a sinusoidal streamwise gust. *Phys. Fluids* **29** (5). DOI. ↩

[100] Hunt, J., Poulton, E., & Mumford, J. 1976 The effects of wind on people; New criteria based on wind tunnel experiments. *Build. Environ.* **11** (1), 15–28. DOI. ↩

[101] Kobayashi, H., Hatanaka, A., & Ueda, T. 1994 Active simulation of time histories of strong wind gust in a wind tunnel. *J. Wind Eng. Ind. Aerodyn.* **53** (3), 315–330. DOI. ↩

[102] Makita, H. & Sassa, K. 1991 Active Turbulence Generation in a Laboratory Wind Tunnel. *Adv. Turbul. 3* 497–505. DOI. ↩

[103] Makita, H. 1991 Realization of a large-scale turbulence field in a small wind tunnel. *Fluid Dyn. Res.* **8** (1-4), 53–64. DOI. ↩

[104] Biler, H., Badrya, C., & Jones, A. R. 2019 Experimental and Computational Investigation of Transverse Gust Encounters. *AIAA J.* **57** (11). DOI. ↩

[105] Van Doom, E., Dhruva, B., Sreenivasan, K. R., & Cassella, V. 2000 Statistics of wind direction and its increments. *Phys. Fluids* **12** (6), 1529–1534. DOI. ↩

[106] Fernandez, F., Cleaver, D., & Gursul, I. 2021 Unsteady aerodynamics of a wing in a novel small-amplitude transverse gust generator. *Exp. Fluids* **62** (1), 1–20. DOI. ↩

[107] Wood, K. T., Cheung, R. M., Richardson, T., Cooper, J., Darbyshire, O., & Warsop, C. 2017 A new gust generator for a low speed wind tunnel: Design and commissioning. *AIAA SciTech Forum - 55th AIAA Aerosp. Sci. Meet.* DOI. ↩

[108] Sang, L. Q., Murata, J., Morimoto, M., Kamada, Y., Maeda, T., & Li, Q. 2017 Experimental investigation of load fluctuation on horizontal axis wind turbine for extreme wind direction change. *J. Fluid Sci. Technol.* **12** (1), 1–12. DOI. ↩

[109] Mackowski, A. W. & Williamson, C. H. 2015 Direct measurement of thrust and efficiency of an airfoil undergoing pure pitching. *J. Fluid Mech.* **765**, 524–543. DOI. ↩

[110] Pfahl, A., Buselmeier, M., & Zaschke, M. 2011 Wind loads on heliostats and photovoltaic trackers of various aspect ratios. *Sol. Energy* **85** (9), 2185–2201. DOI. ↩

[111] Peterka, J. & Derickson, R. 1992 Wind load design methods for ground-based heliostats and parabolic dish collectors. *Tech. rep.* SAND-92-7009, Sandia National Laboratories, Albuquerque, NM. DOI. ↩

[112] Boddupalli, N., Goenka, V., & Chandra, L. 2017 Fluid flow analysis behind heliostat using les and RANS: A step towards optimized field design in desert regions. *AIP Conf. Proc.* **1850** (June). DOI. ↩

[113] Pfahl, A., Buselmeier, M., & Zaschke, M. 2011 Determination of wind loads on heliostats. In *SolarPACES 2011 Conf.* URL. ↩

[114] Marais, M. D., Craig, K. J., & Meyer, J. P. 2015 Computational Flow Optimization of Heliostat Aspect Ratio for Wind Direction and Elevation Angle. *Energy Procedia* **69**, 148–157. DOI. ↩

[115] Wu, Z., Gong, B., Wang, Z., Li, Z., & Zang, C. 2010 An experimental and numerical study of the gap effect on wind load on heliostat. *Renew. Energy* **35** (4), 797–806. DOI. ↩

[116] Pfahl, A. & Uhlemann, H. 2011 Wind loads on heliostats and photovoltaic trackers at various Reynolds numbers. *J. Wind Eng. Ind. Aerodyn.* **99** (9), 964–968. DOI. ↩

[117] Gharakhani Siraki, A. & Pillay, P. 2012 Study of optimum tilt angles for solar panels in different latitudes for urban applications. *Sol. Energy* **86** (6), 1920–1928. DOI. ↩

[118] Ortiz, X., Hemmatti, A., Rival, D., & Wood, D. 2012 Instantaneous Forces and Moments on Inclined Flat Plates. *Seventh Int. Colloq. Bluff Body Aerodyn. Appl. Shanghai, China* 1124–1131. URL. ↩

[119] Hoerner, Sighard, F. 1985 *Fluid Dynamic Lift - Practical Information on Aerodynamic and Hydrodynamic Lift*. 2nd ed. L.A. Hoerner, p. 507. ISBN. ↩

[120] DeVoria, A. C. & Mohseni, K. 2015 Vortex structure of low-aspect-ratio wings in sideslip. In *53rd AIAA Aerosp. Sci. Meet.* Number January, Reston, Virginia. American Institute of Aeronautics and Astronautics. DOI. ↩

[121] Manolesos, M. & Voutsinas, S. G. 2014 Study of a stall cell using stereo particle image velocimetry. *Phys. Fluids* **26** (4). DOI. ↩

[122] Shields, M. & Mohseni, K. 2012 Effects of sideslip on the aerodynamics of low-aspect-ratio low-reynolds-number wings. *AIAA J.* **50** (1), 85–99. DOI. ↩

[123] Schlichting, H. & Gersten, K. 2017 *Boundary-Layer Theory*, vol. 7 of number 2. Springer Berlin Heidelberg, pp. 32–36. DOI. ↩

[124] Mueller, T. J. 2000 Aerodynamic measurements at low Reynolds numbers for fixed wind micro-air vehicles. *Tech. rep.* ADP010760, Defense Technical Information Center, Fort Belvoir, VA. URL. ↩

[125] Liu, Y., Kopp, G. A., & Chen, S. F. 2021 An Examination of the Gust Effect Factor for Rigid High-Rise Buildings. *Front. Built Environ.* **6** (February), 1–14. DOI. ↩

[126] Badrya, C., Baeder, J. D., & Jones, A. R. 2019 Application of prescribed velocity methods to a large-amplitude flat-plate gust encounter. *AIAA J.* **57** (8), 3261–3373. DOI. ↩

[127] Biler, H., Badrya, C., & Jones, A. R. 2018 Experimental and computational investigation of transverse gust encounters. In *2018 AIAA Aerosp. Sci. Meet.* Pp. 1–20, Reston, Virginia. American Institute of Aeronautics and Astronautics. DOI. ↩

[128] Mulleners, K., Mancini, P., & Jones, A. R. 2017 Flow Development on a Flat-Plate Wing Subjected to a Streamwise Acceleration. *AIAA J.* **55** (6), 2118–2122. DOI. ↩

[129] Manar, F. & Jones, A. R. 2019 Evaluation of potential flow models for unsteady separated flow with respect to experimental data. *Phys. Rev. Fluids* **4** (3), 1–35. DOI. ↩

[130] Taira, K. & Colonius, T. 2009 Three-dimensional flows around low-aspect-ratio flat-plate wings at low Reynolds numbers. *J. Fluid Mech.* **623**, 187–207. DOI. ↩

[131] Stevens, P. R., Babinsky, H., Manar, F., Mancini, P., Jones, A. R., Nakata, T., Phillips, N., Bomphrey, R. J., Gozukara, A. C., Granlund, K. O., & Ol, M. V. 2017 Experiments and computations on the lift of accelerating flat plates at incidence. *AIAA J.* **55** (10), 3255–3265. DOI. ↩

[132] Wong, J. G., Mohebbian, A., Kriegseis, J., & Rival, D. E. 2013 Rapid flow separation for transient inflow conditions versus accelerating bodies: An investigation into their equivalency. *J. Fluids Struct.* **40**, 257–268. DOI. ↩

[133] Mancini, P., Manar, F., Granlund, K., Ol, M. V., & Jones, A. R. 2015 Unsteady aerodynamic characteristics of a translating rigid wing at low Reynolds number. *Phys. Fluids* **27** (12). DOI. ↩

[134] Fernando, J. N., Weymouth, G. D., & Rival, D. E. 2020 On the limits of added-mass theory in separated flows and with varying initial conditions. *J. Fluids Struct.* **93**, 102835. DOI. ↩

[135] Gharib, M., Rambod, E., & Shariff, K. 1998 A universal time scale for vortex ring formation. *J. Fluid Mech.* **360**, 121–140. DOI. ↩

[136] Pitt Ford, C. W. & Babinsky, H. 2013 Lift and the leading-edge vortex. *J. Fluid Mech.* **720**, 280–313. DOI. ↩

[137] Ringuette, M. J., Milano, M., & Gharib, M. 2007 Role of the tip vortex in the force generation of low-aspect-ratio normal flat plates. *J. Fluid Mech.* **581**, 453–468. DOI. ↩

[138] Simon, N., Piqué, A., Snyder, D., Ikuma, K., Majumdar, A., & Hultmark, M. 2023 Fast-response hot-wire flow sensors for wind and gust estimation on UAVs. *Meas. Sci. Technol.* **34** (2). DOI. ↩

[139] Kazarina, M. V. & Golubev, V. V. 2019 On 3d effects in gust-airfoil and turbulence-airfoil interaction responses. *AIAA Scitech 2019 Forum* **2** (1), 1–18. DOI. ↩

[140] Ju, H. & Mani, R. 2018 A semi-analytical method for oblique gust - cascade interaction. *J. Sound Vib.* **436**, 95–111. DOI. ↩

[141] Leung, J. M., Wong, J. G., Weymouth, G. D., & Rival, D. E. 2018 Modeling transverse gusts using pitching, plunging, and surging airfoil motions. *AIAA J.* **56** (8), 3271–3278. DOI. ↩

[142] Badrya, C., Biler, H., Jones, A. R., & Baeder, J. D. 2021 Effect of gust width on flat-plate response in large transverse gust. *AIAA J.* **59** (1), 49–64. DOI. ↩

[143] Storey, R. C., Norris, S. E., & Cater, J. E. 2014 Modelling turbine loads during an extreme coherent gust using large eddy simulation. *J. Phys. Conf. Ser.* **524** (1). DOI. ↩

[144] Menegozzo, L., Dal Monte, A., Benini, E., & Benato, A. 2018 Small wind turbines: A numerical study for aerodynamic performance assessment under gust conditions. *Renew. Energy* **121**, 123–132. DOI. ↩

[145] Sang, L. Q., Maeda, T., & Kamada, Y. 2019 Study effect of extreme wind direction change on 3-bladed horizontal axis wind turbine. *Int. J. Renew. Energy Dev.* **8** (3), 261–266. DOI. ↩

[146] Ma, G., Zhong, L., Zhang, X., Ma, Q., & Kang, H. S. 2020 Mechanism of mooring line breakage of floating offshore wind turbine under extreme coherent gust with direction change condition. *J. Mar. Sci. Technol.* **25** (4), 1283–1295. DOI. ↩

[147] Tudball Smith, D., Rockwell, D., Sheridan, J., & Thompson, M. 2017 Effect of radius of gyration on a wing rotating at low Reynolds number: A computational study. *Phys. Rev. Fluids* **2** (6), 1–23. DOI. ↩

[148] Garmann, D. J. & Visbal, M. R. 2014 Dynamics of revolving wings for various aspect ratios. *J. Fluid Mech.* **748** (3), 932–956. DOI. ↩

[149] Rozhdestvensky, K. V. 2006 Wing-in-ground effect vehicles. *Prog. Aerosp. Sci.* **42** (3), 211–283. DOI. ↩

[150] Zhang, X., Toet, W., & Zerihan, J. 2006 Ground effect aerodynamics of race cars. *Appl. Mech. Rev.* **59** (1-6), 33–48. DOI. ↩

[151] Rayner, J. M. V. & Rayner, J. M. V. 1991 On the aerodynamics of animal flight in ground effect. *Philos. Trans. R. Soc. London. Ser. B Biol. Sci.* **334** (1269), 119–128. DOI. ↩

[152] Qu, Q., Wang, W., Liu, P., & Agarwal, R. K. 2015 Airfoil aerodynamics in ground effect for wide range of angles of attack. *AIAA J.* **53** (4), 1048–1061. DOI. ↩

[153] Wang, Y., Thompson, D., & Hu, Z. 2019 Effect of wall proximity on the flow over a cube and the implications for the noise emitted. *Phys. Fluids* **31** (7). DOI. ↩

[154] Ahmed, M. R. 2005 Aerodynamics of a cambered airfoil in ground effect. *Int. J. Fluid Mech. Res.* **32** (2), 157–183. DOI. ↩

[155] Martinuzzi, R. J., Bailey, S. C., & Kopp, G. A. 2003 Influence of wall proximity on vortex shedding from a square cylinder. *Exp. Fluids* **34** (5), 585–596. DOI. ↩

[156] Lei, C., Cheng, L., & Kavanagh, K. 1999 Re-examination of the effect of a plane boundary on force and vortex shedding of a circular cylinder. *J. Wind Eng. Ind. Aerodyn.* **80** (3), 263–286. DOI. ↩

[157] Liu, I. H. & Oztekin, A. 2018 Three-dimensional transient flows past plates translating near a wall. *Ocean Eng.* **159** (May), 9–21. DOI. ↩

[158] Bleischwitz, R., de Kat, R., & Ganapathisubramani, B. 2017 On the fluid-structure interaction of flexible membrane wings for MAVs in and out of ground-effect. *J. Fluids Struct.* **70** (June 2016), 214–234. DOI. ↩

[159] Bleischwitz, R., de Kat, R., & Ganapathisubramani, B. 2018 Near-wake characteristics of rigid and membrane wings in ground effect. *J. Fluids Struct.* **80**, 199–216. DOI. ↩

[160] Lu, A. & Lee, T. 2021 Effect of ground boundary condition on near-field wingtip vortex flow and lift-induced drag. *J. Fluids Eng. Trans. ASME* **143** (3). DOI. ↩

[161] Boschetti, P. J., Quijada, G., & Cárdenas, E. M. 2016 Dynamic Ground Effect on the Aerodynamic Coefficients of a Wing using a Panel Method. In *AIAA Atmos. Flight Mech. Conf.* Reston, Virginia. American Institute of Aeronautics and Astronautics. DOI. ↩

[162] Qu, Q., Jia, X., Wang, W., Liu, P., & Agarwal, R. K. 2014 Numerical simulation of the flowfield of an airfoil in dynamic ground effect. *J. Aircr.* **51** (5), 1659–1662. DOI. ↩

[163] Kurelek, J. W. 2016 *Transition in a Laminar Separation Bubble and the Effect of Acoustic Excitation*. Master, University of Waterloo. URL. ↩

[164] Toppings, C. E. 2021 *Laminar separation bubble development on a finite wing*. Master, University of Waterloo. URL. ↩

[165] Kurelek, J. W. 2021 *The Vortex Dynamics of Laminar Separation Bubbles*. PhD, University of Waterloo. URL. ↩

[166] Pelletier, A. & Mueller, T. J. 2000 Low Reynolds Number Aerodynamics of Low-Aspect-Ratio, Thin/Flat/Cambered-Plate Wings. *J. Aircr.* **37** (5), 825–832. DOI. ↩

[167] Hanson, R. E., Buckley, H. P., & Lavoie, P. 2012 Aerodynamic optimization of the flat-plate leading edge for experimental studies of laminar and transitional boundary layers. *Exp. Fluids* **53** (4), 863–871. DOI. ↩

[168] Cowdrey, C. 1968 Two Topics of Interest in Experimental Industrial Aerodynamics—Part 1: Application of Maskell's Theory of Wind-Tunnel Blockage to Some Large Models, Part 2: Design of Velocity-Profile Grids. *Tech. rep.* Aero Report No. 1268. ↩

[169] Maskell, E. C. 1965 A Theory of Blockage Effects on Bulff Bodies and Stalled Wings in a Closed Wind Tunnel. *Tech. rep.* ARC/R&M-3400. URL. ↩

[170] Yuan, Q. & Yarusevych, S. 2020 Wake topology and dynamics over a slender body at a high incidence and their relation to structural loading. *Phys. Fluids* **32** (5), 055111. DOI. ↩

[171] Wang, Y., Curran, J., Padfield, G. D., & Owen, I. 2011 AirDyn: An instrumented model-scale helicopter for measuring unsteady aerodynamic loading in airwakes. *Meas. Sci. Technol.* **22** (4). DOI. ↩

[172] Merzkirch, W. 2007 Flow Visualization. In *Springer Handb. Exp. Fluid Mech.* Pp. 857–870. Springer Berlin Heidelberg. DOI. ↩

[173] Smits, A. J. 2012 *Flow Visualization: Techniques and Examples*. Imperial College Press. ISBN. ↩

[174] Toppings, C. E. & Yarusevych, S. 2022 Structure and dynamics of a laminar separation bubble near a wing root: towards reconstructing the complete LSB topology on a finite wing. *J. Fluid Mech.* **944**. DOI. ↩

[175] Perry, A. E. & Fairlie, B. D. 1975 Critical points in flow patterns. *Adv. Geophys.* **18** (PB), 299–315. DOI. ↩

[176] Tobak, M. & Peake, D. J. 1982 Topology of Three-Dimensional Separated Flows. *Annu. Rev. Fluid Mech.* **14** (1), 61–85. DOI. ↩

[177] Délery, J. M. 2001 Robert Legendre and Henri Werlé: Toward the elucidation of three-dimensional separation. *Annu. Rev. Fluid Mech.* **33** (1), 129–154. DOI. ↩

[178] Westerweel, J., Elsinga, G. E., & Adrian, R. J. 2013 Particle image velocimetry for complex and turbulent flows. *Annu. Rev. Fluid Mech.* **45** (1), 409–436. DOI. ↩

[179] Raffel, M., Willert, C. E., Scarano, F., Kähler, C. J., Wereley, S. T., & Kompenhans, J. 2018 *Particle Image Velocimetry*. Springer International Publishing. DOI. ↩

[180] Melling, A. 1997 Tracer particles and seeding for particle image velocimetry. *Meas. Sci. Technol.* **8** (12), 1406–1416. DOI. ↩

[181] Bhattacharya, S., Charonko, J. J., & Vlachos, P. P. 2017 Stereo-particle image velocimetry uncertainty quantification. *Meas. Sci. Technol.* **28** (1). DOI. ↩

[182] Wieneke, B. 2005 Stereo-PIV using self-calibration on particle images. *Exp. Fluids* **39** (2), 267–280. DOI. ↩

[183] Sciacchitano, A. & Scarano, F. 2014 Elimination of PIV light reflections via a temporal high pass filter. *Meas. Sci. Technol.* **25** (8). DOI. ↩

[184] Scarano, F. & Riethmuller, M. L. 2000 Advances in iterative multigrid PIV image processing. *Exp. Fluids* **29** (SUPPL. 1). DOI. ↩

[185] Westerweel, J. & Scarano, F. 2005 Universal outlier detection for PIV data. *Exp. Fluids* **39** (6), 1096–1100. DOI. ↩

[186] Wieneke, B. 2015 PIV uncertainty quantification from correlation statistics. *Meas. Sci. Technol.* **26** (7). DOI. ↩

[187] Sciacchitano, A., Neal, D. R., Smith, B. L., Warner, S. O., Vlachos, P. P., Wieneke, B., & Scarano, F. 2015 Collaborative framework for PIV uncertainty quantification: Comparative assessment of methods. *Meas. Sci. Technol.* **26** (7). DOI. ↩

[188] Epps, B. P. 2017 Review of vortex identification methods. *AIAA SciTech Forum - 55th AIAA Aerosp. Sci. Meet.* (January). DOI. ↩

[189] Jeong, J. & Hussain, F. 1995 On the identification of a vortex. *J. Fluid Mech.* **285**, 69. DOI. ↩

[190] Eldredge, J. D. & Jones, A. R. 2019 Leading-Edge Vortices: Mechanics and Modeling. *Annu. Rev. Fluid Mech.* **51** (1), 75–104. DOI. ↩

[191] Jiang, M., Machiraju, R., & Thompson, D. 2005 Detection and Visualization of Vortices. In *Vis. Handb.* Pp. 295–309. Elsevier. DOI. ↩

[192] Graftieaux, L., Michard, M., & Nathalie, G. 2001 Combining PIV, POD and vortex identification algorithms for the study of unsteady turbulent swirling flows. *Meas. Sci. Technol.* **12** (9), 1422–1429. DOI. ↩

[193] Moffat, R. J. 1982 Contributions to the Theroy of Single-Sample Uncertainity Analysis. *J. Fluids Eng.* **104** (June), 250–258. DOI. ↩

[194] Moffat, R. J. 1988 Describing the uncertainties in experimental results. *Exp. Therm. Fluid Sci.* **1** (1), 3–17. DOI. ↩

[195] Li, Z., Lan, C., Jia, L., & Ma, Y. 2017 Ground effects on separated laminar flows past an inclined flat plate. *Theor. Comput. Fluid Dyn.* **31** (2), 127–136. DOI. ↩

[196] Reina, G. P. & De Stefano, G. 2017 Computational evaluation of wind loads on sun-tracking ground-mounted photovoltaic panel arrays. *J. Wind Eng. Ind. Aerodyn.* **170** (August), 283–293. DOI. ↩

[197] Cooper, K. 1998 Bluff-body Blockage Corrections in Closed- and Open-Test-Section Wind Tunnels. *Tech. rep.* AGARD-AG-336, National Technical Information Service, Springfield, VA. URL. ↩

[198] Seif, M. S. & Dakhrabadi, M. T. 2016 A practical method for aerodynamic investigation of WIG. *Aircr. Eng. Aerosp. Technol.* **88** (1), 73–81. DOI. ↩

[199] Wieselsberger, C. 1922 Wing resistance near the ground. *Tech. rep.*, National Advisory Committee for Aeronautics Collection. URL. ↩

[200] Van Oudheusden, B. W. 2013 PIV-based pressure measurement. *Meas. Sci. Technol.* **24** (3). DOI. ↩

[201] Zhang, P., Peterson, S. D., & Porfiri, M. 2019 Combined particle image velocimetry/digital image correlation for load estimation. *Exp. Therm. Fluid Sci.* **100** (August 2018), 207–221. DOI. ↩

[202] Van der Kindere, J. W., Laskari, A., Ganapathisubramani, B., & de Kat, R. 2019 Pressure from 2D snapshot PIV. *Exp. Fluids* **60** (2), 1–18. DOI. ↩

[203] McClure, J. & Yarusevych, S. 2017 Optimization of planar PIV-based pressure estimates in laminar and turbulent wakes. *Exp. Fluids* **58** (5), 1–18. DOI. ↩

[204] Jardin, T., Farcy, A., & David, L. 2012 Three-dimensional effects in hovering flapping flight. *J. Fluid Mech.* **702**, 102–125. DOI. ↩

[205] Mammar, M., Djouimaa, S., Gärtner, U., & Hamidat, A. 2018 Wind loads on heliostats of various column heights: An experimental study. *Energy* **143**, 867–880. DOI. ↩

[206] Hartlin, S. 2022 *Sideslip effects on a square flat plate under freestream turbulence*. Master, McGill University. ↩

[207] DeVoria, A. C. & Mohseni, K. 2017 A vortex model for forces and moments on low-aspect-ratio wings in side-slip with experimental validation. *Proc. R. Soc. A Math. Phys. Eng. Sci.* **473** (2198). DOI. ↩

[208] Tumse, S., Karasu, I., & Sahin, B. 2022 Experimental Investigation of Ground Effect on the Vortical Flow Structure of a 40° Swept Delta Wing. *J. Aerosp. Eng.* **35** (4), 04022055. DOI. ↩

[209] Oguz Tasci, M., Tumse, S., & Sahin, B. 2022 Vortical flow characteristics of a slender delta wing in ground effect. *Ocean Eng.* **261** (March), 112120. DOI. ↩

[210] Yen, S. C. & Fei, Y. F. 2011 Winglet dihedral effect on flow behavior and aerodynamic performance of NACA0012 wings. *J. Fluids Eng. Trans. ASME* **133** (7). DOI. ↩

[211] Smith, S. E., Viggiano, B., Ali, N., Silverman, T. J., Obligado, M., Calaf, M., & Cal, R. B. 2022 Increased panel height enhances cooling for photovoltaic solar farms. *Appl. Energy* **325** (July), 119819. DOI. ↩

[212] Moshfegh, B. & Sandberg, M. 1998 Flow and heat transfer in the air gap behind photovoltaic panels. *Renew. Sustain. Energy Rev.* **2** (3), 287–301. DOI. ↩

[213] Kaplani, E. & Kaplanis, S. 2014 Thermal modelling and experimental assessment of the dependence of PV module temperature on wind velocity and direction, module orientation and inclination. *Sol. Energy* **107**, 443–460. DOI. ↩

[214] Jubayer, C. M., Siddiqui, K., & Hangan, H. 2016 CFD analysis of convective heat transfer from ground mounted solar panels. *Sol. Energy* **133**, 556–566. DOI. ↩

[215] Strobel, K. & Banks, D. 2014 Effects of vortex shedding in arrays of long inclined flat plates and ramifications for ground-mounted photovoltaic arrays. *J. Wind Eng. Ind. Aerodyn.* **133**, 146–149. DOI. ↩

[216] Martínez-García, E., Blanco-Marigorta, E., Parrondo Gayo, J., & Navarro-Manso, A. 2021 Influence of inertia and aspect ratio on the torsional galloping of single-axis solar trackers. *Eng. Struct.* **243**, 112682. DOI. ↩

[217] Linehan, T. & Mohseni, K. 2019 Investigation of a sliding alula for control augmentation of lifting surfaces at high angles of attack. *Aerosp. Sci. Technol.* **87**, 73–88. DOI. ↩

[218] Linehan, T. & Mohseni, K. 2020 On the maintenance of an attached leading-edge vortex via model bird alula. *J. Fluid Mech.* **897**. DOI. ↩